THE DYNAMICS OF GRANULAR SOLIDS

A Thesis Submitted for the Degree

Doctor of Philosophy

by

L. W. Saperstein

The Queen's College, Oxford

Department of Engineering Science

Oxford University

Trinity 1967

ABSTRACT

A theoretical and experimental examination into the dynamics of granular solids has been completed which covers aspects of flow and failure within this material. The investigation is divided into three natural sections; each section being devoted to a different type of failure. As indicated by the title, the subject of the study was cohesionless soil, and thus the basic tenets of soil mechanics and the failure of granular media are applicable.

The first section deals with gravity flow of non-cohesive granular material in both axial and rectangular geometry. Traditional plasticity theory is used to establish characteristics of stress and strain, also stress sliplines within a wedge. From these, two relationships between the angle of internal friction and the bound to a radial flow field are established. A minimum energry theory of flow is discussed and then used to determine mass flow rates. From this theory a velocity profile is deduced and by use of either the entire profile or the vertical ray or the extreme angular ray three relationships between the bound to the radial flow field and the mass flow rate are established.

The limits to piping in axial symmetry are defined. It is shown that gravity flow in rectangular geometry must always result in pipes.

Experiments were devised to substantiate these findings and they show that, dependent upon the assumptions that were made, the devised relationships bracket, within reasonable limits, the radial bound and the mass flow rate. Work of two other investigators is compared with the presented experimental results. The definitions of piping are shown to have validity.

Section Two was the result of an attempt to measure a parameter that

was relevant to the investigation in Section Three. The possibility of the passive rather than the active lateral earth pressure acting upon a shifting retaining wall was discovered while attempting the measurement of the coefficient of friction of sand on mild steel.

The third section is concerned with an investigation into the factors that affect the forces on a horizontally propelled model that is immersed in sand. The parameters of depth, speed, projected model area, and other model characteristics were varied, and experimental relationships between the force and these parameters determined. Also, pressure measurements were made within the sand as the model passed to determine the extent of the failure region. Several other experiments, such as the effect of false walls on the force level, were made in order to determine the limits of validity of the main experiment.

It was found that the force on the model varied as the 2.3 power of the depth, linearly with the projected model area, and not at all with model surface, model length, or speed in the range 0 - 15 feet per minute. The pressure measurements and false-walls studies showed that failure occurred within the sand and not at the walls of the tank; also that failure took the form of successive shear dislocation of pyramidally shaped wedges of sand.

TABLE OF CONTENTS

Abstract 1

Table of Contents iii

List of Illustrations v

List of Nomenclature viii

Section I: Flow Studies

Introduction 1

Subject 1

Past Empirical Work 1

Plasticity Theory 4

Traditional Plasticity Theory as Applied to the Failure of Granular Media 5

The Yield Function 5

The Equations of Stress 11

The Equations of Strain 14

Transformation of Axes 17

The Theory of a Wedge 18

Recent Work on Converging Flow 22

The Slipline Field 22

Flow-Rate Theory 25

Applications to Radial Theory 32

The Radial Bound 32

Flow Rates 36

Piping 38

Experiment or Verification of Theoretical Relationships 43

Establishment of Physical Parameters 43

TABLE OF CONTENTS CONTINUED

Flow Rate as a Function of Orifice Diameter 45

θ' Variation 49

Plane Flow 51

Non-Influential Parameters 57

Radial Bound 58

Errors 63

Correlation of Experiment to Theory 67

Flow Fields 67

Flow Rates 67

Section II

A Relationship Between Frictive Forces and Earth Pressure Coefficients 74

Section III: Tow - Tank Studies

Introduction 79

General 79

Previous Work 80

Aims 82

Equipment and Procedure 83

Mechanical Equipment 83

Electrical Equipment 96

Procedure 97

Results 103

General 103

Depth 103

Model Variation 104

TABLE OF CONTENTS CONTINUED

Speed Changes 111

Pressure and Boundary Effects 115

Trolley Draft 144

Errors and Analysis of Results 145

Errors 145

Analysis 148

Bibliography 154

LIST OF ILLUSTRATIONS

1	Coulomb's Failure Surface	6
2	Three-Dimensional Failure Surface	6
3	Cartesian Co-ordinates	12
4	Cylindrical Polar Co-ordinates	12
5	Spherical Polar Co-ordinates	12
6	Slipline in a Radial Wedge	21
7	Flow-Field Geometry	27
8	The Angle of the Principal Stress with a Ray Minus 90° versus the Angle of the Ray	34
9	Dimensions in a Pipe	39
10	Unbounded Flow Field	39
11	Bounded Flow Fields	39
12	The Nozzles	47
13	Orifice Diameter versus Flow Rate	48
14	Particle Diameter versus Flow Rate	50
15	Flow Rate versus Cone Angle, θ'	52
16	Flow Rate versus Wall Angle, θ', for Rectangular Geometry, ¼-inch Slit	54
17	Flow Rate versus Wall Angle, θ', 3/16-inch Slit	55
18	Piping in Rectangular Geometry	56
19	The Perspex Tube	59
20	Dimensions of the Perspex Tube	59
21	Wax-Cast Models of Ballotini No. 4	62
22	Wax-Cast Model of Silicon Carbide Showing Piping	64
23	Natural Radial Bound, θ', versus the Angle of Internal	

LIST OF ILLUSTRATIONS CONTINUED

	Friction, ϕ	68
24	Flow Rate versus Angle of Internal Friction, ϕ, with the Flow-Rate Equations based on Equation (69) for the Radial Bound	70
25	Flow Rate versus Angle of Internal Friction using Equation (71) for the Radial Bound	71
26	Flow Rate versus Cone Angle, θ', with Imposed Theoretical Curves	72
27	Relative Frictive Force versus Area; Variable Dimension Horizontal	77
28	Relative Frictive Force versus Area; Variable Dimension Vertical	78
29	Tow-Tank Cross-Section	84
30	The Tank and Related Equipment	85
31	The Trolley	89
32	The Trolley in Place	90
33	The Probe and its Support	90
34	The Probe	92
35	Section View of the Lower Beam and Model, Showing the Strain-Gauge Mount	93
36	The Model Profiles	95
37	Strain Bridge Circuit Diagram	98
38	The Soil Pressure Gauge	99
39	Force versus Depth	105
40	Force versus Cylinder Area	108

LIST OF ILLUSTRATIONS CONTINUED

41	Force with Variation of Cone Angle	108
42	Force versus Projected Area	110
43	Recorder Chart Showing Strain Output for Run when Model was Held in the Sand	113
44	Force versus Speed	114
45	Static Pressures versus Depth	122
46	Contour Plot of Equal Pressures: 11-inch Rod	123
47	Contour Plot of Equal Pressures: Model One at 18 inches	124
48	Contour Plot of Equal Pressures: Model One at 24 inches	125
49	X - Y Plot Showing Soil Pressure Gauge Output	127
50	Half-Buried False Walls	130
51	Recorder Chart Showing Strain Output when Model was Run between False Walls	131
52	Smooth Sand Surface	133
53	Sand Surface After Model One at 18 inches Passed	133
54	Sand Surface After Model One at 18 inches Passed	134
55	Sand Surface After Model One at 21 inches Passed	134
56	Sand Surface After Model One at 24 inches Passed	135
57	Sand Surface After Model One Passed between the False Walls	135
58	The Failed Wedge	138
59	X - Y Plot of Axial Pressures below the Model	139
60	X - Y Plot of Axial Pressures above the Model	139
61	Position of Line of Failure in the Axial Direction	140
62	X-Y Plot of Normal Pressure as Model Passes Completely	141
63	Chart Showing Strain Output of Successive Shear Failure	143
64	Possible Dead-Zone of Moving Material in Front of the Model	151

LIST OF NOMENCLATURE

Symbol	Meaning	Page Where First Found
A	Area	26
a	Subscript indicating Active	7
C	a Constant	
c	Cohesion	5
D	Orifice Diameter	26
D'	Effective Orifice Diameter	26
d	Particle Diameter	26
d	Depth	74
E	Modulus of Elasticity	94
e	Natural Logarithms' Base	24
e	Voids Ratio	147
F	Frictive Force	74
F	Force	109
f	Function of	
f_c	Unconfined Yield Pressure	38
g	Acceleration due to Gravity	28
g	a Function	28
h	depth	104
h	Subscript indicating Hydrostatic	121
i	Subscript indicating a co-ordinate direction	
$J_{1,2,3}$	Invariants	8
$J'_{1,2,3}$	Invariants on a Deviatoric Plane	8
j	Subscript indicating a co-ordinate direction	
K	Coefficient of lateral earth pressures	7

Symbol	Meaning	Page Where First Found
k	a Constant of Proportionality	
k	equivalent to K	10
l	Slit Length	28
l'	Effective Slit Length	28
m	Coefficient of symmetry	18
m	Weight per granule	26
N	Number of granules per unit area per unit time	26
N	Normalizing factor	37
n	a Number	19
n	a Coefficient	26
n	a Ratio	38
o	Subscript indicating that a function of θ is at $\theta = 0$	23
P	Perimeter	74
P	Pressure	104
Q	Mass Flow Rate	26
q	Function for dimensionless Flow Rate	28
q	a Ratio	41
R	a Ray	26
R	Electrical Resistance	101
r	a Ray, a Radial direction, a Radius Vector	17
S	Slit Width	28
S'	Effective Slit Width	28
s	a Function involved in Stress	18
s	Standard Deviation	103
T	Total Energy	23

Symbol	Meaning	Page where First Found
u	Component of Strain	15
V	Velocity	47
V	Volume	137
v	Component of Strain	15
v	Velocity	28
$v_{r,\theta}$	Velocity Components	37
$\dot{W}$	Mass Flow Rate	2
x	a Variable	74
x, y, z	Cartesian Co-ordinates	11
Y	Constant of Yield Functions	8
α	Horizontal Angular Direction	17
α	Trigonometric Substitution	15
β	Trigonometric Substitution	16
γ	Bulk Density	13
Δ	Bin Diameter	2
Δ	Increment	
δ	Angle between a Slipline and the Principal Stress	14
δ	Effective Angle of Friction	23
ϵ	a Strain	21
ϵ	a Function	25
$\epsilon_{i,j}$	a Strain in the i-plane acting in the j-direction	21
θ	Polar Angle	17
θ	Angle of a Ray with the Vertical	22
θ	Model Cone Angle	107
θ'	Angle of a Wall with the Vertical	26

Symbol	Meaning	Page where First Found
λ	Ratio of Flow-Field Width to Total Width	24
μ	Coefficient of Friction	75
ξ	a Function	24
π	a Constant = 3.1416	
ρ	Particle Density	44
σ	Normal Stress	5
$\sigma_{i,j}$	Normal Stress in the i-plane acting in the j-direction	11
τ	Shear Stress	5
$\tau_{i,j}$	Shear Stress in the i-plane acting in the j-direction	11
ϕ	Angle of Internal Friction	5
ϕ'	Angle of Internal Friction for Real Space	10
ϕ'	Angle of Wall Friction	23
ψ	Semi-vertical Angle made by Principal Stress and Ray	17
ω	Semi-vertical Angle made by Principal Stress and x-axis	11
1, 2, 3	Numbering for Principal Stresses or Strains	5
∂	Differential	
$\propto$	Symbol of Proportionality	
$\sim$	Symbol for Approximate	

THE DYNAMICS OF GRANULAR SOLIDS

Section I: Flow Studies

INTRODUCTION

Subject

This section is concerned with the flow of granular media, often called bulk solids, through a nozzle. Simply put, this is a subject of importance to any field, or industry, where efficiency of transfer of this material is a concern. Gravity flow of granular material through a nozzle is a simulation of flow of this material from a hopper or container, or even through any constriction.

The interest in this field came indirectly. Originally the studies were planned as background material for the tow-tank studies described in Section III. After some investigation, it became obvious that the two studies were separate and discrete. Although the basic tenets of soil mechanics are common to both; the methods and means are disparate. Therefore the two studies are treated separately.

After discarding the notion that the flow studies were a prelude to the tank studies, the more far-reaching aims of these studies became apparent. Thus the ultimate ambition was to co-ordinate theoretical considerations of flow to practical ones; that is to find a flow-field and verify it experimentally, and to determine flow-rates and verify them. The case of plane symmetry is examined as well as the case of axial symmetry, however, the axial case is more closely examined because it more nearly approximates reality. It will be shown that the flow in the axial case is more efficient than in the plane.

Past Empirical Work

At this point, some background material will be useful. Various exper-

imenters have established equations of flow by examination of the experimental parameters to create dimensionless units and then by using their data to form proportionality factors which equate their flow rates to these dimensionless units. Although their results are entirely dependent on their form of experimentation, many relevant relationships have been uncovered. Therefore synopses of this work will be presented here and then the information held in abeyance until it applies to the work being reported herein.

Considered first is the work of Rose and Tanaka who separated the parameters as described above and then experimentally determined the variation of flow-rate with change in these groups. Using their symbolism, the grouping was as follows: flow-rate, $W/(D^{2.5}\rho\, g^{\frac{1}{2}})$; aperture diameter to particle diameter, D/d; bin diameter to aperture diameter, Δ/D; head height to bin diameter, H/Δ; cohesion related to aperture diameter, density, and gravity acceleration, $C/(D^{3}\rho\, g)$; the coefficient of friction, μ; a shape factor, Z; and the vertical cone angle, θ. Examining each group experimentally, they concluded that as long as Δ/D and H/D were greater than 2.5 (as is usually the case) their variation had no effect on the flow rate; that surprisingly μ variations had no effect on flow rate, but C variations did; that a shape factor of particles was relevant; that the cone angle was also relevant; that for D/d reasonably large, flow varied as $(D/d)^{0.3}$ and for D/d small, but not cohesive, flow varied as $(D/d - 3)^{0.3}$ indicating that the minimum aperture for flow to continue was three times the particle diameter. From the above, and making a few simplifying assumptions, they concluded that

$$W/(D^{2.5}\rho\, g^{\frac{1}{2}}) = 0.16(D/d)^{0.3} \text{ times } \phi(\theta) \text{ times } (Z - 5)^{-\frac{1}{2}},$$

where ϕ indicates "function of".

Next is the work of Franklin and Johanson who started with an equation attributed to Deming and Mehring

$$t = (\mu_1/D_o^{2.5}D_p)[0.201 + (39.2 + 2.58\sin\tfrac{1}{2}\phi)((D_p/D_o) + 0.130 - 0.161\mu_1)],$$

where t is time of flow, μ_1 is the tangent of the static angle of repose, D_o is the orifice diameter, D_p is the prrticle diameter, and ϕ is the cone angle; and adapted it for use with a flat plate. Their equation, devised for a flat plate, was

$$W = \rho_p D_o^{2.93}/[(6.288\mu + 23.16)(D_p + 1.889) - 44.90],$$

where W is flow in pounds per minute, ρ_p is the density (pounds per cubic foot) of the particles, μ is the tangent of the internal kinetic angle of repose, and D is as before.

Fowler and Glastonbury suggest the following equation:

$$W/\rho_B A(2gD_h)^{\frac{1}{2}} = 0.236(D_h/d_s)^{0.185},$$

where W is weight per unit time, ρ_B is the bulk density of packing, A is the free-flow area of orifice, g is the gravitational constant, D_h is the hydraulic or perimetral diameter (D_h = 4A/perimeter of orifice), and d_s is particle diameter. Their equation is for use only with a flat plate, but is adapted for different shaped orifices.

The last equation, from an early work of Brown and Richards, which was also developed only for flat plates and for material of specific gravity 2.5, is

$$Q = 2.24\ D^{2.5}\ \psi$$

for circular orifices; and

$$Q = 2.72\ A(H)^{\frac{1}{2}}\ \psi$$

for rectilinear apertures. The aperture dimensions are to be in inches, Q is tons per hour, A is area of the aperture; H is the perimetral diameter as above; D is the orifice diameter; and ψ is a dimensionless group, $v/(gH)^{\frac{1}{2}}$,

where v is the mean linear velocity, $Q/\rho A$, and ρ is the particle density.

Plasticity Theory

In order to obtain a true picture of a flow field that is solidly based on theory, an approach must be adopted that is not based on empiricism. Hence plasticity theory as applied to the failure of granular media is used as a starting point for development. Empirical data is to be used to determine the correctness of the theory, but not to establish the theory itself. In addition to giving a purely theoretical approach, this treatment has the advantage of being able to predict an accurate failure surface in two dimensions. Unfortunately, to date, the extension of plasticity theory to three dimensions creates so many unknowns as to be unsolvable. Therefore, the most work has been done in soving the plane case and some of that is reviewed. The theory developed here is an extension of plane theory to the case of axial symmetry.

To obtain a flow-rate theory, the bounds of the flow field are applied to a minimum energy theory of flow. The minimum energy theory is also reviewed.

TRADITIONAL PLASTICITY THEORY AS APPLIED TO THE FAILURE OF GRANULAR MEDIA

The Yield Function

General: In the following discussion, it is assumed that the material dealt with is rigid-plastic, isotropic, and has friction. The particular case being investigated is of soils without cohesion; therefore, to simplify matters, cohesive strength, although alluded to, does not enter into the derivation of the theory. Much of the basic theory is taken from Scott or Sokolovskii; references to metal plasticity are from Hill or Johnson and Mellor. In addition, all statements drawn from reference sources are credited to their source.

Two Dimensions: In a general soil, the criterion for stability, and thus failure, was given by Coulomb in 1773 as

$$|\tau| \leq \sigma \tan\phi + c. \qquad (1)$$

That is the shearing stress on a section of isotropic, cohesive soil must be less than the cohesion plus the normal stress on that same section times the coefficient of internal friction. Failure occurs when the shear stress equals the cohesion plus this value of the normal stress. The geometry of this situation is shown in Figure 1.

Mohr adapted this yield condition and represented it by means of a graphical plot of principal stresses upon stress co-ordinates, where the normal stress, σ, is the abscissa and the shear stress, τ, is the ordinate. In Figure 1, σ_1, the major, and σ_3, the minor, are the principal stresses, c is the cohesion, c cotϕ is the tensile strength, and ϕ is the angle, called the angle of internal friction, made by the envelope surrounding the circles of radius $(\sigma_1 - \sigma_3)/2$ and the abscissa. It will be accepted that, although Figure 1 demonstrates cohesion, cohesionless material is being dealt with

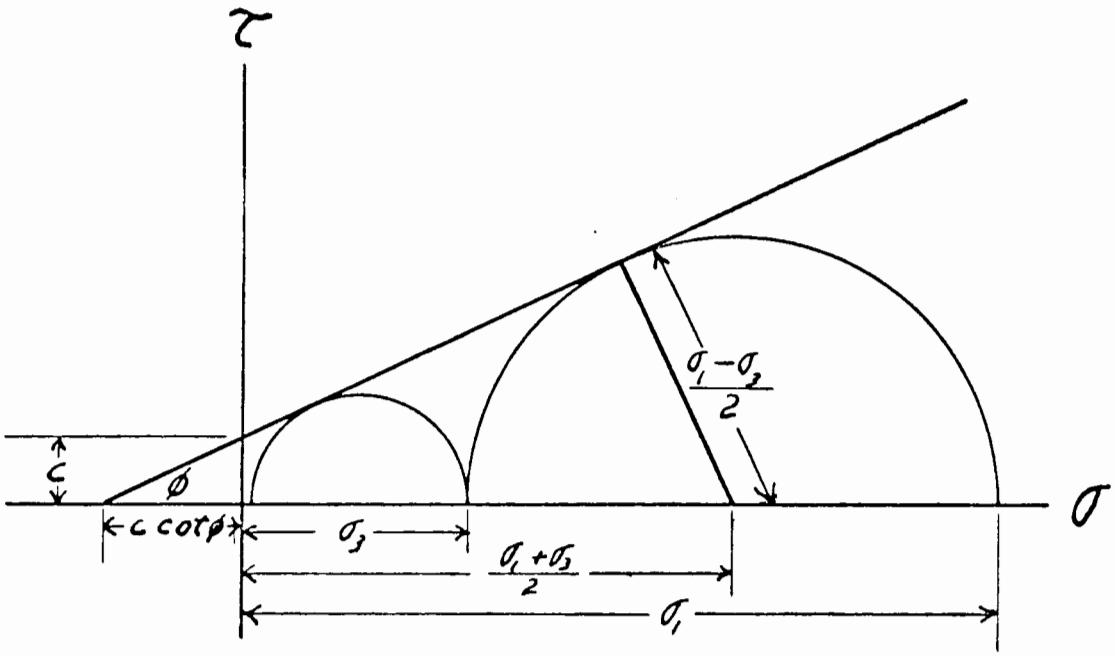

Figure 1: Coulomb's Failure Surface

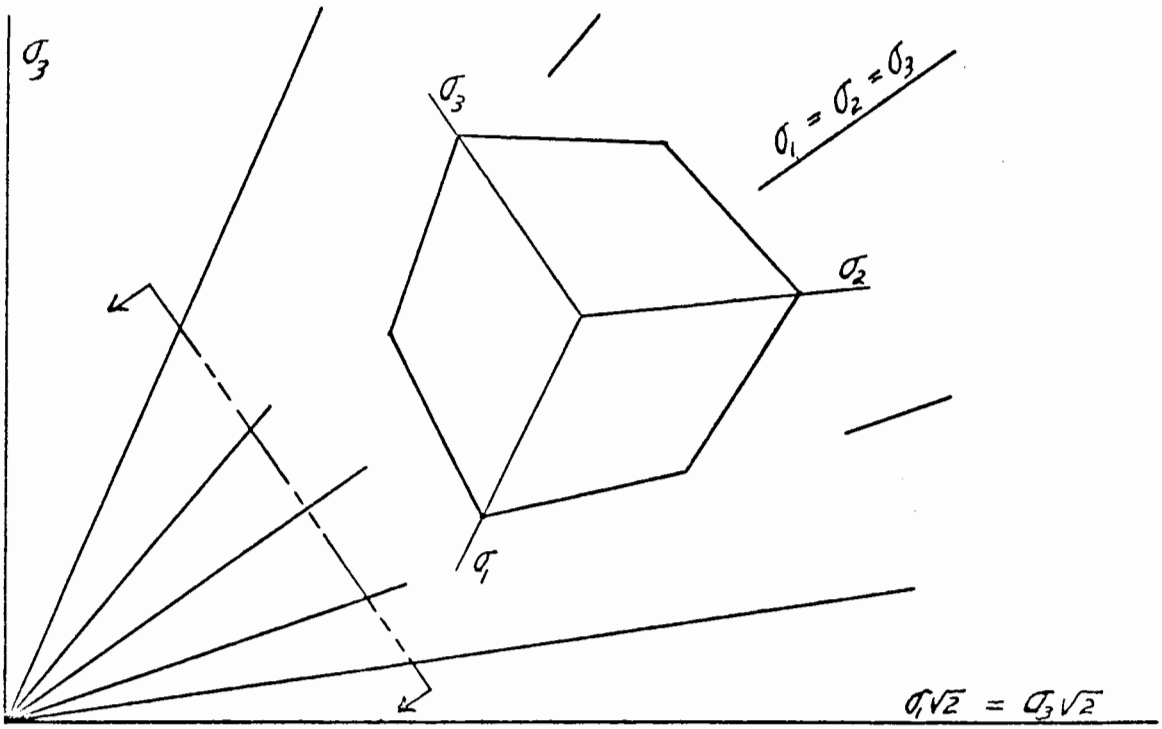

Figure 2: Three-Dimensional Failure Surface

and that ϕ corresponds to a so-called effective angle of friction. The envelope describes the limiting yield conditions of the principal stresses and satisfies the equality of equation (1); therefore a circle that is tangential to the envelope represents a stressed soil sample that is yielding, and a circle that lies within the envelope represents a stressed soil sample that is rigid. Under the stated conditions, it is impossible for the stresses to be arranged such that a Mohr circle intersects the envelope.

In terms of the principal stresses, failure occurs when

$$2c\cos\phi + (\sigma_1 + \sigma_3)\sin\phi = \sigma_1 - \sigma_3. \qquad (2)$$

Considering cohesionless soil, $c\cos\phi$ must equal zero and equation (2) reduces to

$$\sigma_1/\sigma_3 = (1 + \sin\phi)/(1 - \sin\phi). \qquad (3)$$

Equation (3) represents the maximum value of σ_1, for any σ_3 and any ϕ; however, if Figure 1 is examined, it is seen that a circle can be drawn to the left of σ_3 so that σ_1 is smaller than σ_3. This is the minimum value of σ_1 and is represented by

$$\sigma_1/\sigma_3 = (1 - \sin\phi)/(1 + \sin\phi). \qquad (4)$$

The ratios of equations (3) and (4) are recognized as defining Rankine's lateral earth-pressure coefficients. σ_1 divided by σ_3 of equation (3) is called the passive coefficient, K_p, and the same relation in equation (4) is the active coefficient, K_a.

It is known that when the limiting conditions of equilibrium are reached, the soil will fail along preferred orientations. In plane conditions, these orientations are called sliplines and form angles of $45° \pm \frac{1}{2}\phi$ with the principal or algebraically greater stress direction. Although the sliplines' directions are derived in accepted theory, the derivation will be repeated in sections following.

Three Dimensions: In real space, where the Cartesian axes are the three, mutually perpendicular, stresses, σ_1, σ_2, σ_3, the yield function takes the form of a solid that is symmetric about the space diagonal, the $\sigma_1 = \sigma_2 = \sigma_3$ axis. Hill, who presents a comprehensive study of the yield function in metal plasticity, states (page 15) that the general expression for a yield criterion is

$$f(J_1, J_2, J_3) = 0$$

with J_1, J_2, and J_3 being the first three invariants of the stress tensor σ_{ij}, and are defined in terms of the principal components of stress,

$$J_1 = \sigma_1 + \sigma_2 + \sigma_3; \; J_2 = -(\sigma_1\sigma_2 + \sigma_2\sigma_3 + \sigma_3\sigma_1); \; J_3 = \sigma_1\sigma_2\sigma_3.$$

The yield criterion can also be expressed in terms of the deviatoric stresses. That is, rather than express the stresses in relation to the origin, their magnitude can be given as the length of the perpendicular from the stress to the space diagonal. Thus the yield criterion takes the form

$$f(J_2', J_3') = 0$$

where the invariants are defined by the deviator stresses σ_1', σ_2', and σ_3'. In metal plasticity, the position of the deviatoric tensor is of no concern and therefore $J_1' = 0$. With this in mind, it is mentioned that two such yield criteria are in common use, that of Tresca

$$\sigma_1 - \sigma_3 = Y = 2k,$$

and that of von Mises

$$(\sigma_1 - \sigma_2)^2 + (\sigma_2 - \sigma_3)^2 + (\sigma_3 - \sigma_1)^2 = 2Y^2 = 6k^2.$$

Tresca's yield surface has the shape of a hexagonal prism and von Mises' is the cylinder that circumscribes this prism.

It will be accepted that a radius extending to the surface of a yield criterion can intersect it only once; also that the strain tensor representing the strain increment caused by a stress situation at the boundary must

be parallel with the normal to the yield surface at the point of stress. If the strain tensor is at a corner, a situation which is permissible, the direction of the tensor is bounded by normals to the surfaces that form the corner.

The application of the theory of a three-dimensional yield surface to soil media has been undertaken and is now widely used. An analysis of the yield function is given, in the order of development, by Drucker and Prager, 1952; Drucker, 1953; and Shield, 1955. Kirkpatrick, 1957, gives experimental evidence to substantiate this function. Because the hydrostatic pressure affects the strength of a soil, the shape of this function is a right, hexagonal pyramid. The yield function is called Mohr-Coulomb because it is derived from an extension of equation (1). All the rules, previously stated, for a yield function apply to this one; the difference, however, comes from the effect of the hydrostatic or confining pressure on the strength of the soil, and from the fact that most soils will not support tension as well as compression.

In a wholly cohesive medium, the yield function assumes the form of Tresca's hexagonal prism. The general form for a cohesionless medium, however, is given by Sokolovskii (page 7) and is

$$\left[\left|\tfrac{1}{2}(\sigma_2 - \sigma_3)\right| - \tfrac{1}{2}(\sigma_2 + \sigma_3)\sin\phi\right]\left[\left|\tfrac{1}{2}(\sigma_3 - \sigma_1)\right| - \tfrac{1}{2}(\sigma_3 + \sigma_1)\sin\phi\right]$$
$$\left[\left|\tfrac{1}{2}(\sigma_1 - \sigma_2)\right| - \tfrac{1}{2}(\sigma_1 + \sigma_2)\sin\phi\right] = 0. \qquad (5)$$

This gives a pyramid that is bounded, assuming constancy of ϕ, by the straight lines that pass through the origin and that form the angles $(1 \pm \sin\phi)/\sqrt{2}(1 \mp \sin\phi)$ with the axes $\sigma_1 = \sigma_2$, $\sigma_1 = \sigma_3$, and $\sigma_2 = \sigma_3$. The pyramid is shown in Figure 2. The intersection of the pyramid with any plane drawn at right angles to the space diagonal is a hexagon with non-parallel but equal-lengthed sides. Scott (page 313) calls this the octa-

hedral plane with an equation

$$\sigma_1 + \sigma_2 + \sigma_3 = c,$$

and states that all points on this plane have the same mean normal stress which is the octahedral normal stress,

$$\sigma_{oct} = (1/3)(\sigma_1 + \sigma_2 + \sigma_3) = c/3.$$

This normal stress is controlled only by the value of the confining pressure which also determines the distance of the plane from the origin.

It has been shown (Drucker, Sokolovskii, etc.) that the yield surface for plane conditions is an extension of the Mohr-Coulomb surface, and, also (Sokolovskii), that the directions of the slip surfaces can be obtained from this function.

Normals to the pyramidal surfaces give the directions of the strain vectors; the direction cosines of these normals are the six permutations of 1 : 0 : -k. Considering the pyramid, which is symmetric about the 1, 2 = 3 plane, the normal to the upper surface is perpendicular to that of the lower surface; also, from the direction cosines, every normal lies in a principal plane, 12, 23, or 13. Again, from the direction cosines, the equations for the normals are x - ky = 0, x - kz = 0, y - kx = 0, y - kz = 0, z - kx = 0, and z - ky = 0. Hence, for any normal, it can be said that the ratio of one axial length to the other is equal to k, or that

$$\tan\phi' = (1 - \sin\phi)/(1 + \sin\phi), \qquad (6)$$

where ϕ is the angle of internal friction from a plane analysis, and ϕ' is the angle of friction for real space.

Since the theory is to be applied to cohesionless soils, it has not been necessary to modify the yield criterion as has been suggested by Drucker and Prager, or Jenike. It will be accepted that, although ϕ may vary at low

or negative (tensile) stresses from its stated value to $\frac{1}{2}T$, with a soil that cannot support tension, a straight line or surface will adequately serve as a bound to the yield function. During plastic flow, that is steady yielding at the boundary of the yield function, and with $\phi \neq 0$, an increase of volume must result (Shield, 1954).

The Equations of Stress

The equations of stress equilibria, and thus the equations of the stress characteristics, in two dimensions, can be derived from the failure criterion. The derivation follows Scott, Appendix C, who bases his work on Sokolovskii.

If the principal stresses are oriented in a conventional co-ordinate system, as in Figure 3, such that σ_1 forms an angle ω with the x-axis, then the following equations for the stresses can be written:

$$\sigma_{xx} = (\sigma_1 \cos^2\omega + \sigma_3 \sin^2\omega) = \tfrac{1}{2}(\sigma_1 + \sigma_3) + \tfrac{1}{2}(\sigma_1 - \sigma_3)\cos 2\omega, \quad (7)$$

$$\sigma_{zz} = (\sigma_1 \sin^2\omega + \sigma_3 \cos^2\omega) = \tfrac{1}{2}(\sigma_1 + \sigma_3) + \tfrac{1}{2}(\sigma_3 - \sigma_1)\cos 2\omega, \quad (8)$$

$$\tau_{xz} = (\sigma_1 - \sigma_3)\sin\omega\cos\omega = \tfrac{1}{2}(\sigma_1 - \sigma_3)\sin 2\omega. \quad (9)$$

At conditions of failure, considering equation (2), these relations are written:

$$2\sigma_{xx} = (\sigma_1 + \sigma_3) + \cos 2\omega\,[(\sigma_1 + \sigma_3)\sin\phi + 2c\cos\phi],$$

$$2\sigma_{zz} = (\sigma_1 + \sigma_3) - \cos 2\omega\,[(\sigma_1 + \sigma_3)\sin\phi + 2c\cos\phi],$$

$$2\tau_{xz} = \sin 2\omega\,[(\sigma_1 + \sigma_3)\sin\phi + 2c\cos\phi].$$

The above relations can be rearranged and simplified by substituting the original stress for its resolved components. Thus if

$$2\sigma = \sigma_1 + \sigma_3 + 2c\cot\phi, \text{ then}$$

$$\sigma_{xx} = \sigma + \sigma\cos 2\omega\sin\phi - c\cot\phi, \quad (10)$$

$$\sigma_{zz} = \sigma - \sigma\cos 2\omega\sin\phi - c\cot\phi, \quad (11)$$

$$\tau_{xz} = \sigma\sin\phi\sin 2\omega\,. \quad (12)$$

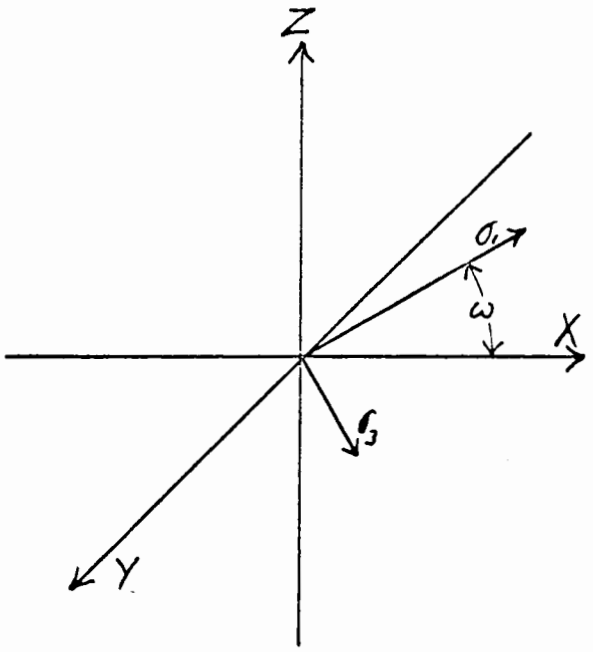

Figure 3: Cartesian Co-ordinates

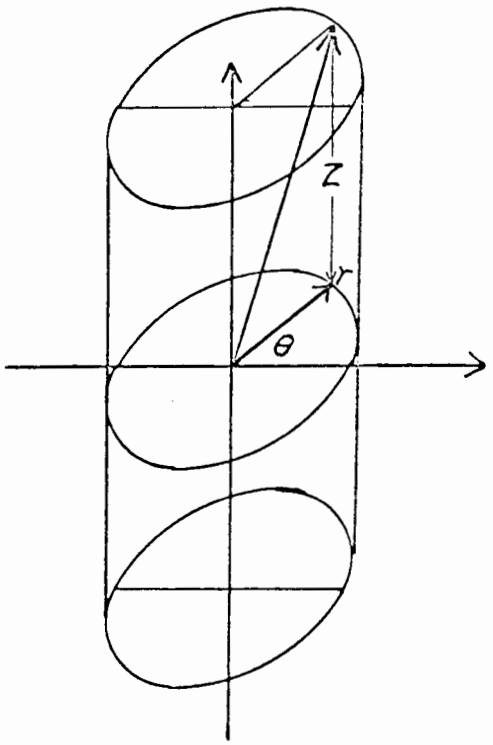

Figure 4: Cylindrical Polar Co-ordinates

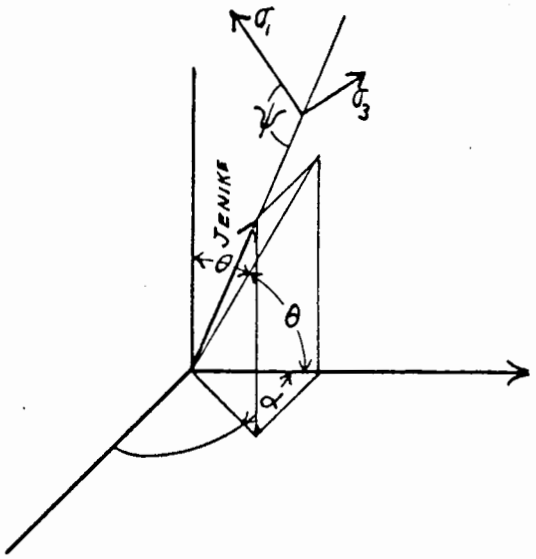

Figure 5: Spherical Polar Co-ordinates

Now that the equations of stress, at failure, are known, equations of equilibrium for steady-state flow can be written. The axes are as before so that -z is the principal stress direction, that of gravity, and x is the minor stress direction; therefore

$$\partial \sigma_{xx}/\partial x + \partial \tau_{xz}/\partial z = 0, \tag{13}$$

$$\partial \tau_{xz}/\partial x + \partial \sigma_{zz}/\partial z = -\gamma, \tag{14}$$

where γ is the bulk density of the flowing material. Substituting equations (10), (11), and (12) into the above and solving the differentials gives

$$(\partial\sigma/\partial x)(1 + \sin\phi\cos 2\omega) - (\partial\omega/\partial x)(2\sigma\sin\phi\sin 2\omega) + (\partial\omega/\partial z)$$
$$(2\sigma\sin\phi\cos 2\omega) + (\partial\sigma/\partial z)(\sin\phi\sin 2\omega) = 0, \tag{15}$$

$$(\partial\sigma/\partial x)(\sin\phi\sin 2\omega) + (\partial\omega/\partial x)(2\sigma\sin\phi\cos 2\omega) + (\partial\omega/\partial z)$$
$$(2\sigma\sin\phi\sin 2\omega) + (\partial\sigma/\partial z)(1 - \sin\phi\cos 2\omega) = \gamma. \tag{16}$$

A new function, $f(\omega, \sigma)$, is introduced to aid in the solution of the equilibrium equations. It is differentiated so that it resembles them,

$$\partial f/\partial x = (\partial f/\partial\omega)(\partial\omega/\partial x) + (\partial f/\partial\sigma)(\partial\sigma/\partial x),$$

$$\partial f/\partial z = (\partial f/\partial\omega)(\partial\omega/\partial z) + (\partial f/\partial\sigma)(\partial\sigma/\partial z).$$

There are now enough coefficients of $\partial\sigma/\partial x$, $\partial\sigma/\partial z$, $\partial\omega/\partial x$, and $\partial\omega/\partial z$ to set up a fourth-order determinant and solve it for a real solution for $f(\omega, \sigma)$,

$$\begin{vmatrix} 1 + \sin\phi\cos 2\omega & \sin\phi\sin 2\omega & -2\sigma\sin\phi\sin 2\omega & 2\sigma\sin\phi\cos 2\omega \\ \sin\phi\sin 2\omega & 1 - \sin\phi\cos 2\omega & 2\sigma\sin\phi\cos 2\omega & 2\sigma\sin\phi\sin 2\omega \\ \partial f/\partial\sigma & 0 & \partial f/\partial\omega & 0 \\ 0 & \partial f/\partial\sigma & 0 & \partial f/\partial\omega \end{vmatrix} = 0$$

Solving for $\partial f/\partial\sigma$, it is found that it equals $\pm(\partial f/\partial\omega)\cot\phi/2\sigma$, which is satisfied by

$$f = \tfrac{1}{2}\cot\phi \log(\sigma/\sigma_0) \mp \omega. \tag{17}$$

It can be seen that this is Sokolovskii's suggested function (Scott, page

510; Sokolovskii, page 26) where σ_0 is a reference stress such as cohesion. With the value of the new variable, f, retained, another determinant is created, based on the same equations, but designed to solve for $\partial\omega/\partial z$,

$$\begin{vmatrix} 1 + \sin\phi\cos 2\omega & \sin\phi\sin 2\omega & -2\sigma\sin\phi\sin 2\omega & 0 \\ \sin\phi\sin 2\omega & 1 - \sin\phi\cos 2\omega & 2\sigma\sin\phi\cos 2\omega & \gamma \\ \partial f/\partial\sigma & 0 & \partial f/\partial\omega & \partial f/\partial x \\ 0 & \partial f/\partial\sigma & 0 & \partial f/\partial z \end{vmatrix} = 0.$$

After proper manipulation, and substitution within the function f, the solution can be written

$$\pm(\partial f/\partial x)(\sin\phi + \cos 2\omega) + (\partial f/\partial z)(\cos\phi \pm \sin 2\omega) = \pm\gamma\,[\cos\phi\sin 2\omega \pm (1 + \sin\phi\cos 2\omega)]/2\sigma\sin\phi. \qquad (18)$$

By means of the substitution, $\delta = \frac{1}{4}\pi - \frac{1}{2}\phi$, equation (18) is simplified so that it can be written

$$(\partial f_+/\partial z)\cos(\omega + \delta) + (\partial f_+/\partial x)\sin(\omega + \delta) = -\gamma\sin(\omega - \delta)/2\sigma\sin\phi, \qquad (19)$$

$$(\partial f_-/\partial z)\cos(\omega - \delta) + (\partial f_-/\partial x)\sin(\omega - \delta) = \gamma\sin(\omega + \delta)/2\sigma\sin\phi. \qquad (20)$$

Equations (19) and (20) are in a form suitable for numerical solution. Further, along the set of lines with slope $dz/dx = \cot(\omega + \delta)$, the positive differential of f, df_+, is proportional to $-\gamma\sin(\omega - \delta)/2\sigma\sin\phi$; and along the set of lines with slope $dz/dx = \cot(\omega - \delta)$, the negative differential, df_-, is proportional to $\gamma\sin(\omega + \delta)/2\sigma\sin\phi$. The positive differential is equal to zero when $\omega = \delta$, thus $\omega = \frac{1}{4}\pi - \frac{1}{2}\phi$; $df_- = 0$ when $\omega + \delta = \pi$, so the negative differential is inclined as $\omega = 3\pi/4 + \frac{1}{2}\phi$. The sets of lines are the stress characteristics for plastic equilibrium and are independent of the value of c, the cohesive force.

The Equations of Strain

Having found the stress characteristics, a similar approach is used to

find the strain characteristics. It is given that the strain vector is perpendicular to the yield locus. From the pyramidal failure surface, it is seen that the principal strains are

$$\epsilon_1 = -k\sin\phi', \qquad \epsilon_3 = k\cos\phi', \tag{21}$$

where k is the relation between maximum and minimum values of σ, and where ϕ' is the angle of friction in real space. As finite strain is the displacement of an elemental length, or of an elemental volume, it may be expressed in terms of a differential:

$$\epsilon_{xx} = \partial u/\partial x, \qquad \epsilon_{zz} = \partial v/\partial z, \qquad \gamma_{xz} = \partial u/\partial z + \partial v/\partial x. \tag{22}$$

Strain in an x,z plane may also be expressed by means of the principal strains:

$$\epsilon_{xx} = \epsilon_1\cos^2\omega + \epsilon_3\sin^2\omega = \tfrac{1}{2}(\epsilon_1 + \epsilon_3) + \tfrac{1}{2}(\epsilon_1 - \epsilon_3)\cos 2\omega, \tag{23}$$

$$\epsilon_{zz} = \epsilon_1\sin^2\omega + \epsilon_3\cos^2\omega = \tfrac{1}{2}(\epsilon_1 + \epsilon_3) + \tfrac{1}{2}(\epsilon_3 - \epsilon_1)\cos 2\omega, \tag{24}$$

$$\gamma_{xz} = (\epsilon_1 - \epsilon_3)\sin 2\omega = (\epsilon_1 - \epsilon_3)2\sin\omega\cos\omega. \tag{25}$$

To have enough equations to solve for all the variables, several more are devised which describe the strain motion. First are the equations of the total differential,

$$du = (\partial u/\partial x)dx + (\partial u/\partial z)dz, \tag{26}$$

$$dv = (\partial v/\partial x)dx + (\partial v/\partial z)dz; \tag{27}$$

then the equation for the displacement of an elemental length in the x-direction, which is obtained by substituting equations (21) and (22) into (23),

$$\partial u/\partial x = \tfrac{1}{2}k\left[(\cos\phi' - \sin\phi') - (\cos\phi' + \sin\phi')\cos 2\omega\right],$$

in which the trigonometric functions are set equal to α, so that

$$\partial u/\partial x = \tfrac{1}{2}\alpha k; \tag{28}$$

then the equation for the displacement in the z-direction,

$$\partial v/\partial z = \tfrac{1}{2}k\left[(\cos\phi' - \sin\phi') + (\cos\phi' + \sin\phi')\cos 2\omega\right],$$

which is shortened by using β for the trigonometric functions, so that

$$\partial v/\partial z = \pm\beta k; \tag{29}$$

and finally there is an equation for strain equilibrium,

$$\beta(\partial u/\partial x) - \alpha(\partial v/\partial z) = 0. \tag{30}$$

Using the relationship

$$(\partial u/\partial x) - (\partial v/\partial z) = \cot 2\omega[(\partial u/\partial z) + (\partial v/\partial x)],$$

(which is a subtraction of terms equivalent to those in equations (23) and (24)) and equations (26), (27), and (30), a determinant is created,

$$\begin{vmatrix} 1 & -\cot 2\omega & -\cot 2\omega & -1 \\ dx & 0 & dz & 0 \\ 0 & dx & 0 & dz \\ \beta & 0 & 0 & -\alpha \end{vmatrix} = 0,$$

and a new equation formed

$$(dz)^2\beta \cot 2\omega + dzdx(\alpha - \beta) + (dx)^2\alpha \cot 2\omega = 0,$$

which can be solved for dz/dx. This yields, upon solution of the quadratic and resubstitution of the trigonometric functions for α and β,

$$dz/dx = [(\cos\phi' + \sin\phi')\sin 2\omega \pm 2(\cos\phi'\sin\phi')^{\frac{1}{2}}]/$$
$$[(\cos\phi' - \sin\phi') + (\cos\phi' + \sin\phi')\cos 2\omega]. \tag{31}$$

At dz/dx = 0, which represents the limit of the strain field, it is drawn from equation (31) that

$$(\cos\phi' + \sin\phi')\sin 2\omega = \pm 2(\cos\phi'\sin\phi')^{\frac{1}{2}},$$

which simplifies to

$$\cos 2\omega = \pm\tan(\tfrac{1}{4}\pi - \phi').$$

Recalling equation (6), the above expression for cos 2ω can be reduced to $\pm\sin\phi$ or

$$\omega = \pm\tfrac{1}{4}\pi \pm \tfrac{1}{2}\phi. \tag{32}$$

Equation (31) is the value of the strain characteristic and equation (32) is the characteristic direction. Inasmuch as no concern was given to dilatancy, one cannot expect that this description will be accurate throughout the failing region. However, it is assumed to be valid at the boundary between material in motion and stationary material. Thus these strain characteristics are valid for incipient failure and are useful for the theory at hand. This derivation is similar to one that Jenike, 1961, gives for incipient failure (page 138).

Transformation of Axes

In order to adapt the theory of characteristics to the situation of converging flow, it is best to transform the results into the form they take in polar co-ordinates. The simplest change is to cylindrical polar co-ordinates, Figure 4, page 12, with azimuthal symmetry, where r is the horizontal radius vector, θ is the angle of the vector with the polar axis, and z is the vertical height of the cylinder in question. Shear, τ, in any plane but the r, z is equal to zero. Thus the equations of equilibrium, equations (13) and (14), become

$$(\partial \sigma_{rr}/\partial r) + (\partial \tau_{rz}/\partial z) + (\sigma_{rr} - \sigma_{\theta\theta})/r = 0,$$
$$(\partial \tau_{rz}/\partial r) + (\partial \sigma_{zz}/\partial z) + (\tau_{rz}/r) = -\gamma.$$

The shear relations are transformed in a similar manner:

$$\epsilon_{rr} = \partial u/\partial r, \quad \epsilon_{\theta\theta} = u/r, \quad \epsilon_{zz} = \partial w/\partial z, \quad \gamma_{rz} = (\partial u/\partial z) + (\partial w/\partial r).$$

Another form of co-ordinates, perhaps more useful, is spherical polar co-ordinates, Figure 5, page 12. An angle, ψ, is introduced which is the angle between the principal stress, σ_1, and the radius vector, r. θ is the vertical angle that r makes with the horizontal axis, and α is the angle made by the horizontal component of the vector with the polar axis. In terms

of the average stress, σ, all the component stresses can be defined,

$$\sigma_{rr} = \sigma(1 + \sin\phi\cos 2\psi), \quad \sigma_{\theta\theta} = \sigma(1 - \sin\phi\cos 2\psi), \quad \tau_{r\theta} = \sigma\sin\phi\sin 2\psi. \tag{33}$$

Therefore, the equations of equilibrium become

$$(\partial\sigma_{rr}/\partial r) + (\partial\tau_{r\theta}/r\partial\theta) + [(\sigma_{rr} - \sigma_{\theta\theta}) + m(\sigma_{rr} - \sigma_{\alpha\alpha}) + m\tau_{r\theta}\cot\theta]/r - \gamma\sin\theta = 0, \tag{34}$$

$$(\partial\tau_{r\theta}/\partial r) + (\partial\sigma_{\theta\theta}/r\partial\theta) + [m(\sigma_{\theta\theta} - \sigma_{\theta\theta})\cot\theta + (2 + m)\tau_{r\theta}]/r + \gamma\cos\theta = 0, \tag{35}$$

with $m = +1$ for axial symmetry and $m = 0$ for plane symmetry. The latter is the case that Sokolovskii presents on page 219 and gives his equation in polar co-ordinates for equilibrium. The former is Hill's equation for equilibrium in spherical polar co-ordinates, page 344, but with body weight. The condition of limiting equilibrium, a variant of equation (2) becomes

$$\tfrac{1}{4}(\sigma_{rr} - \sigma_{\theta\theta})^2 + \tau_{r\theta}^2 = \tfrac{1}{4}\sin^2\phi(\sigma_{rr} + \sigma_{\theta\theta})^2. \tag{36}$$

The Theory of a Wedge

As the theory evolves toward describing converging, axially symmetric flow, it becomes obvious that Sokolovskii's derivation of the limiting equilibrium of a wedge must be reviewed. If the polar co-ordinates are superimposed over the cartesian ones such that the origins coincide, it can be seen that

$$\psi = \omega - \theta$$

where ω is the angle the principal stress makes with the x-axis and θ is the angle of the ray, r, with the x-axis.

The assumption is made that σ is proportional to r, and that ω and ψ depend only on θ. Therefore $\omega = \omega(\theta)$, $\psi = \psi(\theta)$, and a new function $s = s(\theta)$ is introduced which is defined by

$$\sigma = \gamma r s(\theta). \tag{37}$$

Thus equations (33) which satisfy the condition of equation (36) are substituted into equations (34) and (35). Using equation (37), and rearranging, the following equations of equilibrium are obtained

$$\sin\phi\sin2\psi\, ds/d\theta + 2s\sin\phi\cos2\psi((d\psi/d\theta) + 1) + s(1 + \sin\phi\cos2\psi) = \sin\theta,$$

$$(1 - \sin\phi\cos2\psi)ds/d\theta + 2s\sin\phi\sin2\psi((d\psi/d\theta) + 1) + s\sin\phi\sin2\psi = -\cos\theta.$$

With two equations and two unknowns, a solution is easily obtained for the derivatives, which are

$$ds/d\theta = -[s\sin2\psi + \cos(\theta + 2\psi)]/(\cos2\psi - \sin\phi), \tag{38}$$

$$(d\psi/d\theta) + 1 = [-\sin\theta + \sin\phi\sin(\theta + 2\psi) + s\cos^2\phi]/$$

$$2s\sin\phi(\cos2\psi - \sin\phi). \tag{39}$$

Since the two families of sliplines intersect each other at an angle

$$2\delta = \tfrac{1}{2}\pi - \phi,$$

it is seen that the denominators become zero when $\psi = \pm\delta$. The sliplines are inclined to the x-axis at angles $\omega \mp \delta$, and to the ray, r, at angles $\psi \mp \delta$. Therefore the differential equations of the sliplines are

$$dz/dx = \tan(\omega \mp \delta), \qquad rd\theta/dr = \tan(\psi \mp \delta),$$

which give

$$r = C\exp\int_0^\theta \cot(\psi \mp \delta)d\theta. \tag{40}$$

Equation (40) is seen to be a definition of logarithmic spirals. Thus the stress characteristics in a wedge are the two families of spirals formed by this equation.

Sokolovskii considers the special case of a medium without weight. In this case, it is assumed that σ is proportional to a power function of r and equation (37) becomes

$$\sigma = r^n s(\theta). \tag{41}$$

Equations (38) and (39) reduce to

$$ds/d\theta = ns\sin 2\psi/(\cos 2\psi - \sin\phi),$$

$$(d\psi/d\theta) + 1 = -n\cos^2\phi/2\sin\phi(\cos 2\psi - \sin\phi);$$

the equations of the sliplines becomes

$$r^n s \exp[\mp 2(\theta + \psi)\tan\phi] = C. \qquad (42)$$

The rule that the characteristics intersect at angles of 2δ is satisfied by equations (40) and (42). The bisectors of the intersections of the characteristics give the directions of the principal stress at each point. Further, if a fan of straight lines is superimposed over the isogonal net, along one ray the characteristics will intersect the ray at equal angles. This geometry is sketched in Figure 6.

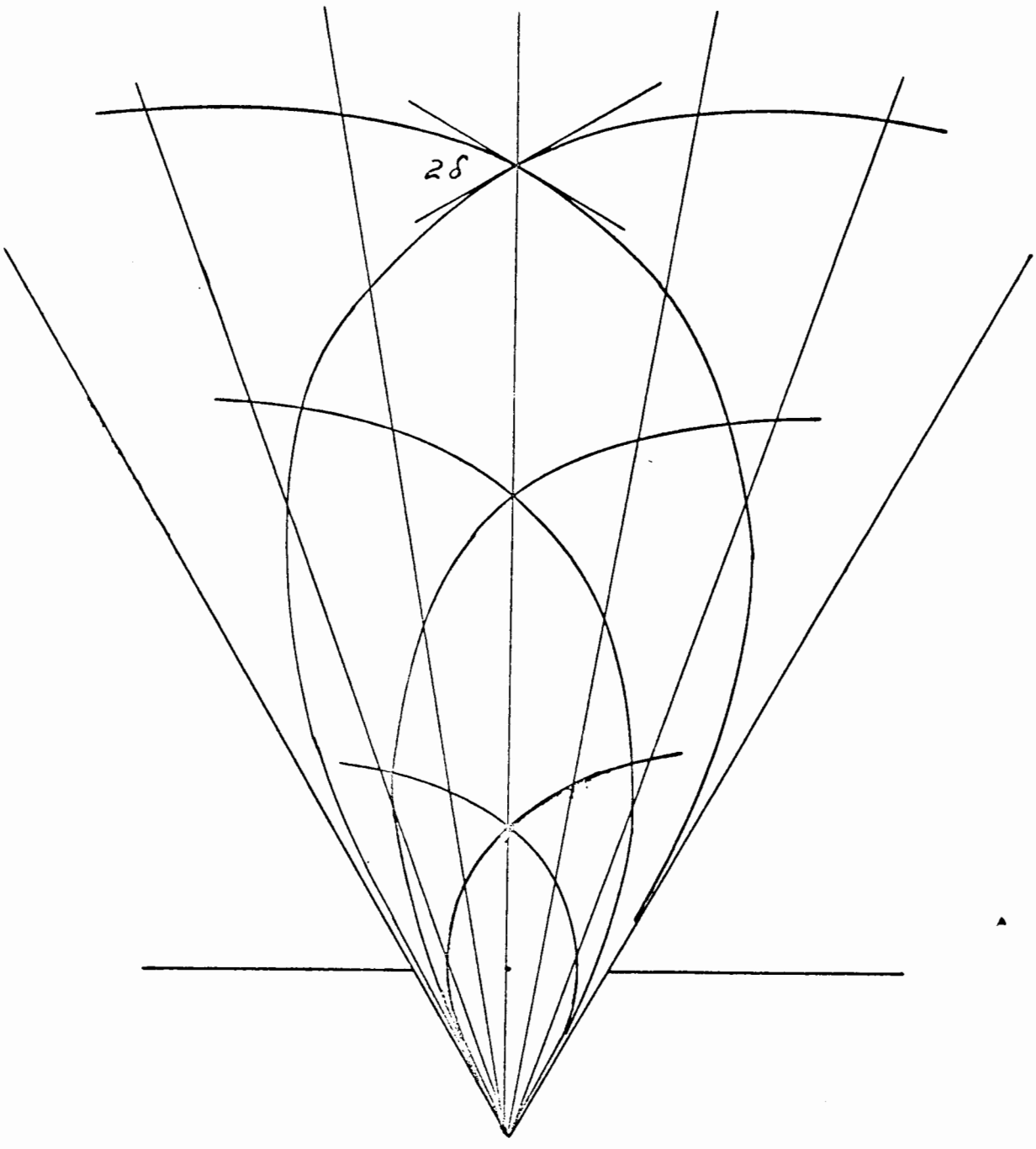

Figure 6: Sliplines in a Radial Wedge

RECENT WORK ON CONVERGING FLOW

The Slipline Field

Jenike and Johanson: Any discussion of flow within granular material would be severely limited without including the work of Jenike and his associates. In a long report, published in 1961, he examined closely many of the ramifications of failure and flow in bulk solids. Although he looks into such things as the yield surface, and proposes an effective yield locus for cohesive material and a wall yield locus for failure at a rigid wall, his most important contribution was to transform Sokolovskii's theory of a wedge into a theory suitable for cases of axial symmetry. Thus Jenike has used equations (34) and (35) with $m = +1$ (unlike Sokolovskii who solves only the plane case) to obtain equations equivalent to (38) and (39). He further assumes that, unlike equation (37), the density is dependent upon the stress and thus upon θ, so that throughout the failing region the stress can be defined,

$$\sigma = r\, \gamma(r, \theta)\, s(r, \theta). \tag{43}$$

Remembering that he defines θ as the angle the principal stress makes with the vertical axis, he rearranges and separates his derivatives so that two complicated equations for $\partial s/\partial\theta$ and $\partial s/\partial r$ result. If the stress field near to the vertex of the converging channel is considered however, it is assumed that it is radial, that γ is constant, and that $s = s(\theta)$. The differential equations (in Jenike's geometry where θ is the angle with the vertical) then become

$$ds/d\theta = \left\{s \sin 2\psi + \sin(\theta + 2\psi) + ms \sin\phi \left[\cot\theta(1 + \cos 2\psi) - \sin 2\psi\right]\right\}/ (\cos 2\psi - \sin\phi), \tag{44}$$

$$(d\psi/d\theta) + 1 = -\left[ms \sin\phi(1 + \sin\phi)(\cot\theta \sin 2\psi + \cos 2\psi - 1) + \cos\theta - \sin\phi\cos(\theta + 2\psi) + s\cos^2\phi\right]/\left[2s \sin\phi(\cos 2\psi - \sin\phi)\right]. \tag{45}$$

Jenike's geometry, used to develop equations (44) and (45), deviates from that in Figure 5 such that the equilibrium equations now have reversed trigonometric functions of θ and reversed signs. At the boundary of flow, or the zone of incipient failure, γ is considered constant and thus equations (44) and (45) are valid as bounding the flow.

Jenike proposes values of s and $s_o = s(\theta = 0)$ for various values of effective angle of internal friction and for various values of angle of wall friction. From the Mohr's diagram of wall yield loci, he relates ψ' (ψ at the wall) to ϕ' (angle of wall friction) by

$$\psi' = \tfrac{1}{2}\pi + \tfrac{1}{2}(\phi' + \text{Arcsin}(\sin\phi'/\sin\delta)), \qquad (46)$$

where δ is the effective angle of friction and is always larger than ϕ, or, in the case of cohesionless material, equal to ϕ. Jenike's angle of wall friction should not be confused with the previously developed angle of friction for real space. Thus starting from the condition $\theta = 0$ and $\psi = \tfrac{1}{2}\pi$ he obtains arbitrary values of s_o and by machine integration of equations (44) and (45) proceeds to plot s_o for any θ and ψ'. Along loci of s_o, positions of various values of s are plotted and then connected to form equal contours of s.

Therefore, on these curves of the function s for given δ, a point can be plotted that corresponds to given wall conditions (θ' and ϕ'); in turn this point will lie on a trajectory of s_o. The trajectory of s_o gives the relation between ψ and θ for the given wall conditions. In other words, Jenike has introduced a method of determining the direction of the principal stress in regard to a ray, for any ray in a radial stress field.

From continuity equations, and considering the flowing material to be incompressible, Jenike shows (1961, pages 119 - 124) that the ratio of the velocity along any slipline to the velocity at $\theta = 0$ is given by

$$V/V_o = e(\exp -3\int_0^{\theta} \tan 2\psi \, d\theta). \qquad (47)$$

Velocity profiles can be calculated from this equation, but they show that there must be a velocity discontinuity at $\theta = \frac{1}{4}\pi$ or $3\pi/4$.

Jenike gives some criteria for piping and they will be discussed in a separate section.

Gardner: One of Gardner's latest papers sets an interesting approach to determining the slipline field. He works with plane strain symmetry and divides his flowing region into three portions. The first is the region along and above the bound between steady plastic flow (such as is found between parallel walls or in a bin) and converging flow. In this region the average stress σ (he defines it as a pressure) is related to the stress at $\theta = 0$ by

$$\sigma/\sigma_o = (1 + \sin\phi)\left[1 + (x/\lambda)^2\tan^2\phi\right]/\left[1 + \sin\phi(1 - (x/\lambda)^2)^{\frac{1}{2}}\right], \qquad (48)$$

where $\lambda = x$ at the wall. In the nomenclature of this report, the angle between the x-direction and the principal stress is given by

$$\cos 2\omega = \left[-(x/\lambda)^2\sin\phi + \cos^2\phi(1 - (x/\lambda)^2)^{\frac{1}{2}}\right]/\left[\cos^2\phi + (x/\lambda)^2\sin^2\phi\right]. \qquad (49)$$

The sliplines in this region are given by

$$dz/dx = \tan(\omega + \delta), \quad \delta = \tfrac{1}{4}\pi - \tfrac{1}{2}\phi, \qquad (50)$$

along which the function $\xi = \frac{1}{2}\cot\phi \log(\sigma/\sigma_o) + \omega$ exists.

The second region is based on a radial stress system for material without weight and is the region of theoretical converging flow. The vertical length, OD, of this region above the apex of the wedge is given by

$$OD/\lambda = \cot\phi/s_o(1 + \sin\phi), \qquad (51)$$

where s_o is determined from Jenike's curves of the function s by knowledge of the angle the wall makes with the center-line and of the angle of wall friction. The bound to this region is given by the slipline

$$dz/dx = \tan(\omega - \delta), \qquad (52)$$

along which the function $\epsilon = \frac{1}{2}\cot\phi \log(\sigma/\sigma_o) - \omega$ exists. By combining equations (51) and (52) to give length and direction, the bound to the radial field can be plotted.

The third region connects the zone of steady flow to the zone of converging flow and its sliplines follow the directions imparted by equations (50) and (52). The actual placement of the sliplines in this region is done by moving from the established bounds of regions one and two by means of Hencky's theorems.

Gardner relies upon Sokolovskii and Jenike for the origins of his theory, but manages to create a slipline field that is uniquely his own. In particular, the second region is akin to Sokolovskii's failure of a wedge, however, the important difference is that Gardner puts a bound on his wedge and shows how it influences the sliplines within the wedge.

Pariseau: One other worker, Pariseau, is mentioned for his work in establishing slipline theory. In a carefully prepared report he gives a derivation of slipline theory for plane strain, extending Hill's mathematical work on metal plasticity to soil mechanics, and from this theory predicts pressures on the walls and base of the container of the flowing material. His experiments then measured the pressures actually occurring and substantiated the hypothesis that stress sliplines control the flow in a bulk solid.

Flow-Rate Theory

General: A case has been founded for establishing a flow-field, wherein the field is based on sliplines as predicted by plasticity theory. Extensions of this theory will be discussed in a section devoted to new theory. The object now is to lay some foundations for a theoretical method that will

determine flow rate.

Minimum Energy, Brown: One method of determining flow rates is based on the assumption that there must be a decrease in energy within the flowing material as it converges toward an aperture. A theoretical minimum for the energy is devised, applied to the velocity, and a flow rate is obtained.

The originator of this line of reasoning is R. L. Brown. He develops the flow rates as stated, but makes no allowance for variable flow-field. It is hoped that this minimum-energy theory can be developed and then applied to the flow-field theory so as to obtain a total picture of flow. The theory works only where there is no cohesion.

If radial flow, of either cylindrical or spherical nature, is considered, such that the flow can be said to be in stream-tubes along the lines of the rays, R, and at angles, θ, to the center-line, and if v is the velocity within the tube normal to its area dA, then the flow rate is

$$Q = \gamma v = mN, \tag{53}$$

where m is the weight of a granule, and N is the number of granules per unit area per unit time. The situation is sketched in Figure 7. The total flow-field is bounded by a ray which is at an angle θ' to the vertical. It is noted that D', the effective diameter of the aperture is used rather than the actual diameter; they are related by

$$D' = D - nd, \tag{54}$$

where n is found to be most nearly 2 by experiment and d is the particle diameter. From Figure 7, D' can be redefined

$$D' = 2R_o \sin\theta'. \tag{55}$$

A new function, $f(\theta) = NR^2$, is introduced so that the total mass rate of flow in conical geometry is given by

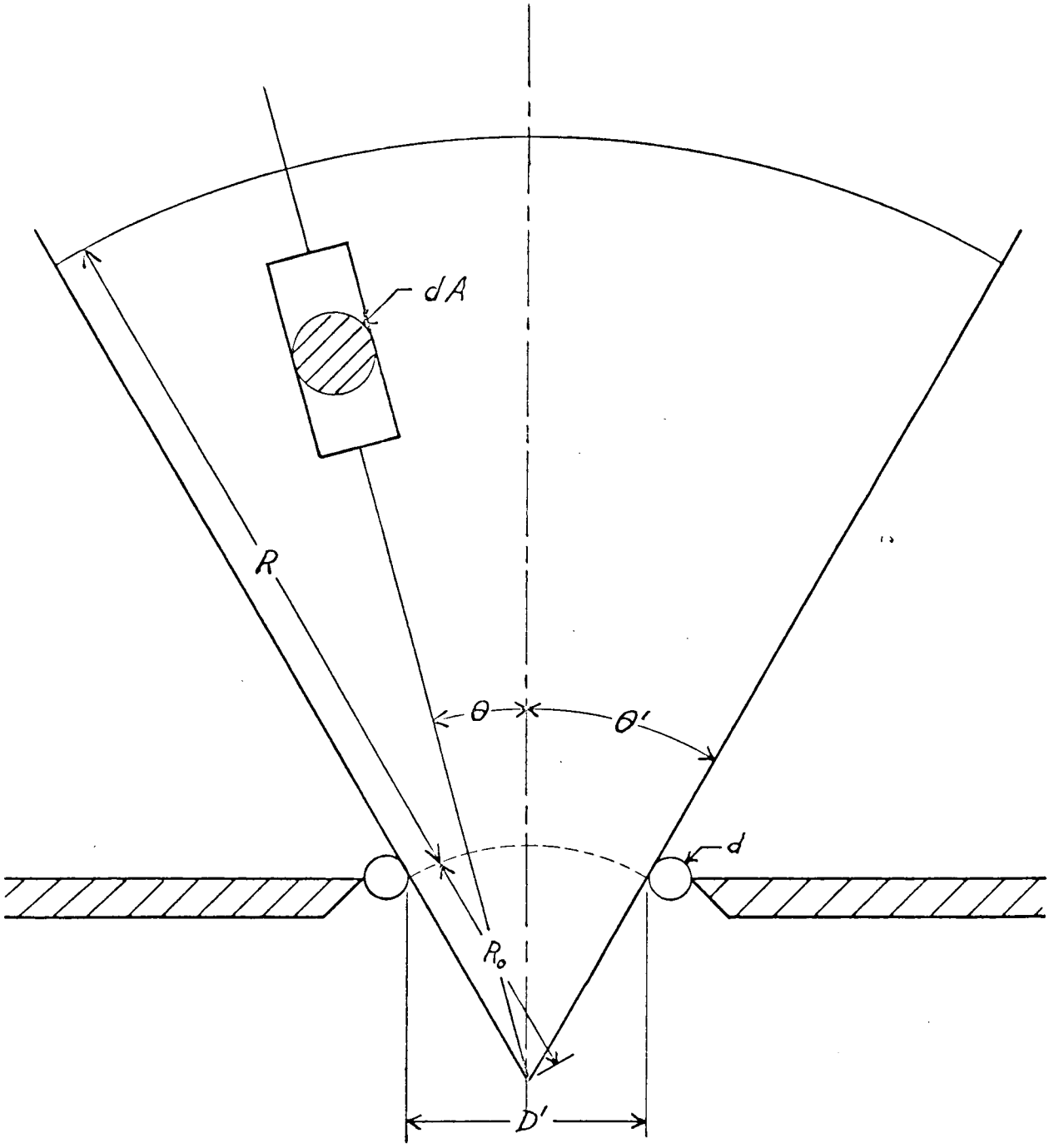

Figure 7: Flow-Field Geometry

$$Q = 2\pi m \int_0^{\theta'} f(\theta)\sin\theta d\theta. \qquad (56)$$

In wedge geometry, that is flow from a trough, a function $g(\theta) = NR$ is introduced and the total mass rate is given by

$$Q = 2ml' \int_0^{\theta'} g(\theta)d\theta, \qquad (57)$$

where $l' = l - 2d$ is the slit length and $S' = S - 2d = 2R_o\sin\theta'$ is the slit width.

With an expression for the flow at hand, the energy theory is now established. The total energy, T, which is a combination of kinetic and potential energy, is

$$2T = \gamma(v^2 + 2gR\cos\theta). \qquad (58)$$

Inasmuch as the stream-tubes converge, the total energy must decrease continuously along their length; the excess energy being dissipated by collisional, rotational, and frictional losses. Obviously, T cannot decrease beyond a minimum, but it is assumed that it reaches this minimum just at the point of egress. This being so,

$$\partial[(Q^2/\gamma^2) + 2gR\cos\theta]/\partial R = 0, \text{ for } R = R_o, \text{ or}$$

$$(m^2/\gamma^2)(N\partial N/\partial R)_{R=R_o} + g\cos\theta = 0. \qquad (59)$$

From the above, equation (56), and the substitution for $f(\theta)$, the total rate for conic flow

$$Q = 2\pi R_o^{2.5}\gamma(\tfrac{1}{2}g)^{\frac{1}{2}}\int_0^{\theta'}(\cos\theta)^{\frac{1}{2}}\sin\theta d\theta \qquad (60)$$

is obtained. From equations (59) and (57), and the expression for $g(\theta)$, a similar expression for flow from a trough is obtained:

$$Q = 2l'R_o^{1.5}\gamma g^{\frac{1}{2}}\int_\theta^{\theta'}(\cos\theta)^{\frac{1}{2}}d\theta. \qquad (61)$$

These expressions are simplified and transformed into more workable units by the introduction of two dimensionless quantities. The first is for conical flow, and the second for flow from a trough

$$q_1 = 4Q/\gamma\pi D'^2(gD')^{\frac{1}{2}}, \quad (62a), \qquad q_2 = Q/\gamma l'S'(gS')^{\frac{1}{2}}. \quad (62b)$$

Using these quantities and substituting for Q, two new expressions, which define the flow, are derived. Thus

$$q_1 = 2(1 - \cos^{1.5}\theta')/3\sin^{2.5}\theta' \text{ for conical flow, and} \quad (63)$$

$$q_2 = \int_0^{\theta'} \cos^{\frac{1}{2}}\theta d\theta/2^{\frac{1}{4}}\sin^{1.5}\theta' \text{ for flow from a trough.} \quad (64)$$

From the last three equations one can now predict the flow rate of granular material from a flat-bottomed vessel if the radial bound to the flow-field is known.

There are some disadvantages to this theory. The first is that γ is considered constant along all the stream-tubes. That is Brown has not considered change of density with R, or

$$\partial\left[(m^2N^2/\gamma^2) + 2gR\cos\theta\right]/\partial R = (2m^2/\gamma^2)(N\partial N/\partial R) + 2g\cos\theta - (2m^2N^2/\gamma^3)(\partial\gamma/\partial R).$$

This equation, similar to (59), introduces a term for variable density. Rearranging, and neglecting any density variations with θ, there is obtained a new definition of $f(\theta)$,

$$f(\theta) = \left[\gamma^2R^5g\cos\theta/2m^2(1 + (R/2\gamma)(\partial\gamma/\partial R))\right]^{\frac{1}{2}}.$$

From the notion of continuous expansion, or plastic potential, it is reasonable to suppose that γ decreases with R so that the flow rate would be less than given by the Brown theory.

Another difficulty of the theory is that it is suitable for only one value of θ'. The following derivation explains this situation. The quantity q_1 is examined for its minima,

$$\partial q_1/\partial\theta \propto (3\sin\theta'\cos^{\frac{1}{2}}\theta'/2\sin^{2.5}\theta') - \left[5\cos\theta'(1 - \cos^{1.5}\theta')/2\sin^{3.5}\theta'\right].$$

The differential is zero when

$$3\sin^2\theta'\cos^{\frac{1}{2}}\theta' = 5\cos\theta'(1 - \cos^{1.5}\theta'), \text{ or}$$

$$3 + 2\cos^2\theta' = 5\cos^{\frac{1}{2}}\theta'$$

One root of this is

$$\cos^{\frac{1}{2}}\theta' = 0.692, \text{ or}$$

$$\theta' = 61.4^{\circ}.$$

Thus q_1, and hence the conical flow rate, Q, is at a minimum when $\theta' = 61.4^{\circ}$. This delineates, under Brown's theory, the boundary of any radial velocity field, no matter what the state of flowing material.

One further point is in regard to minimum energy, and its use in a consistent flow pattern. Obviously, it can be used to set a bound to the flow rate, but the question is whether it can be attained along all values of θ. From equation (60) it is drawn that the velocity

$$v(\theta) \propto (\cos\theta)^{\frac{1}{2}},$$

hence $v \neq 0$ when $\theta = \theta'$. Further, the velocity profile corresponding to this relation is quite different from one that is drawn from Jenike's theory (equation (47)). It is therefore assumed that the minimum energy cannot be applied along all values of θ. A redeeming note, however, is that along $\theta = 0$, a minimum is probably obtained so that it can be applied to obtain a v_o from equation (60) that is used in equation (47) to generate all values of $v(\theta)$.

Savage: Another theory based on wall conditions is that presented by Savage. He couples the velocity field to that of stress and produces one equation to describe motion equilibrium,

$$(\partial \sigma_{rr}/\partial r) + (m + 1)(\sigma_{rr} - \sigma_{\theta\theta})/r - \gamma g = g\, u\, du/dr,$$

where $m = +1$ for axial symmetry and 0 for plane-strain, and where u is the velocity component in the r-direction. From the continuity equation

$$d(r^{1+m}u)/dr = 0, \text{ is obtained}$$

$$u = A/r^{1+m}.$$

Remembering that $k = (1 + \sin\phi)/(1 - \sin\phi)$, and with some manipulation of

the above equations, and using the boundary condition of zero stress at the orifice and the top-free surface, an equation is produced for the velocity along any stream-tube at the orifice,

$$u \cong -\left\{(1 + k)gD'/2\left[(k - 1)(m + 1) - 1\right]\sin\theta'\right\}^{\frac{1}{2}}.$$

From the velocity equation is drawn an equation for the flow rate through a circular orifice, and within walls that have an angle θ' with the vertical,

$$W \cong \tfrac{1}{4}\pi\gamma D'^{2.5}g^{\frac{1}{2}}\left[(1 + k)/2(2k - 3)\sin\theta'\right]^{\frac{1}{2}}. \qquad (65)$$

Savage's initial equation for motion equilibrium is similar to the equations presented on page 17 except he has included terms that describe inertia effects. Therefore, in this respect, his combined theory goes further than Brown's in that it includes this advanced step. However, Savage does not consider a change of velocity with θ, as has both Brown and Jenike, and thus presents a theoretical case of unchanging velocity profile. Savage's theory cannot work when θ in his velocity equation is set greater than the natural bound, θ', for the flowing material. Because of the implication of zero stress at the orifice and at the free surface of the flowing material this theory vindicates the assumption that flow rate does not depend upon head.

APPLICATIONS TO RADIAL THEORY

The Radial Bound

In three dimensions, because of the complexity of equations and variables, it is difficult to solve for the parameters of stress and strain. Therefore, in an attempt to delineate flow in a conical situation the equations of Jenike will be re-examined for possible solutions of θ'. The object of this section, then, is to determine some possible bounds to the radial flow-field in axial symmetry. Empirical evidence will be called upon to deduce the proper bound and to justify assumptions. Although flow in plane-strain is examined experimentally, the theory of Gardner appears to give a good description of his observations. For this reason, the theory described will not go deeply into plane-strain.

The foremost assumption is that the flow-field is radial, generated from an apex somewhere beneath the orifice, and that the physical bound to the field (viewed in section) is a straight line. The equations that are to be produced represent an extension to the theory of Jenike. If equations (44) and (45), which are valid at the flow boundary, are recalled, then it will be useful to examine solutions to these equations near $\theta = 0$ and $\psi = \psi_0$ as s approaches zero. Using the substitutions, made possible by these limits, $s = \theta(ds/d\theta)_0$ and $\psi = \psi_0 + \theta(d\psi/d\theta)_0$, and with $n = 1$ there is produced the equation

$$(ds/d\theta)_0 = \{\theta(ds/d\theta)_0 \sin 2\psi_0 + \sin 2\psi_0 + 2\theta\cos 2\psi_0 (d\psi/d\theta)_0 + [\theta(ds/d\theta)_0 \sin\phi]$$
$$[((1 + \cos 2\psi_0)/(\theta)) - 2\sin 2\psi_0 (d\psi/d\theta)_0 - \sin 2\psi_0] / [\cos 2\psi_0 - \sin\phi -$$
$$2\sin 2\psi_0 (d\psi/d\theta)_0 \theta].$$

With $(d\psi/d\theta)$ finite and taking into account that $\theta = 0$, this reduces to

$$(ds/d\theta)_0 = \sin 2\psi_0 / [\cos 2\psi_0 (1 - \sin\phi) - 2\sin\phi]. \qquad (66)$$

In a similar fashion, there is produced

$$(d\psi/d\theta)_o + 1 = -\{\theta(ds/d\theta)_o \sin\phi(1 + \sin\phi)[((\sin 2\psi_o)/(\theta)] + 2\cos 2\psi_o (d\psi/d\theta)_o$$
$$+ \cos 2\psi_o - 1] + 1 - \sin\phi\cos 2\psi_o + 2\sin\phi\sin 2\psi_o (d\psi/d\theta)_o \theta +$$
$$(\cos^2\phi)\theta(ds/d\theta)_o\} / [\cos 2\psi_o - \sin\phi - 2\sin 2\psi_o (d\psi/d\theta)_o \theta](2\sin\phi)\theta(ds/d\theta)_o.$$

For a finite $(d\psi/d\theta)_o$, and with $(ds/d\theta)_o$ given as in equation (66), this reduces to

$$\sin\phi(1 + \sin\phi)\sin^2 2\psi_o = (1 - \sin\phi\cos 2\psi_o)\cos 2\psi_o - \sin\phi\cos 2\psi_o - 2\sin\phi,$$

which is solved for $\cos 2\psi_o$

$$\cos 2\psi_o = \sin\phi \text{ or } (1 - \sin\phi)/2\sin\phi.$$

The first alternative is rejected, and the second gives

$$\cos 2\psi_o = (1 - \sin\phi)/2\sin\phi. \qquad (67)$$

It can be shown that equation (67) forms the asymptote to Jenike's curves of the function s plotted on co-ordinates of ψ and θ for particular ϕ. Further, it is seen that one solution for $(d\psi/d\theta)_o$ is -1 and that this represents the slope of these asymptotic curves. Therefore, one solution for $\psi = \psi_o + \theta(d\psi/d\theta)_o$ is $\psi_o - \theta$. Equation (67) can be solved for all values of ϕ greater than $\sin^{-1} 1/3$.

If the geometry of this situation (which follows Jenike's) is recalled, where ψ is the angle made by the principal stress, σ_1, with the ray, r, which deviates from the vertical by the angle θ, and if it is recalled that slip-lines exist at angles $\delta = \frac{1}{4}\pi \pm \frac{1}{2}\phi$ to σ_1, then there is a possible radial slip-field for

$$\psi + \tfrac{1}{4}\pi \pm \tfrac{1}{2}\phi = \pi, \text{ which gives}$$
$$\psi = 3\pi/4 \pm \tfrac{1}{2}\phi. \qquad (68)$$

From equation (67), and from $(d\psi/d\theta)_o = -1$, the graph in Figure 8 may be plotted. The lines plotted in this graph represent s = 0, or are the asymptotes to the curves in figures 34 - 38 (Jenike, 1961). These asymptotes

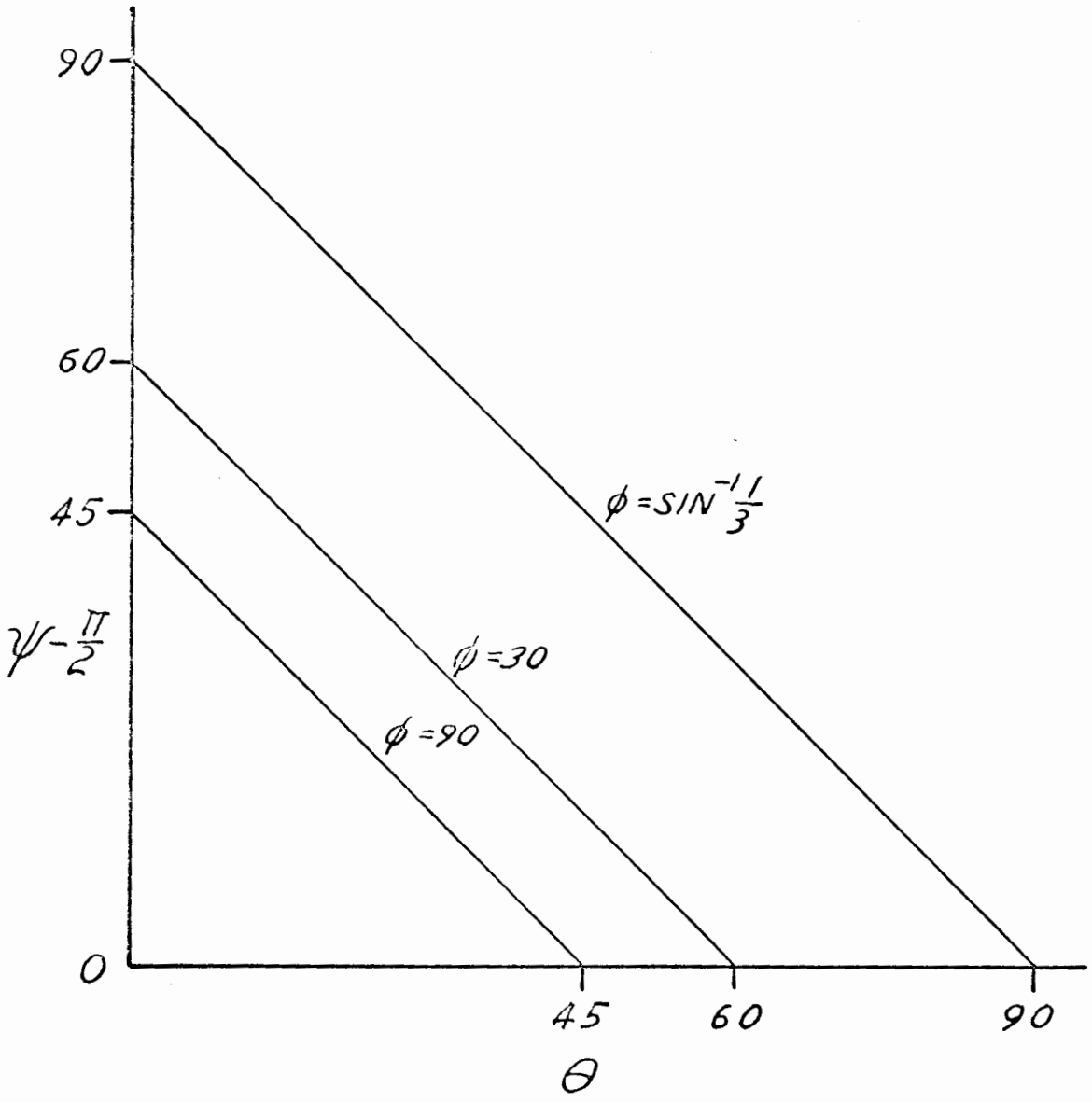

Figure 8: The Angle of the Principal Stress with a Ray Minus 90° versus the Angle of the Ray ($\psi - \frac{1}{2}\pi$ vs θ)

are used because both experimental evidence (Rose and Tanaka; also this report, page 57) and theoretical evidence (Savage) show no significant variation of flow rate or flow-field with heads greater than two container radii. This leads to the conclusion that the parameter s_o is not significant in determining flow rates in axial symmetry.

From Figure 8 and the limiting substitution used to derive equations (66) and (67) several specific examples of the relations between ϕ, ψ_o, ψ and θ' are given: for $\phi = 90^\circ$, $\psi_o = 135^\circ$ (from equation (66)), $\psi = 90^\circ$ or 180° (from equation (67)), therefore for these values of ψ and ϕ, there is only one solution for θ' and that is 45°; correspondingly, for $\phi = 30^\circ$, $\psi_o = 150^\circ$, $\psi = 120^\circ$ or 150°, and $\theta' = 0$ or 30°; and for $\phi = \sin^{-1}1/3 = 20^\circ$, $\psi_o = 180^\circ$, $\psi = 125^\circ$ or 145°, and $\theta' = 35^\circ$ or 55°. The following analysis generalizes these examples:

$$\psi_o = \pi - \tfrac{1}{2}\cos^{-1}\left[(1 - \sin\phi)/2\sin\phi\right], \text{ (from equation (66))}$$

$$\psi = \psi_o - \theta' = 3\pi/4 \pm \tfrac{1}{2}\phi, \text{ (from the limiting substitution and equation (68)), or}$$

$$\theta' = \tfrac{1}{4}\pi \pm \tfrac{1}{2}\phi - \tfrac{1}{2}\cos^{-1}\left[(1 - \sin\phi)/2\sin\phi\right]. \qquad (69)$$

An equation now exists which gives the semi-vertical angle of the radial stress field and is dependent only on the angle of friction of the flowing material. The equation rests on the assumption that flow occurs within the material and is radial.

Another relationship between θ' and ϕ can be derived from basic strain theory and examination of the yield surface. From equation (6), it is recalled that ϕ' is the angle the normal to the yield surface makes with the minor stress axis; also that because of the configuration of the yield surface, the normal always lies in a principal plane or one parallel. Since the normal represents the strain direction, it will lie in the radial di-

rection if $\psi - \phi' = \frac{1}{2}\pi$. It is possible to locate $\psi - \frac{1}{2}\pi$ on figure 8,

$$\psi - \phi' = \tfrac{1}{2}\pi,$$

$$\psi - \tfrac{1}{2}\pi = \tan^{-1}\left[(1 - \sin\phi)/(1 + \sin\phi)\right]. \qquad (70)$$

θ' is found in a manner similar to equation (69), so that

$$\theta' = (\psi_o - \tfrac{1}{2}\pi) - (\psi - \tfrac{1}{2}\pi), \text{ or}$$

$$\theta' = \tfrac{1}{2}\pi - \tfrac{1}{2}\cos^{-1}\left[(1 - \sin\phi)/2\sin\phi\right] - \tan^{-1}\left[(1 - \sin\phi)/(1 + \sin\phi)\right]. \qquad (71)$$

Flow Rates

From the last section it can be seen that logically there is no unique solution for the flow-field; likewise a particular solution for flow rate is not forthcoming. However, several equations for mass flow rate can be devised from the theory already presented. These will subsequently be compared with experimental evidence in order to judge their usefulness.

The combination of equation (63) with either equation (69) or (71) results in a new equation that is dimensionally correct for the solution of flow rates. The flow rate is

$$Q = (1/6)\gamma\pi\left[g(D - 2d)^5\right]^{\frac{1}{2}}\left[(1 - \cos^{1.5}\theta')/\sin^{2.5}\theta'\right], \qquad (72)$$

where θ' is defined in equation (69) or (71).

Equation (72) is based upon a theory of minimum energy and maximum velocity along each and every flow-tube, and therefore gives values that produce a minimum bound to the actual flow rate. However, it must be remembered that because of these assumptions this theory has its drawbacks.

Another approach to the determination of flow rates is obtained by returning to an examination of the yield criterion. On the σ_1, σ_3 plane of the pyramid, the principal strains are as written in equation (21). If a radial strain field is assumed, such that its geometry is similar to the stresses in Figure 5, then expressions for velocity can be written in both

the angular and the radial direction.

$$v_r \propto k(-\sin\phi'\cos\psi + \cos\phi'\sin\psi) = k\sin(\psi - \phi'),$$

$$v_\theta \propto k(\sin\phi'\sin\psi + \cos\phi'\cos\psi) = k\cos(\psi - \phi').$$

It is apparent that a boundary to the radial field exists at a position where $v_r = 0$. This occurs when

$$\psi - \phi' = \tfrac{1}{2}\pi, \text{ or}$$

$$\psi = \tfrac{1}{2}\pi + \phi',$$

which is identical to the hypothesis used to derive equation (71) for θ' and thus substantiates the der'vation.

If the radial velocity is considered, bounds to the flow rate can be determined, not by applying the minimum energy principle to each flow-line, but by minimizing along flow-lines that are most apt to this treatment, that is the vertical and the extreme angular flow-line. From equation (59) the minimum velocity at the extreme angular flow-line is found by

$$\partial\left[(v'^2/2) + g\,r\cos\theta'\right]/\partial r = 0,$$

and at the center-line

$$\partial\left[(v_o^2/2) + gr\right]/\partial r = 0.$$

These equations are valid for flow at the outlet when $r = r_o$. An equation for the mass flow rate is devised by integrating v over the interval of the radial field

$$Q = 2\pi\gamma\int_0^{\theta'} v r_o^2 \sin\theta(N)d\theta,$$

where N is a normalizing factor which is $\sin(\psi - \phi')$ for v' and $\sin(\psi - \phi')/\sin(\psi_o - \phi')$ for v_o. By use of the substitution $v = K/r_o^2$ and from the fact that $\psi = \psi_o - \theta$, the integration is performed and two possible bounds to the mass flow rate are conceived:

$$Q_{(v_o)} = (1/3)\pi\gamma\left[g(D - 2d)^5\right]^{\frac{1}{2}}\theta'(\cos\theta')^{-1}(\sin\theta')^{-1.5}, \qquad (74)$$

$$Q_{(v')} = (1/3)\pi\gamma\left[g(D - 2d)^5\right]^{\frac{1}{2}}\theta'(\cos\theta')^{\frac{1}{2}}(\sin\theta')^{-1.5}, \qquad (75)$$

where θ' is defined as before

Piping

Axial Flow: In engineering experience, it is known that, in some instances, the flow bound is a vertical cylinder whose diameter is not much larger than the diameter of the point of efflux; this cylinder is known as a pipe, and the type of flow as piping. In order to elucidate the conditions that cause a transformation from radial flow to piping, the following analysis, after Jenike (1961, page 148), is offered. Figure 9 shows the piping situation, where D' is the outlet diameter.

Since a pipe implies only vertical flow, the cylindrical equations of equilibrium reduce to

$$d\sigma_{rr}/dr + (\bar{\sigma}_{rr} - \bar{\sigma}_{\alpha\alpha})/r = 0,$$

$$d\tau_{zr}/dr + \tau_{zr}/r = \gamma.$$

Making the substitution, $r^2 = nD^2/4$, these appear as

$$d\sigma_{rr}/dn + (\bar{\sigma}_{rr} - \bar{\sigma}_{\alpha\alpha})/2n = 0, \qquad (76)$$

$$d\tau_{zr}/dn + \tau_{zr}/2n = \gamma D/4n^{\frac{1}{2}}. \qquad (77)$$

If $d(\tau_{zr}n^{\frac{1}{2}}) = \gamma D/4$ which gives $\tau_{zr} = \frac{1}{4}D\gamma(n-1)n^{-\frac{1}{2}}$, then, in piping which supports no shear forces and where $n = 1$, there is produced a new expression for shear equilibrium

$$d\tau_{zr}/dn + \tau_{zr}/2n = \tau_{zr}/(n-1).$$

Following Jenike, a bar over a stress indicates that the stress is at the surface of the yield locus and is causing failure. These stresses are defined below, where f_c, the unconfined yield pressure, is the pressure that will cause failure at a traction-free surface. The failure stresses are

$$\bar{\tau}_{zr} = \bar{\sigma}\sin\phi\sin 2\psi,$$

$$\bar{\sigma}_{zz} = \bar{\sigma}(1 + \sin\phi\cos 2\psi) - f_c(1 - \sin\phi)/2\sin\phi,$$

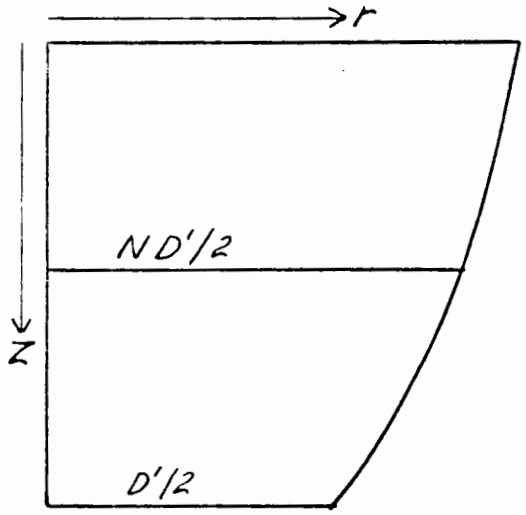

Figure 9: Dimensions in a Pipe

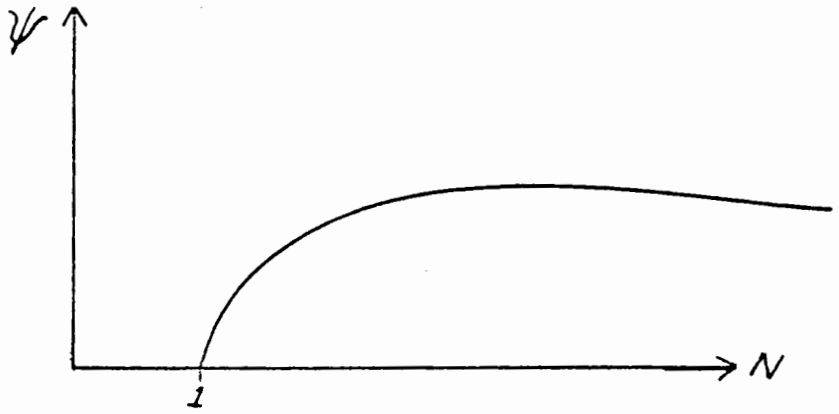

Figure 10: Unbounded Flow Field

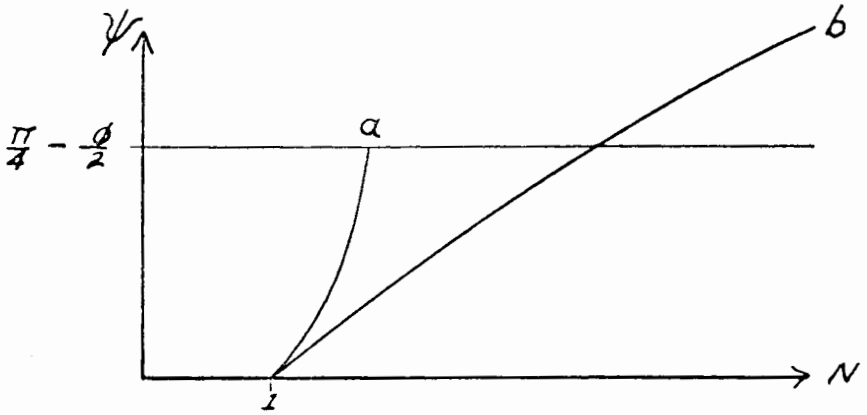

Figure 11: Bounded Flow Fields

$$\bar{\sigma}_{rr} = \bar{\sigma}(1 - \sin\phi\cos 2\psi) - f_c(1 - \sin\phi)/2\sin\phi,$$

$$\bar{\sigma}_{\alpha\alpha} = \bar{\sigma}(1 + \sin\phi\cos 2\psi) - f_c(1 - \sin\phi)/2\sin\phi;$$

the principal stresses are

$$\sigma_1 = \bar{\sigma}(1 + \sin\phi) - f_c(1 - \sin\phi)/2\sin\phi,$$

$$\sigma_3 = \bar{\sigma}(1 - \sin\phi) - f_c(1 - \sin\phi)/2\sin\phi,$$

$$\sigma_\alpha = \bar{\sigma}(1 + \sin\phi) - f_c(1 - \sin\phi)/2\sin\phi;$$

and the mean failure stress is

$$\bar{\sigma} = (\sigma_1 + \sigma_3)/2 + f_c(1 - \sin\phi)/2\sin\phi.$$

Substituting these relationships into equations (75) and (76) and eliminating $d\bar{\sigma}/\bar{\sigma}$ from the resulting equations there is produced a new equation,

$$d\psi/dn = \left[\tfrac{1}{2}\sin 2\psi/(\cos 2\psi - \sin\phi)\right]\left[\left((1 - \sin\phi\cos 2\psi)/(n - 1)\right) - \left((1 + \sin\phi)/2n\right)\right], \tag{78}$$

for the variation of stress direction.

In order to determine the conditions necessary for piping, it is desired to have solutions of equation (78) near $n = 1$, and $\psi = 0$. Examining this equation, it is seen that as ψ increases, so does n for the condition $(d\psi/dn)_{\psi=0} > 0$, and thus there will be a change of behavior, either at

$\cos 2\psi = \sin\phi$, with $d\psi/dn \to \infty$, or at

$2n(1 - \sin\phi\cos 2\psi) = (n - 1)(1 + \sin\phi)$, with $d\psi/dn = 0$.

For $\psi \to 0$, $n \neq 1$, and $d\psi/dn \to 0$, the second possibility gives a graph such as in Figure 10. The first possibility gives a graph such as in Figure 11. In general, there will be a discontinuity in solutions that have one critical solution when both possibilities occur simultaneously so that $d\psi/dn$ does not change sign. This gives

$2n(1 - \sin\phi) = n - 1$, or

$(n + 1)/2n = \sin\phi$.

For the possible ranges of n, $\infty \geq n \geq 1$, there exist a range of solutions to

this phenomenon of $30^\circ \leq \phi \leq 90^\circ$. Thus for $\phi > 30^\circ$ there are finite solutions for n, and a pipe is defined. For $\phi < 30^\circ$ there is a smooth transition from those solutions for which n increases to those where ψ reaches the limiting value of $\frac{1}{4}\pi - \frac{1}{2}\phi$. That is there is a transition to continuously expanding values of n and radial fields develop.

On the other hand, provided that the term in brackets in equation (78) has a zero, there are solutions such as in Figure 10, but this requires

$$2n(1 - \sin\phi\cos 2\psi) = (n - 1)(1 + \sin\phi), \text{ or}$$

$$\sin\phi = (n + 1)/[(n - 1) + 2n\cos 2\psi].$$

Thus, as n varies from one to infinity, $\sin\phi$ varies from $1/\cos 2\psi$ to $1/(1 + 2\cos 2\psi)$, which means that $\sin\phi$ must always be greater than 1/3.

For $\sin\phi < 1/3$, all solutions are as line a in Figure 11. It is seen from Thurston and Deresiewicz' analysis of the ratio of shearing forces to normal forces (Scott, page 301) that $\tan\phi = (\sqrt{3} + 4\sqrt{2}\, f)/2(\sqrt{6} - f)$, where f is the coefficient of friction, which for $f \to 0$, gives $\tan\phi \to 1/2\sqrt{2}$ or $\sin\phi \to 1/3$. Thus solutions as in line a are impossible.

Therefore, there is no solution for flow where $\phi < 19^\circ 28'$, but in the range $19^\circ 28' < \phi < 30^\circ$ there is a smooth transition from expanding flow to piping, dependent upon the ratio of orifice to particle size. However, for $\phi > 30^\circ$ there is an abrupt transition and piping must occur.

Rectangular Symmetry: The bounds of the radial field are now known for the axial case; the same analysis, therefore, is applied to the case of rectangular symmetry. The equations of equilibrium are simplified, because of the reduction of the pertinent dimensions from three to two, to

$$d\tau_{xz}/dx = \gamma, \text{ and } d\sigma_{xx}/dx = 0.$$

The ratio of pipe width to orifice width, x/D, is equal to q. Then, by

integration and substitution, $\tau_{xz} = \gamma_D(q - 1)$, and

$$[d\bar{\sigma}/\bar{\sigma}] + 2\sin 2\psi \sin\phi \, d\psi/(1 - \sin\phi\cos 2\psi) = 0,$$

$$[d\bar{\sigma}/\bar{\sigma}] + 2\cot 2\psi \, d\psi = dq/(q - 1).$$

Combining, and eliminating $d\bar{\sigma}/\bar{\sigma}$, this yields

$$d\psi/dq = [\sin 2\psi/2(\cos 2\psi - \sin\phi)][(1 - \sin\phi\cos 2\psi)/(q - 1)]. \quad (79)$$

There are no real, that is to say, natural, situations which would lead to a zero in the numerator of this equation; therefore there are no smooth transitions, and all solutions in rectangular symmetry are pipes.

EXPERIMENT OR VERIFICATION OF THEORETICAL RELATIONSHIPS

Establishment of Physical Parameters

Particle Size: All material used in the experiments were in the sand range of soils, that is from 0.06 to 2.00 mm in diameter. The size of some synthetic materials (Ballotini, Silicon Carbide, and Aloxite) was determined from manufacturers' statements; the size range of the natural materials (sand) and one manufactured material (lead shot) was determined by sieving. This was done by hand and through British Standard Sieves. Table 1 gives the size range of the sands; Table 2 does the same for the other materials.

TABLE 1

SAND PARTICLE SIZE

Screen	Mesh Size, microns	Hatford Loam, % retained	Leighton-Buzzard, % retained
14	1204	0	0
25	599	0	98
52	295	67	2
100	152	29	-
200	76	3	-
-200		1	-
		100	100

TABLE 2

PARTICLE SIZES

Material	Average Size, mm
Ballotini No. 4	1.00 - 1.20
7	0.52 - 0.60
10	0.25 - 0.30
13	0.12
18	0.06
Lead Shot	0.85 - 1.00
Silicon Carbide No. 120	0.124
220	0.071
320	0.047
Aloxite No. 16	1.00
30	0.50
60	0.25

Density: The density of all unknown material was found by standard test (Akroyd) and is reported in Table 3. The densities are particle densities and are represented by the symbol ρ. Throughout this report, all bulk densities are represented by γ. The exact value of the bulk density is dependent upon the voids ratio; γ reported here was achieved by light vibration of the measuring container.

TABLE 3

SPECIFIC GRAVITY OF VARIOUS GRANULAR SOLIDS

Material	ρ	γ
Hatford-Loam Sand	2.47	1.55
Leighton-Buzzard Sand	2.63	1.53
Ballotini No. 4	2.97	1.74
7	2.95	1.79
10	2.96	1.78
13	2.94	1.78
18	2.77	1.73
Lead Shot	11.00*	6.74
Silicon Carbide	3.22*	
Aloxite	3.97*	

*Taken from Handbook of Chemistry and Physics

Angle of Friction: Inasmuch as the experimental evidence showed that the most important parameter was the angle of internal friction, ϕ, close attention was paid to determining this angle. At first, a Clockhouse Type K11 shear-box tester was used for this determination, and a value of $\phi = 38^{\circ}$ was obtained for Hatford-Loam Sand. Trouble with repeatability and the obvious disadvantage of measuring shear across only one plane led to the selection of a Clockhouse tri-axial tester instead of the shear-box for measuring ϕ; the tests were run with the material dry. The results obtained, which had a minimum of scatter, are tabulated below.

All tests were made with four pressures, 10, 20, 30, and 40 pounds per

inch squared, and the envelope was drawn as a straight line that most approximated the tangents to the four Mohr's circles.

TABLE 4

ANGLE OF INTERNAL FRICTION

Material	ø
Hatford-Loam Sand	30½
Leighton-Buzzard Sand	29½
Ballotini No. 4	18
7	18
10	19½
13	23½
18	24
Silicon Carbide No. 120	33

It would seem, from the Ballotini, that the smaller the particle of the same material, the higher the angle of friction.

Flow Rate as a Function of Orifice Diameter

The first flow parameter established was the relation between orifice and particle diameters for a container sufficiently large. The container used was an inverted pycnometer bottle (actually an household Kilner jar) with a hole drilled in the bottom (the top when inverted) to insure that flow was not inhibited by vacuum within the emptying jar. The procedure used to obtain the flow rate was to close the nozzle orifice with a simple bung, which was removed after the bottle was inverted and supported on a ring-stand; to time the flow, from the moment the bung was removed until the bottle was empty, with a stopwatch; and then to obtain the total weight of material that had run out. In the first instance, the flow rate was noted as seconds per kilogram; the results were later inverted and multiplied by 1000 to place them in the proper form of grams per second.

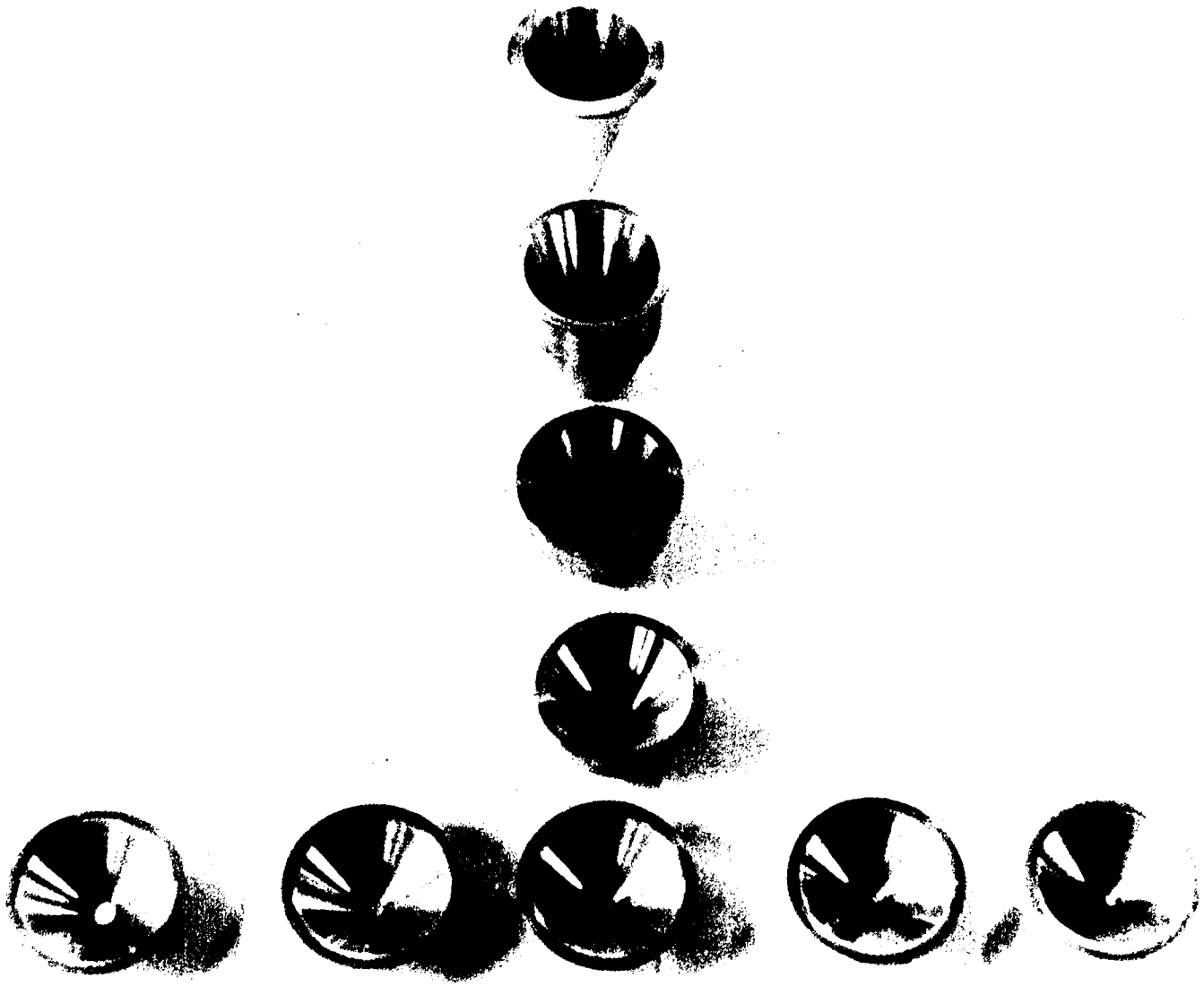

Figure 12: The Nozzles: From left to right, Decreasing Orifice Diameter; from top to bottom, Increasing Cone Angle

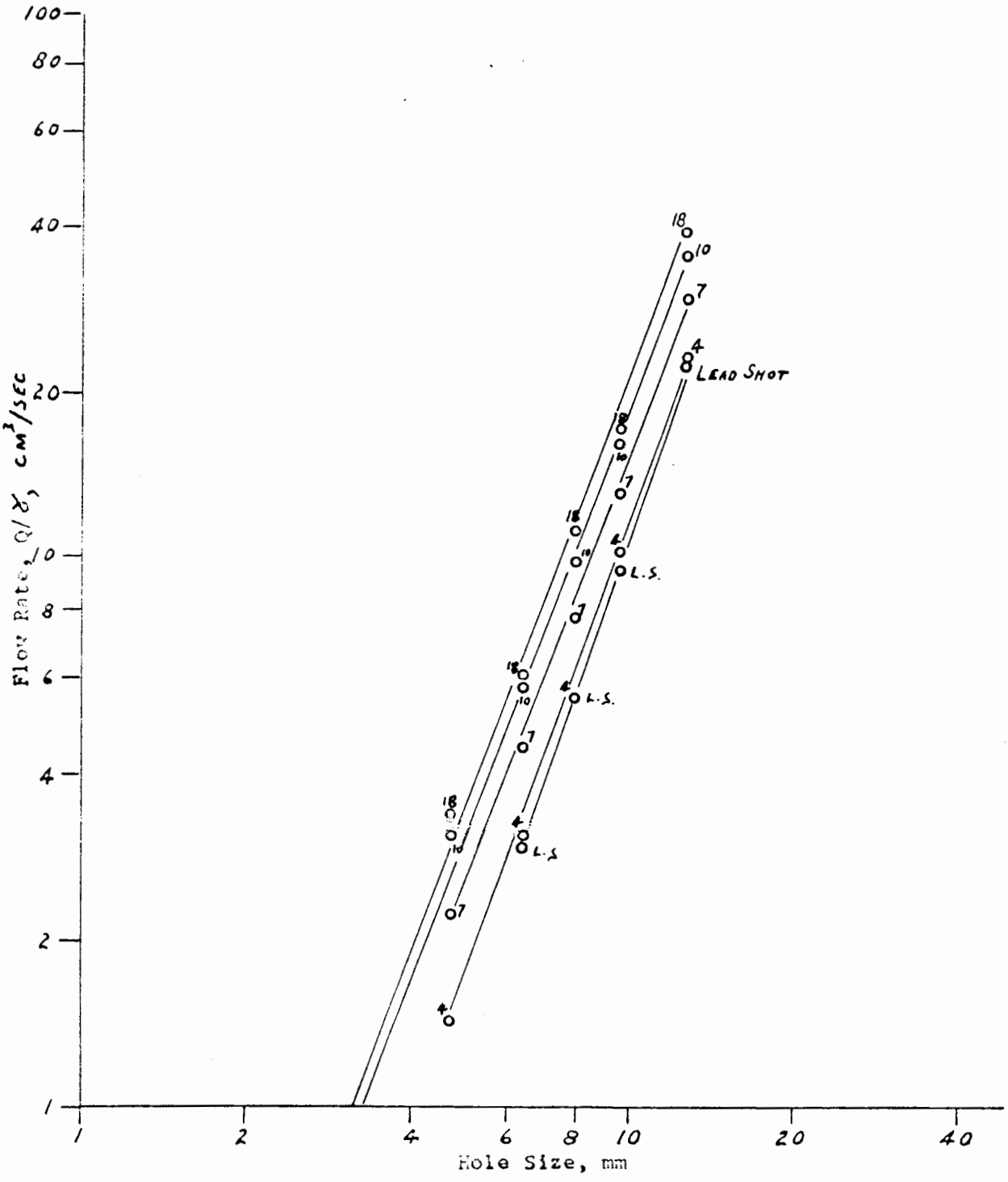

Figure 13: Orifice Diameter versus Flow Rate

Because the exponent of D was not exactly 2.5, a graph of $Q^{0.4}$ versus D was examined. Since it did not extrapolate to the origin showing that there was some blockage of the outlet, the flow rates were fitted to the parameter

$$Q \propto D'^{2.5} = (D - nd)^{2.5} \qquad (81)$$

and a value of n = 1.94 was obtained. Accordingly, the value of n was taken as 2.0 and it was assumed there is an annulus, one particle thick, of slow-moving material between the flow and the outlet surface.

A second logarithmic graph, Figure 14, of particle size versus flow rate with constant hole size gives a series of lines that do not lend themselves to any ready relationship. One conclusion that is seen however, is a minimum ratio between D and d for smooth flow of spherical particles. From (81) the hole diameter must be at least two particle diameters, however, from data of flow through the 1/8-inch (3.175 mm) hole, D'/d must be greater than 4. Further, it can be seen that the larger sizes are curving off to an asymptote that represents zero flow; this, of course, is when d is approximately D'/4. As the particles become smaller, flow increases to a steady value; however, when the particle size is diminished beyond a certain point, cohesion from surface phenomena, becomes a recognizable factor and ultimately causes arching and flow ceases. This is demonstrated with the finer grades of Silicon Carbide. As D/d becomes increasingly large so that $(D - 2d) \rightarrow D$, small variations of d will cause no difference to the flow rate.

θ' Variation

In the same manner as the diameter variation, flow rates were obtained for varying cone angle. The semi-vertical angles of the nozzles were 90° (flat plate), 50°, 40°, 30°, 20°, and 15°; the orifice diameters were kept constant at 5/16 inch. The base dimension of the nozzles was 2.75 inches.

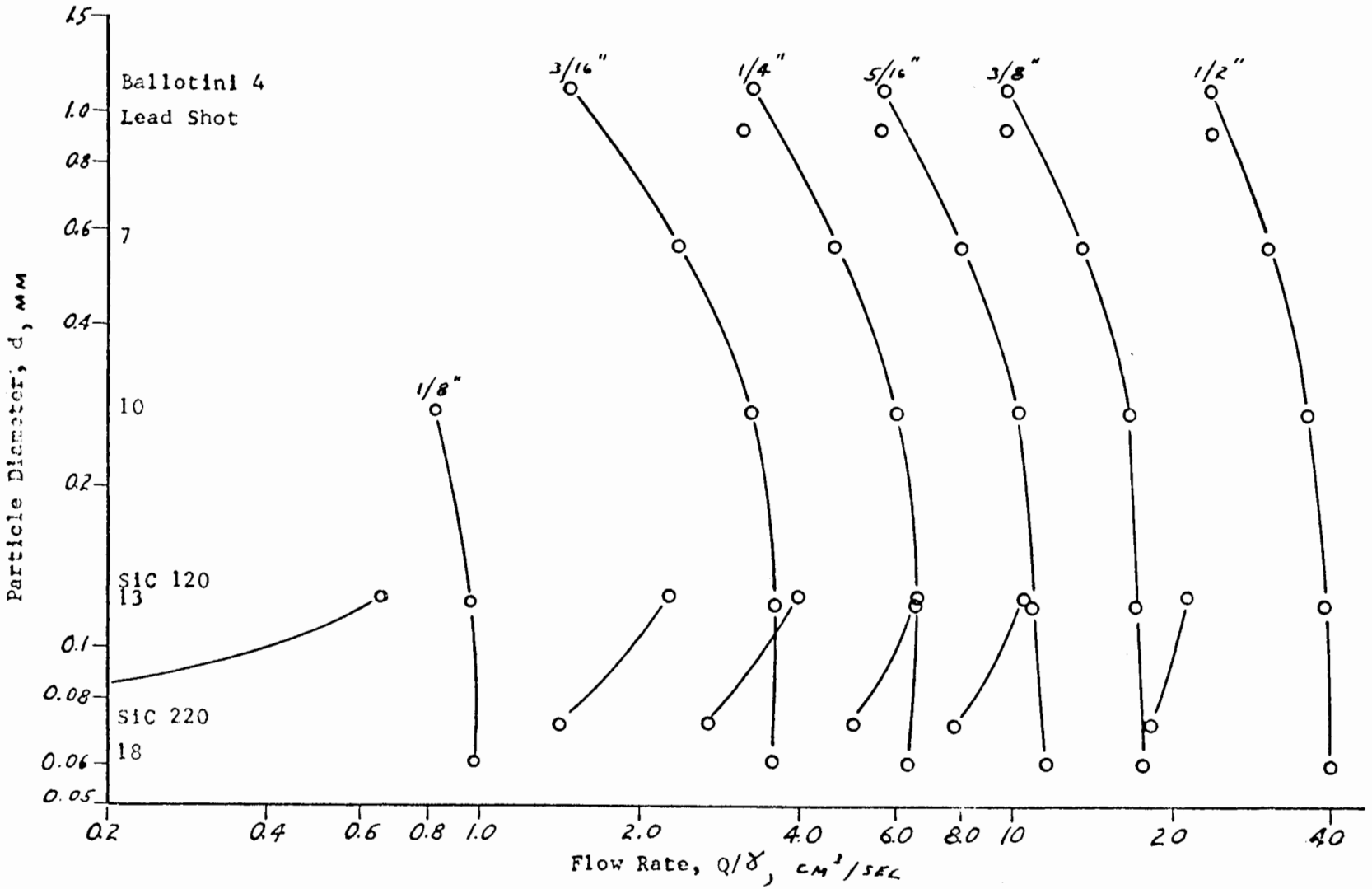

Figure 14: Particle Diameter versus Flow Rate for Varying Hole Size

The results of this variation are placed in Table 6.

This information is plotted, Figure 15, as flow rate versus cone angle for constant particle size. It is assumed that the finer grades of Hatford-Loam have a higher angle of friction, ϕ, than normal, and that the tests on the -100 fraction represent a pipe.

TABLE 6

FLOW, gm/sec, WITH VARYING CONE ANGLE

Material	Semi-Vertical Angle, θ'					
	90°	50°	40°	30°	20°	15°
Ballotini No. 18	18.2	19.2	20.0	18.9	19.2	20.4
13	18.5	18.5	20.4	21.3	24.4	23.3
10	16.9	17.5	19.6	21.3	24.4	25.0
7	12.8	13.7	16.1	17.9	21.2	21.9
4	9.2	9.5	12.0	13.9	17.2	17.2
Leighton-Buzzard	9.2	9.4	10.8	11.8	14.7	15.5
Lead Shot	35.2	36.7	43.9	48.8	61.5	65.5
Hatford-Loam +52	12.3	12.5	13.4	13.4	15.2	15.6
-100	11.0	10.0	10.2	9.0	9.0	8.0

Plane Flow

Some tests, both qualitative and quantitative, were run to observe the flow in rectangular symmetry. The motivation was partly that a check on the statement that all solutions to a radial field in rectangular geometry result in pipes was desired.

A perspex box, with inside dimensions, 1 inch by 4 5/16 inches by 20 inches, and with a bottom plate that has a central slit of dimensions, 1 inch by 5/16 inches was constructed. For the quantitative study, the slit was changed, by means of a sliding insert plate, to either of two smaller dimensions, ¼-inch or 3/16-inch. The smaller widths were used to keep the flow rate within bounds that were reasonable for stop-watch timing.

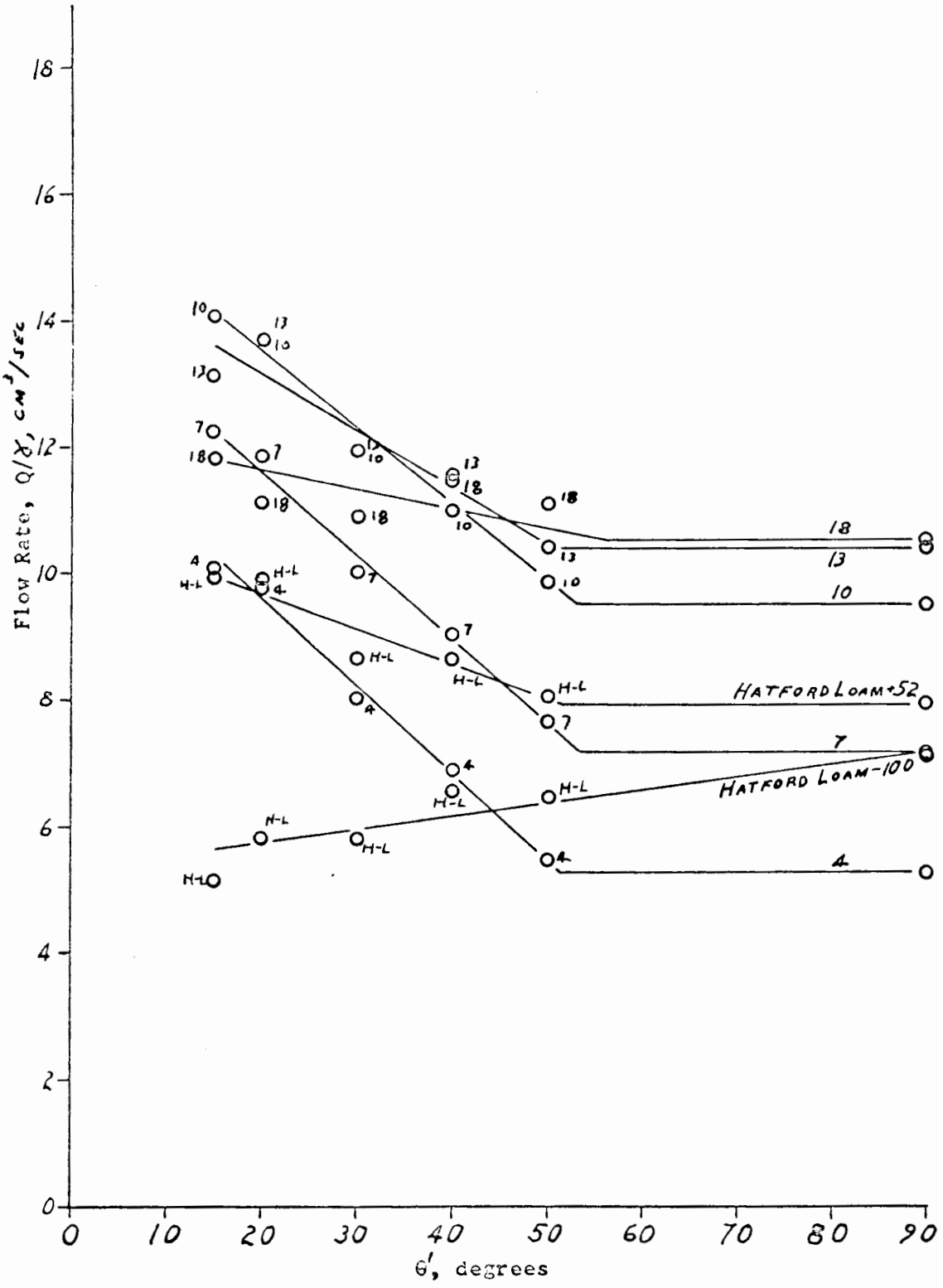

Figure 15: Flow Rate versus Cone Angle, θ'

The box, Figure 18, also has provision for changing the wall angle; this is done by inserting triangular prisms, of the desired shape, on either side of the slit.

The results in Table 7 are given in graphic form in Figures 16 and 17. Figure 16 relates flow rate to semi-vertical angle for the ¼-inch slit; Figure 17 does the same for the 3/16-inch slit.

TABLE 7

FLOW RATES, gm/sec, IN PLANE GEOMETRY

Material	Semi-Vertical Angle 90°	50°	40°	30°	20°	10°
	Slit Area = 0.250 in^2					
Ballotini No. 18	69.2	77.4	73.0	75.2	82.5	77.2
13	70.3	82.5	81.3	83.7	87.9	87.3
10	66.7	79.1	77.0	80.1	82.7	84.8
7	53.8	63.4	63.8	65.7	67.1	69.0
4	39.7	44.8	46.2	48.7	50.2	49.9
Leighton-Buzzard	38.9	42.0	42.3	45.6	46.2	40.4
Lead Shot	147.1	164.4	172.5	175.4	179.9	178.1
Watford-Loam	49.6	54.1	54.2	58.1	58.2	55.1
	Slit Area = 0.1875 in^2					
Ballotini No. 18	43.4	47.1	47.8	50.4	55.0	55.6
13	45.7	48.6	50.8	51.9	55.1	57.3
10	41.3	45.5	48.1	49.7	51.0	54.7
7	31.8	35.5	36.4	36.8	38.7	41.7
4	22.0	24.8	25.6	26.2	27.3	30.8
Leighton-Buzzard	22.2	23.2	23.7	24.0	27.0	23.1
Lead Shot	82.4	99.1	101.8	97.4	103.6	97.5
Watford-Loam	30.3	33.2	32.9	33.9	35.1	34.0

Unlike the curves in the graph of the same relationship in conic flow, the curves in Figures 16 and 17 have rather shallow and unchanging slopes. It is presumed that because of the vertical nature of the flow, the introduction of sloped walls had little effect on the flow rate. This presumption is borne out by photographic evidence collected during these test runs. Figure 18, with Aluminum Oxide granules of number 16 grit and with Leighton-

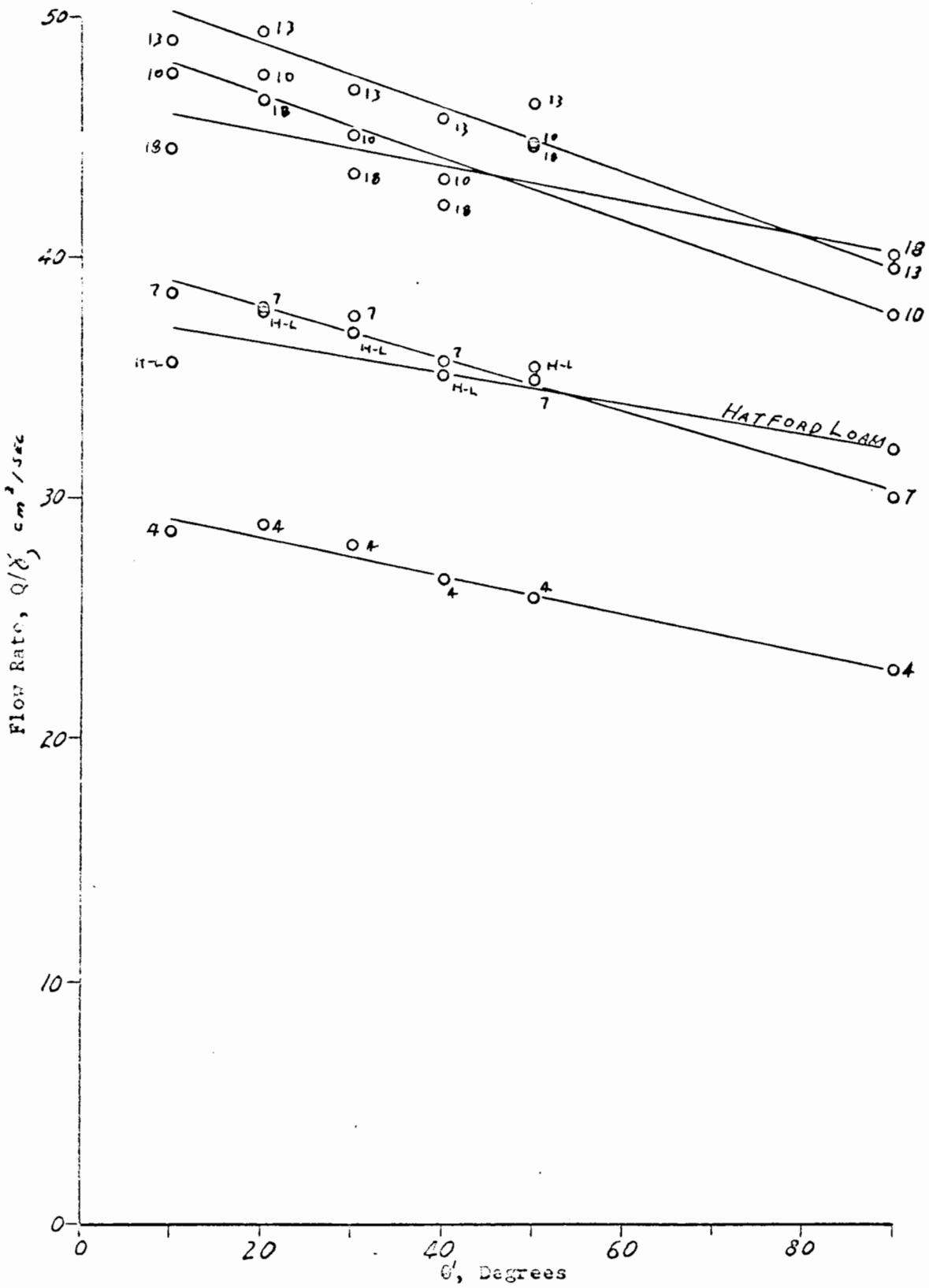

Figure 16: Flow Rate versus Wall Angle, θ', for Rectangular Geometry, ¼-inch Slit

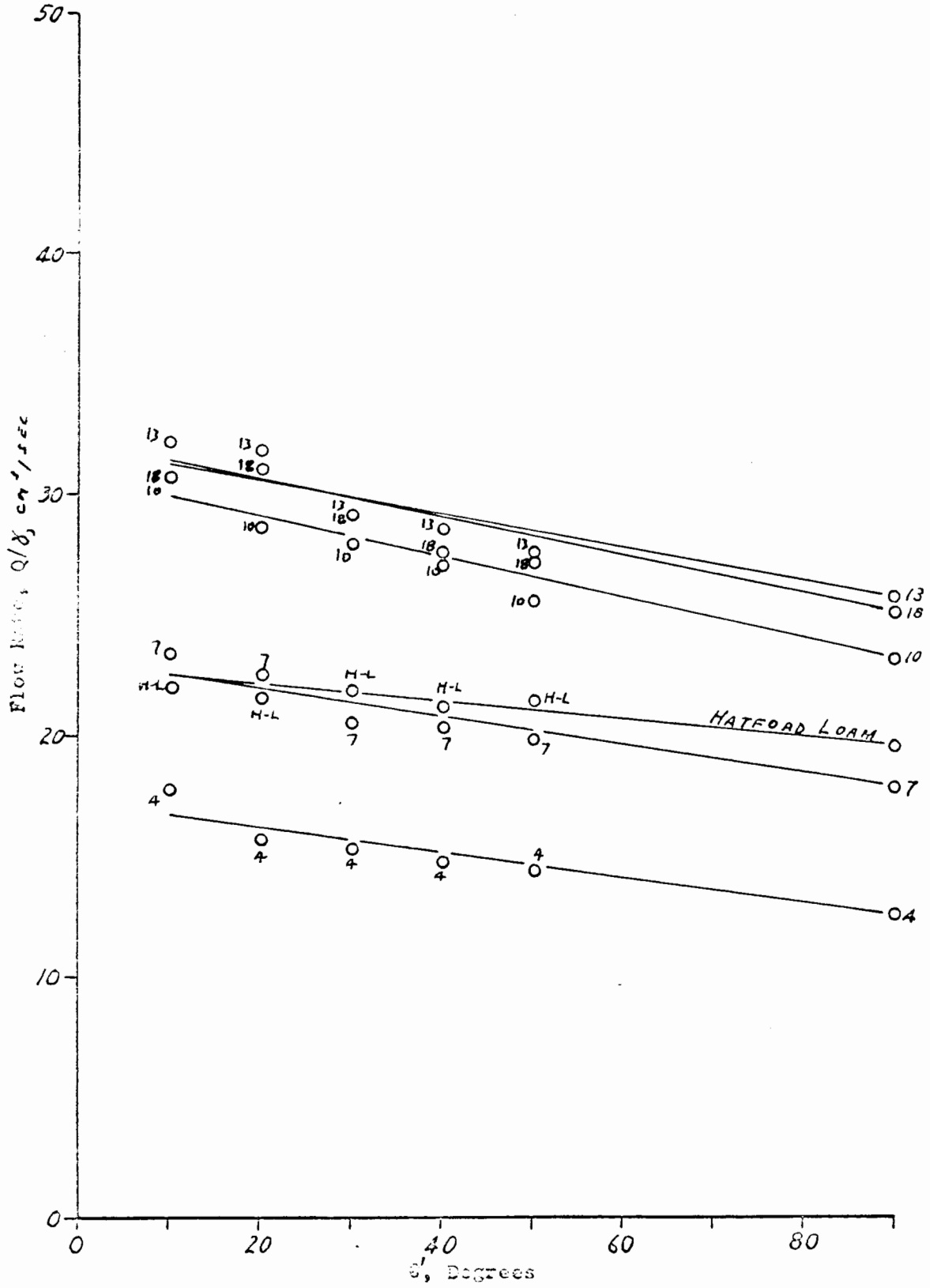

Figure 17: Flow Rate versus Wall Angle, θ', 3/16-inch Slit

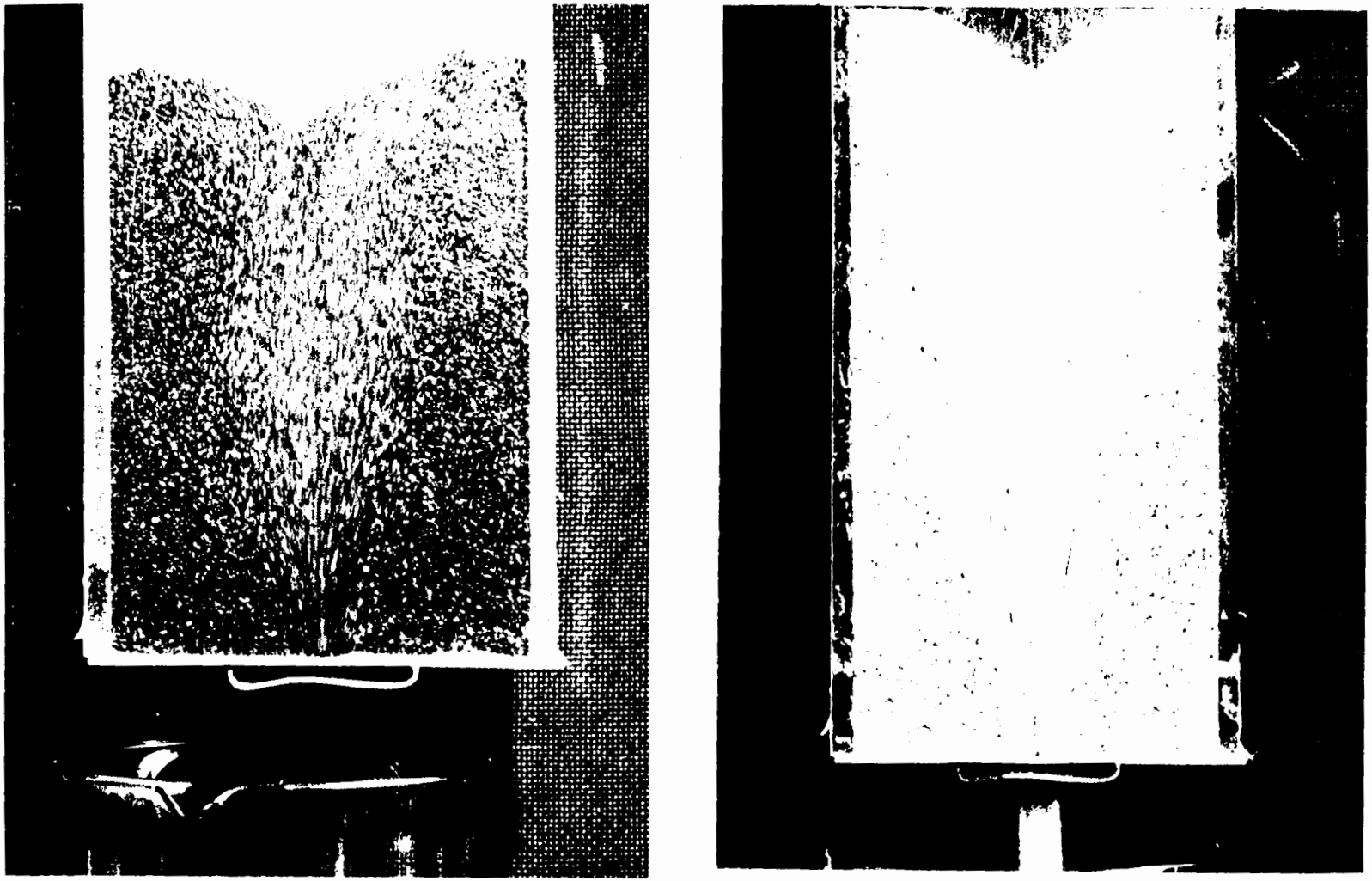

Figure 18: Piping in Rectangular Geometry: (a) Aloxite, (b) Leighton-Buzzard Sand

Dubbard sand, clearly shows a near-vertical flow pattern.

Non-Influential Parameters

General: It has been stated by other workers (pages 2 and 3) that changing some parameters has little or no effect on the failure in granular material, and thus on the flow rate. To be consistent, however, checks on these parameters were made using the materials and equipment described in this report.

Compaction: Flow was compared when the material was loosely heaped in the jar with when it was compacted by placing the jar on a G. R. C. Sherwen Vibration Table. The flow rate did not vary. It is assumed that the material reaches a condition of dilatancy at failure that depends only on its physical characteristics and not upon its original state of packing.

Head Relations: It has been shown by Savage that flow is independent of head. This statement was checked for several different cones and for several materials, and in plane flow, not only by varying the initial head and comparing flow rates, but by timing increments of flow as the bottle emptied, and by greatly increasing the head with lead shot as a surcharge. In all instances, the flow rate remained the same whether there was but a few grains or a kilogram of material above the orifice. This head independence, along with the quantities of material used (usually one kilogram), is justification for timing the flow from removal of bung to emptying of jar rather than the more complicated procedure of stopping the flow before it naturally ceases

Density: The independence of head suggests that the flow is also independent of density variations. The rates of flow for lead shot and equivalent sized Ballotini, when reduced by their respective densities, are equal.

For this reason, the observed mass flow rates are reduced to unit density when plotted.

Wall Roughness: Lining the container or the nozzle or both with sandpaper had no effect upon the flow rate. Presumably, the material fails along many radial sliplines, and the alteration of one line by changing the wall characteristics causes little or no change to the overall flow pattern.

This conclusion is further reason for not using Jenike's s_o in the calculations of radial bounds because s_o is derived from wall conditions.

Radial Bound

Without a doubt, the most important evidence required is proof of radial flow and measurement of its bounds. From initial studies, where a layer of colored beads was placed at various heights over the orifice within the contained material and the resultant pattern observed in the catch-beaker, an assumption of radial flow was made.

The first attempts at measuring the radial bound were done in a perspex tube, Figure 19, of 1 5/8-inch diameter, and 36-inch length which was attached to a plate with a 5/16-inch hole in the center. Observations were made of the bound between moving and stationary material, at the wall, during flow, and of the height of material remaining after flow had ceased. Figure 20 shows the geometry of these measurements. The results are displayed in Table 8.

Where a spread of figures are reported the lower figure indicates a reading just after the commencement of flow, and the higher figure indicates a reading near the end of flow. Although head independence of flow rate has been shown, a check on these readings was made by maintaining constant-head in one instance. There was no observable difference in θ'.

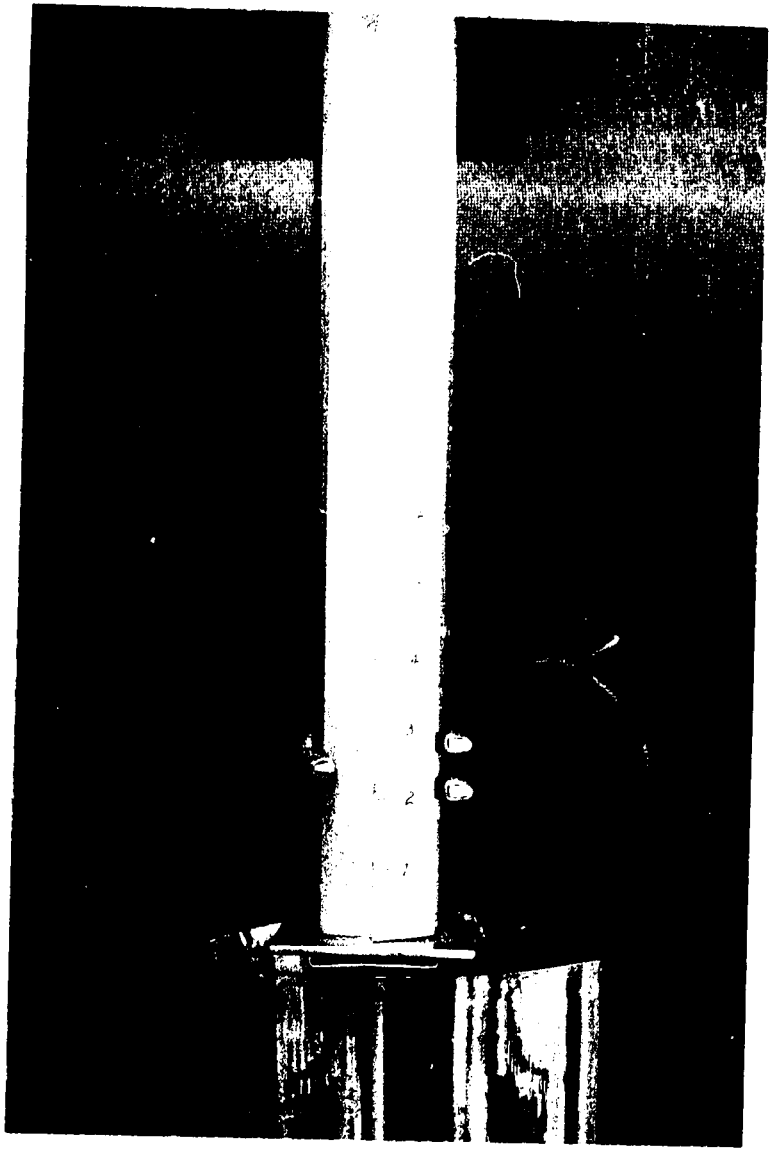

Figure 19: The Perspex Tube

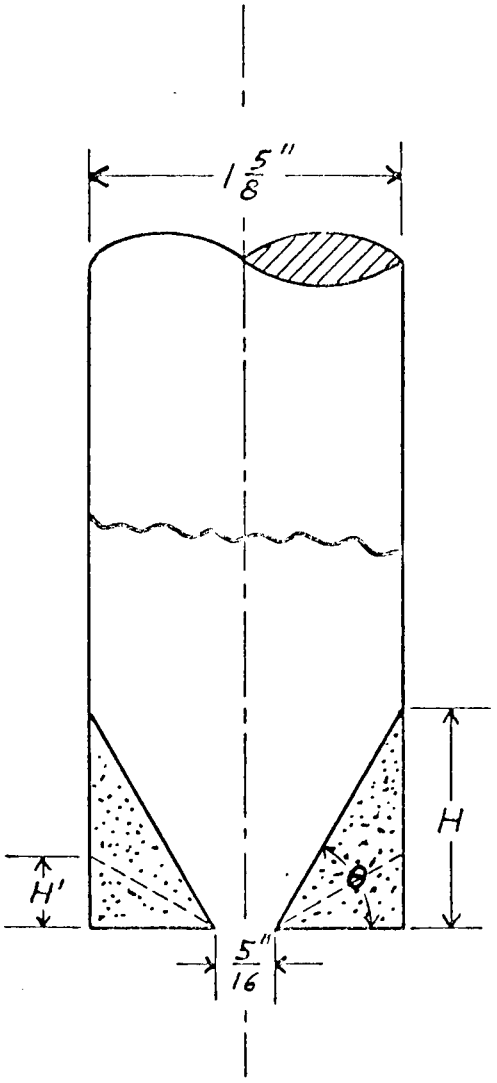

Figure 20: Dimensions of the Perspex Tube

TABLE 8

THE RADIAL BOUND, θ'

Material	Triaxial ϕ, degrees	θ', degrees	Angle of Repose
Ballotini No. 4	18	62 - 69	25
+ 3kg Lead Shot	-	53 - 69	-
7	18	59 - 65	26
10	19½	56 - 62	28
13	23½	52 - 56	28
18	24	50	28
Lead Shot	-	65	30
Hatford-Loam Sand	30½	38	38
+ 3kg Lead	-	26 - 38	-
Leighton-Buzzard Sand	29½	31 - 41	40
+ 3kg Lead	-	41	-
Hatford-Loam, +52 -25	-	38 - 39	40
+100 -52	-	27 - 33	37
+200 -100	-	19	37
SiC No. 120	33	0 - 10	47
SiC No. 120 painted Gray	33	0 - 10	47
Aloxite No. 60	-	0 - 22	40

Because the perspex tube method is open to the criticism that it does not show that either a radial bound exists, or that, if it does, it extends to the wall, another method was used. This was the wax-cast method adapted from equipment designed by Martin and Richards (1965).

The bottom of a Kilner jar was cut off and the cap was fitted with a disc that had a central 5/16-inch hole and a piece of metal loosely riveted so that it could be moved to cover the hole. A 2½-inch diameter by 8-inch long copper tube fitted neatly into this jar and served as the actual mold. The tube was filled to a sufficient height with dyed material and then with undyed material; the hole was uncovered until the undyed material flowed from the hole and then recovered; the base (actually the Kilner-jar cap) was tightly sealed with aluminum foil; and then paraffin wax was melted into the material left in the tube. The entire apparatus was heated in a warming oven to insure removal of all air bubbles in the cast. After the wax had

entirely melted, the tube and its contents were cooled to room temperature; then the tube was gently warmed with a gas flame and the cast extracted. The cast could then be easily split with an old hacksaw blade.

The first conclusion to be drawn from Martin and Richards' article, and from the present evidence, is that the bound is accurately radial and does extend to the walls. However, the values of θ' were found to be smaller in the wax-cast method than in the perspex tube. It was then decided to run as much material through the mold as had been run through the perspex tube (approximately one kilogram) before fixing it with wax. Two things were evident: first, this method can give results that are higher if the flow is not allowed a preliminary period of stabilization; second, with flow of larger particles, grains positioned higher up the slope of the dead-zone can be dislodged or "plucked" from the dead-zone by the moving material.

TABLE 9

RADIAL BOUND, θ', FROM WAX-CAST

Material	ϕ	Cast No.	θ', wax	θ', tube
Lead Shot Through Ballotini No. 4	-	1	-	-
Ballotini No. 4 and Lead Shot	-	2	45	-
Leighton-Buzzard	29½	3	22½, 31 to wall	31 - 41
Hatford-Loam	30½	4	*21	25 - 38
		6	*34	
Ballotini No. 4	18	5	*41	62 - 69
		7	45, 50 to wall	
Aloxite		8	*20	0 - 22
Silicon Carbide No. 120	33	9	*0	0 - 10

Thus the perspex tube gave better results in one respect because it allowed flow to be observed after it had stabilized; but worse results in another respect because it did not show when "plucking" had taken place. Figure 21 shows two wax-casts of the same material, Ballotini Number 4, one

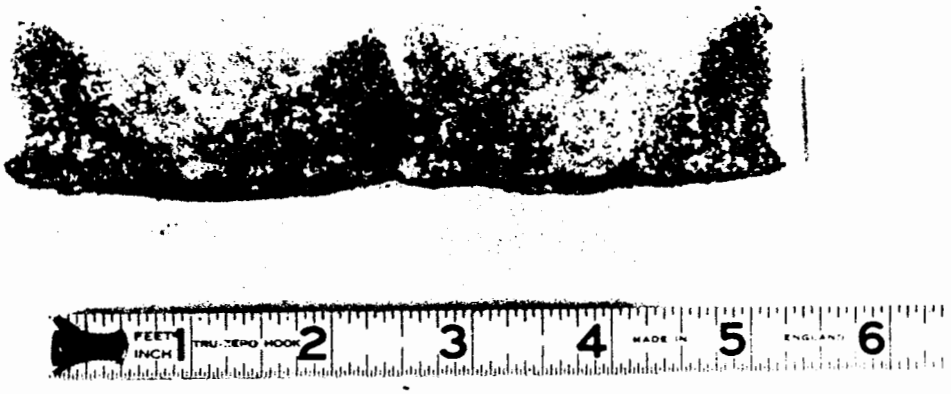

(a) The Radial Bound



(b) Plucking

Figure 21: Wax-Cast Models of Ballotini Number 4

that was fixed soon after the clear material flowed through, and one that was fixed after quite a bit of clear material had flowed. Plucking is very evident. Table 9 lists the casts made and the respective angles of radial bound. The asterisk indicates that the angular bound forms a straight line to the wall and that no "plucking" took place.

A comparison of experimentally determined θ's shows that the perspex method tube was often accurate, but that it fell down in the determination of θ' for the coarser Ballotini. The true value of θ' probably lies between those obtained by these two experimental methods.

Model 9, Silicon Carbide, pictured in Figure 22, shows a definite pipe in radial symmetry, and is substantiation of the thesis that material with ϕ greater than 30° will pipe.

Errors:

With all experimental work, the limits of precision must be stated. In this section it is recognized that the results presented are limited, sometimes severely, by a lack of precision. It is felt, however, that a substantial increase in precision and understanding is obtained over older work.

The majority of the errors are variable , or compensating. Care was taken to not introduce systematic errors by careful control of such things as orifice diameters and cone angles. With careful machining, these two parameters were kept within a few tenths of one percent of their stated value. Flow rates were stop-watch timed with a watch that had a minimum scale division of 0.2 seconds. Therefore, in reporting experimental flow rates, the ~~use of~~ three figures ~~insures that~~ given all are significant.

Reported particle diameters represent an average, thus the graph of

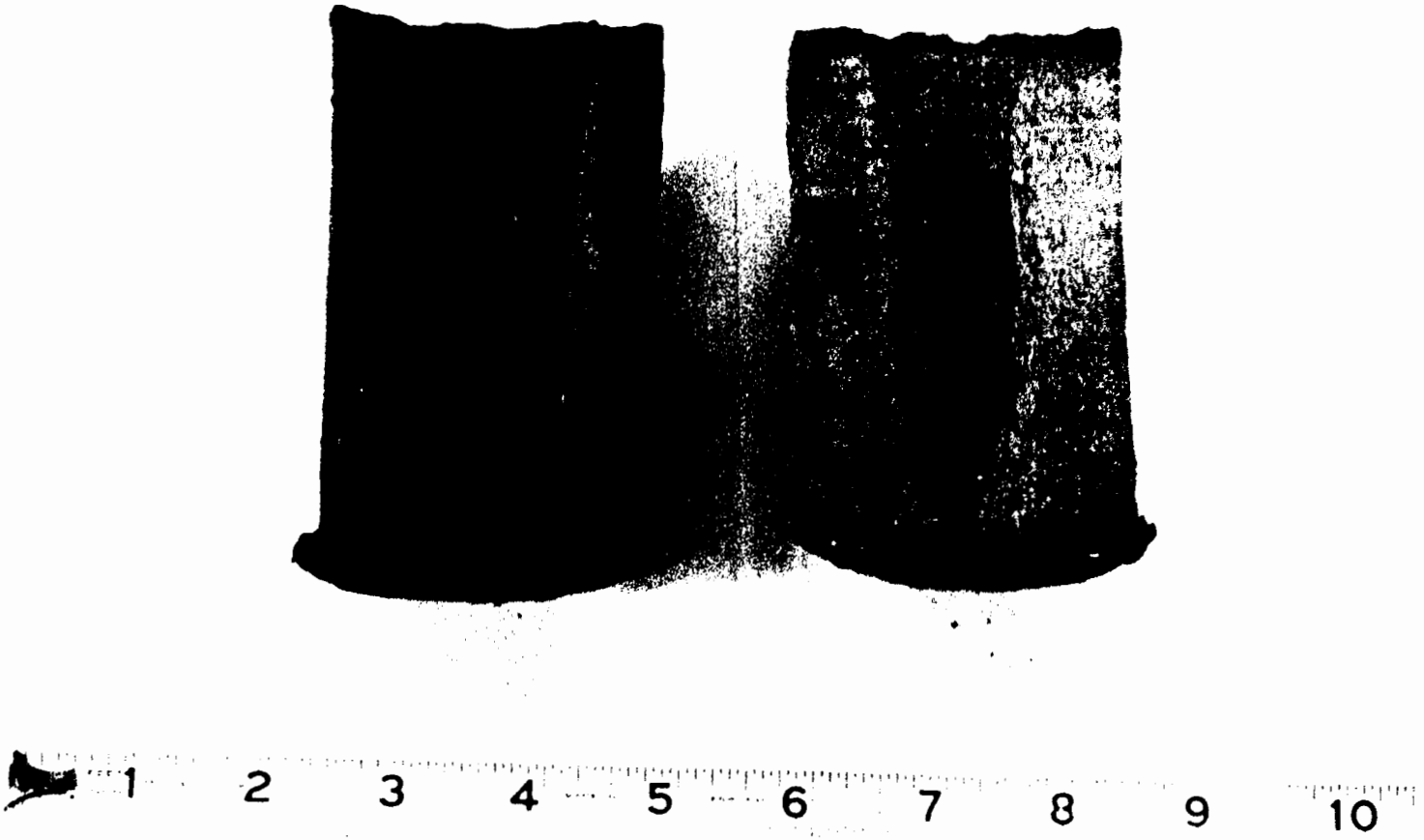

Figure 22: Wax-Cast Model of Silicon Carbide Showing Piping

particle diameter versus flow rate is accepted more for its qualitative than its strictly quantitative value. Differences in d will cause small errors to be introduced in $D' = D - 2d$, however, the effective diameter is caused by many particles so the average diameter suffices for this calculation.

Particle density, ρ, is measured in a precise test and is therefore relatively free from error. Bulk density, γ, though, depends on the state of packing and is subject to more variation. The determination of γ was done with medium under test in a moderately dense state; this is the state that was felt to approximate the condition of the material as it was prepared for flow tests. γ could vary by 2 - 3 percent from that stated.

Accordingly, the dimensionless quantity

$$4Q/\gamma D'^{2.5} g^{\frac{1}{2}}$$

is shown with 3 percent error bars.

The theoretical calculation of θ' is dependent solely upon the value of ϕ. From actual observation, ϕ can vary as much as 10 percent between extreme values; with care, however, repeated values have been kept to a maximum 5 percent variation. A measurement of ϕ by another worker in this laboratory on the same Leighton-Buzzard sand gave a value of 31.3°. This variation of 6 percent represents work by two different observers. As the reported values were obtained by only one observer, the 5 percent limit is not unlikely. From equation (71), a 5 percent variation of ϕ when ϕ is near 30° gives a 3 percent variation of θ'.

The experimental determination of θ' is bound by much wider limits. Because of the difficulty of locating θ' during flow, a certain amount of judgement has to be exercised in evaluating both the wax-cast and perspex tube methods. If θ' from the wax-cast agrees with θ' from the tube and if the wax-cast shows that little or no "plucking" takes place, then that value

CORRELATION OF EXPERIMENT TO THEORY

Flow Fields

Rectangular Symmetry: Although no attempt has been made to establish an independent theory of failure in plane geometry, evidence has been presented to justify the conclusion that a radial bound cannot be applied to this type of flow. The qualitative, pictorial evidence, Figure 18, shows an inclination to piping for material, Leighton-Bussard Sand, that flows radially in conical geometry. The quantitative evidence, Figures 15 and 16, shows little change in flow rate with a decreasing, imposed θ'. Thus flow is construed as a vertical pipe that is unaffected by all but the steepest hopper walls. Since piping occurs, Brown's equation, (64), for flow from a trough cannot be valid.

Axial Symmetry: Theoretically sound hypotheses have been presented for the determination of θ'. Figure 23 is a plot of equations (69) and (71) upon which have been superimposed the experimental values of θ'. Both branches of equation (69) are plotted. An examination of Figure 23 shows that the determination of θ' is not precise enough to make a real choice between equation (71) and the positive branch of equation (69). (71) is preferred because it is derived from the same foundation as equations (74) and (75) for the flow rate.

Flow Rates

Several possibilities for theoretically determining the flow rate have been presented. Two equations, (74) and (75), have been uniquely derived in this report; one, equation (72), is derived herein, but is dependent upon Brown's minimum energy theorem; one other equation, (65), is due to Savage.

From the data described in the last section it is possible to make a

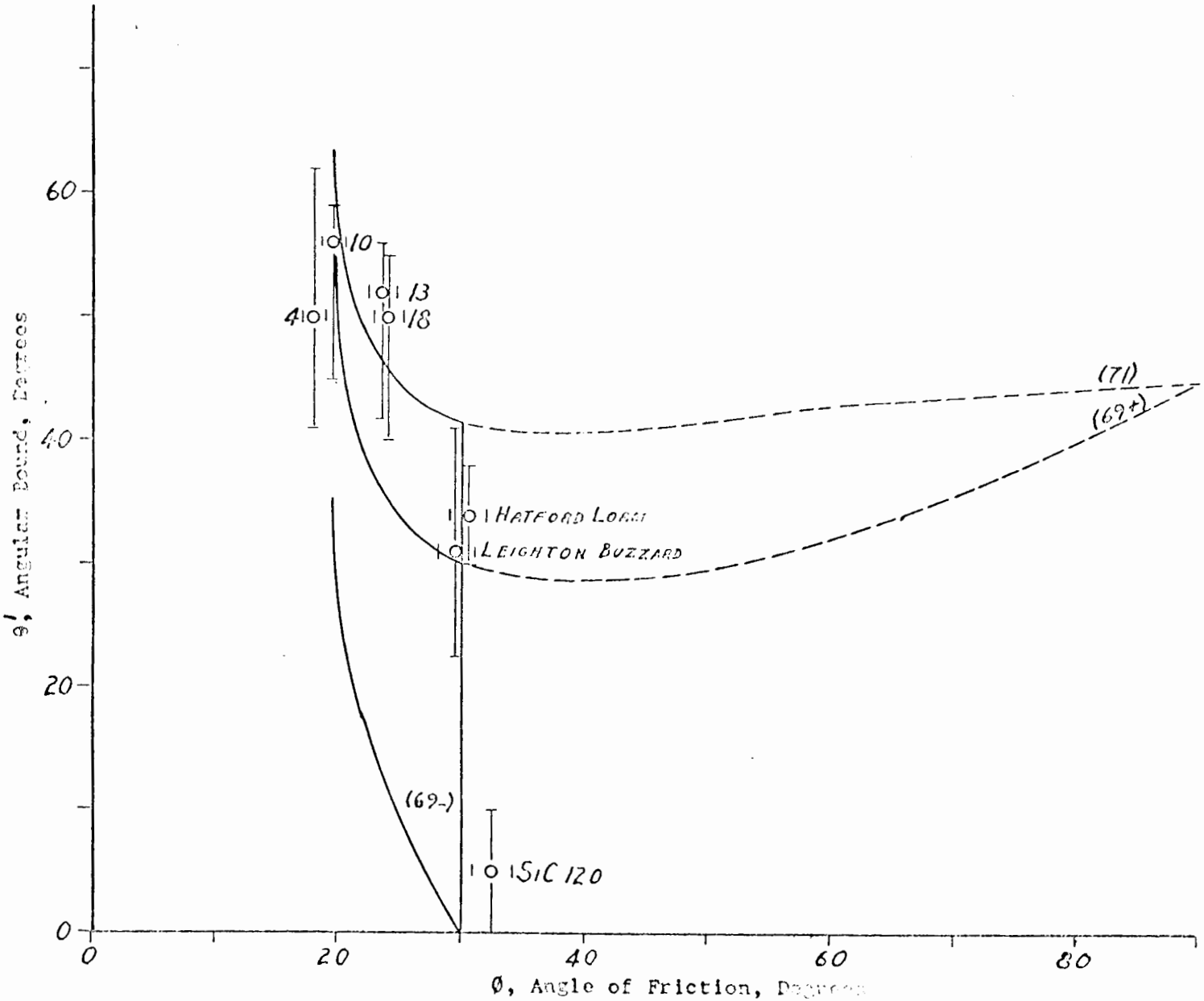

Figure 23: Natural Radial Bound, θ', versus the Angle of Internal Friction, Ø

comparison of experimental evidence with these equations on a plot of dimensionless flow rate against angle of internal friction. Figure 24 is this graph for θ' taken from equation (69); Figure 25 is the same for equation (71). Examination of these two graphs shows that equations have been devised that adequately bracket the experimental flow rates and thus can be used to describe the flow. Preference is given to the combination of (71) with (74) and (75) on the grounds that they represent the most theoretically inclusive approach to the description of flow.

Since it is not easy to vary the angle of friction and still maintain control of the other physical parameters; more evidence to decide which of the bracketing equations gives the best description is not forthcoming.

In constrained flow, that is in flow from a vessel with a conical bottom, the flow pattern, and hence the flow rate, is essentially that of a flat-bottomed vessel if the semi-vertical angle of the cone is greater than θ'. If the semi-vertical angle is less than θ', the case investigated by Savage and Brown is achieved. Thus on a plot of dimensionless flow rate versus θ', Figure 26, the data in Table 6 is graphed and compared with three theoretical curves. The first is Savage's with ϕ selected as 25°, the second is equation (74), and the third is Brown's equation, (72). In applying equation (74) to flow from conical hoppers, an assumption is made that in constrained flow the material behaves as if it had an angle of internal friction such as to give a natural bound coinciding with the imposed cone. This equation, in this context, is only valid for an imposed θ' lesser than the natural θ'; for $\phi = 25^{\circ}$, as with Savage's equation, $\theta' = 44.5^{\circ}$. This point is also shown on Figure 26.

Figure 26 demonstrates that as the angle of internal friction of the flowing material increases toward 30°, the constraining walls of the cones

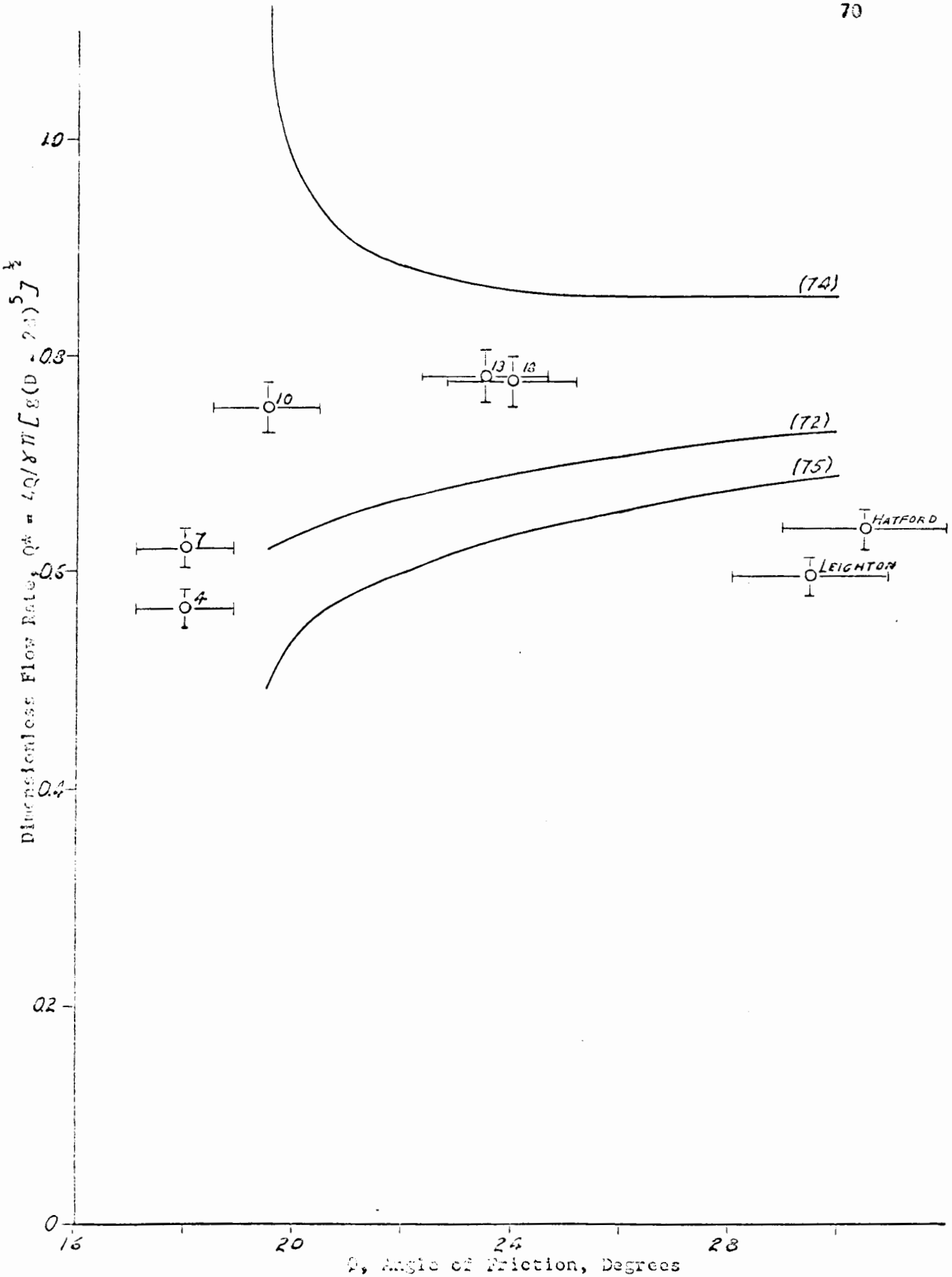

Figure 24: Flow Rate versus Angle of Internal Friction, Ø, with the Flow-Rate Equations Based on Equation (69) for the Radial Bound

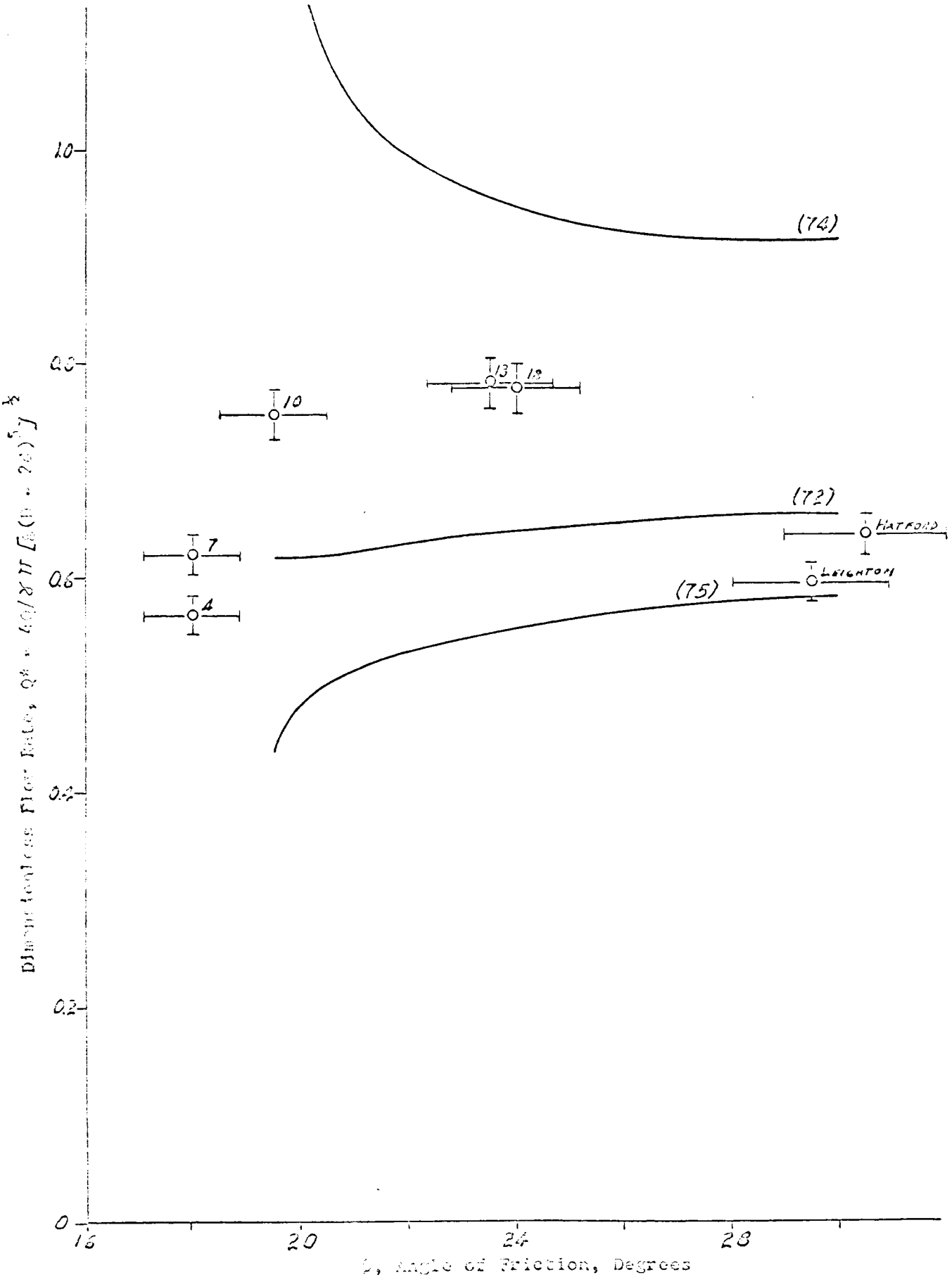

Figure 25: Flow Rate Versus Angle of Internal Friction using Equation (71) for the Radial Bound

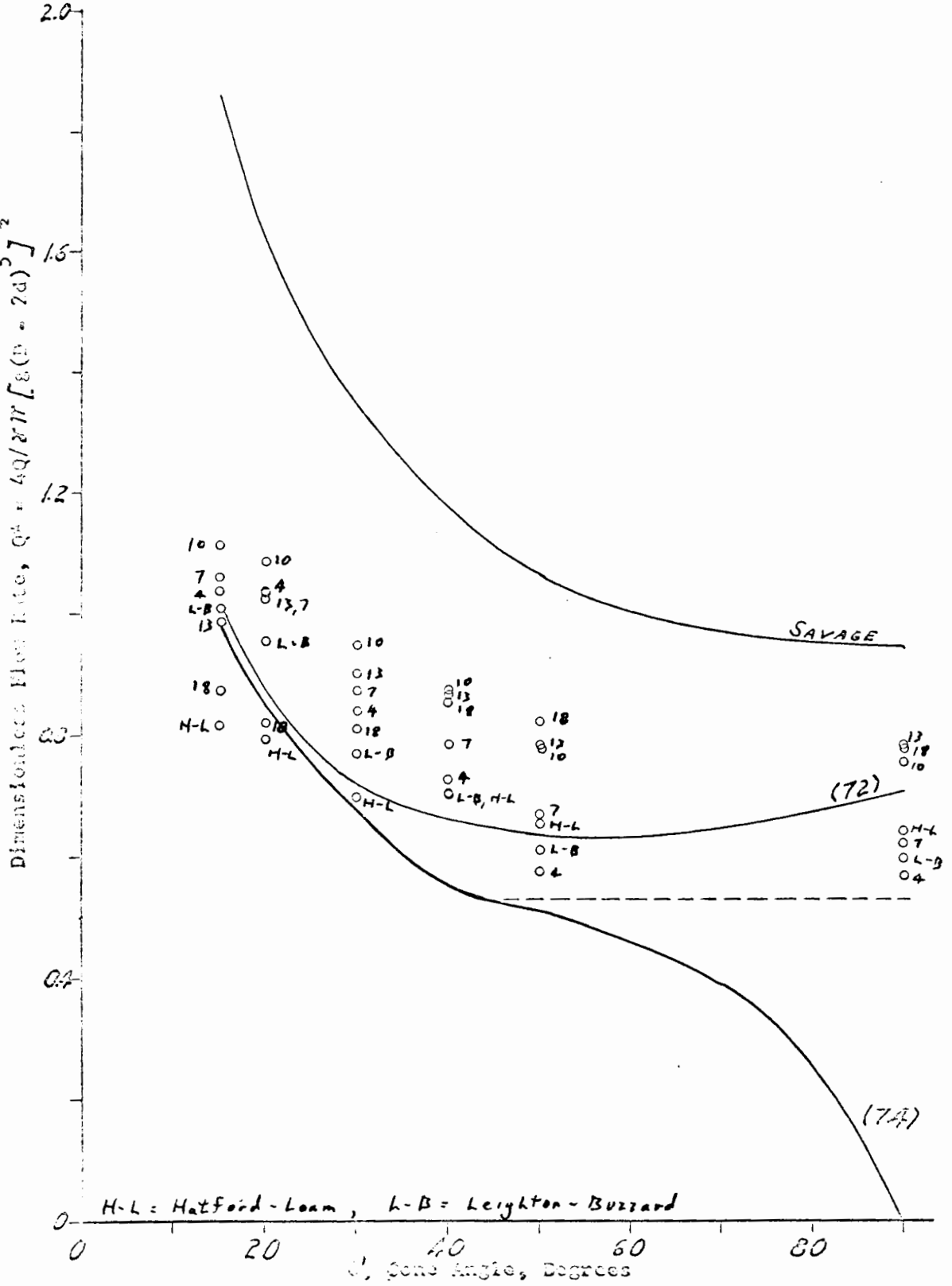

Figure 26: Flow Rate versus Cone Angle, θ', with Imposed Theoretical Curves

have a decreasing effect on the flow rate. Both Ballotini Number 18 and -100 +200 mesh Hatford-Loam Sand have near infinite slopes on this plot which demonstrates this point.

The proven dependence of θ' on ϕ makes the reversed assumption for equation (74), given just above, invalid. However, Figure 26 is useful to show that in axial symmetry, a greater flow rate results if constraining walls are chosen smaller than θ'. Presumably, this is because radii of the velocity profile which represent slower velocities are removed by the imposition of the constraining wall. This figure is of further use to determine whether Brown's approach of variation of velocity with θ and neglect of inertia effects or whether Savage's reversed approach best approximates a description of constrained flow. Both equations depend upon an imposed wall in order to be useful, therefore neither is valid for an imposed θ' greater than the natural θ'. However, Brown's equation, in spite of its drawbacks, best fits the data shown in Figure 26.

The final conclusion, discounting constrained flow, is that dimensionless flow of cohesionless material in axial geometry is dependent only upon the angle of internal friction of the flowing material.

SECTION II: A RELATIONSHIP BETWEEN FRICTIVE FORCES AND EARTH PRESSURE COEFFICIENTS

While attempting to discover the coefficient of friction between Hatford-Loam Sand and mild steel boiler plate, some interesting observations were made regarding the variation of lateral with vertical pressures in a contained granular medium. Although the experiments were undertaken to obtain information on the change of frictive force between steel and sand with increasing depth, the question of the selection of the proper coefficient of earth pressure, that is active or passive, became essential to a valid conclusion.

The original experiment was performed in the following manner. A bucket, 9-inches in diameter and 9 inches deep, was filled with Hatford-Loam Sand; a ¼-inch steel plate was buried in the sand with its top edge matching the free surface of the sand; and the sand compacted by use of a vibrator table. The plate was then pulled from the sand by means of a single-beam balance that was loaded in 10-gram increments. The experiment was performed, in one instance, with plates of varying length having the variable dimension vertical; and in the other instance, with the varying length horizontal. The results of this experiment are given in Table 10. This data is also plotted in Figures 27 and 28.

The frictive force can be related to the spatial parameters of the steel plate by

$$F = kPd^{x}, \tag{82}$$

where F is the force; k, a constant; P, the ~~perimetral surface~~ horizontal perimeter of the plate; d, the depth of the plate in the sand; and x, a variable. From the graph, it becomes obvious that, with constant depth, ~~the variable x is equal to one~~;

and that F varies linearly with P.

TABLE 10

FRICTIVE FORCE

Dimensions of Plate (horizontal first)	Area of Plate, in^2	Weight of Plate, gm	Average Lifting Force	Frictive Force, gm	Relative Frictive Force
3"x2"	13.0	195.8	576	380.5	1.00
3"x3"	19.5	290.5	1055	764.5	2.01
3"x4"	26.0	390.1	2255	1864.9	4.90
3"x5"	32.5	487.5	3850	3362.5	8.84
3"x6"	39.0	588.2	6125	5536.8	14.55
3"x8"	52.0	782.9	(exceeded limit of balance)		
2"x3"	13.0	195.1	800	604.9	1.00
4"x3"	26.0	389.3	1405	1015.7	1.68
6"x3"	39.0	587.5	2048	1450.5	2.40
8"x3"	52.0	782.1	2770	1987.9	3.29

Examining the logarithmic chart of relative frictive force against depth with constant P, it is seen that F varies with the 2.44 power of d, and that for this particular steel, k = 23.3, hence

$$F = 23.3Pd^{2.44}.$$

Thus it can be assumed that the frictive force increases as the depth raised to a power somewhat over two.

The frictive force is more logically related to the value of the normal force, as in the following equation

$$F = K_p \gamma \mu P \int_0^d d\,dz,$$

where K_p, the coefficient of ~~active~~ passive earth pressure is defined in equation (4); γ is the bulk density; μ is the coefficient of friction between sand and steel; P is the horizontal perimeter; and d is the depth. Expanding, this becomes

$$F = \tfrac{1}{2}\gamma P d^2 \mu (1 + \sin\phi)/(1 - \sin\phi). \qquad (83)$$

Equation (83), however, is a simplification of the process because it makes no allowance in the coefficient of lateral pressure for the friction that exists between the plate and the sand. Obviously, this parameter, represented by the angle $\tan^{-1}\mu$, is going to offset the slip surface in the sand. The use of Sokolovskii's pressure coefficients as found in Scott, page 412, ensures that this parameter is included. Therefore, equation (83) is used to determine the lifting force, but with earth pressure coefficients that are derived from curved rather than straight failure surfaces in the sand.

In order to evaluate (83) a value of μ = 0.469 was found by moving Hatford-Loam Sand across a steel plate, similar to those used in the experiment, in the shearbox tester. This value of μ corresponds to an angle of 25°; K_p is therefore 5.3 and μK_p is 2.4.

Since the Sokolovskii coefficients represent the limit of failure, forces calculated from equation (83) are higher than those measured. This difference is approximately 25 percent.

A solution of the forces from principles of elasticity, that is a Mohr's Circle analysis, gives values of the forces that are so low as to be meaningless. The high value of the lifting force, indicates that the sand fails in a plastic manner.

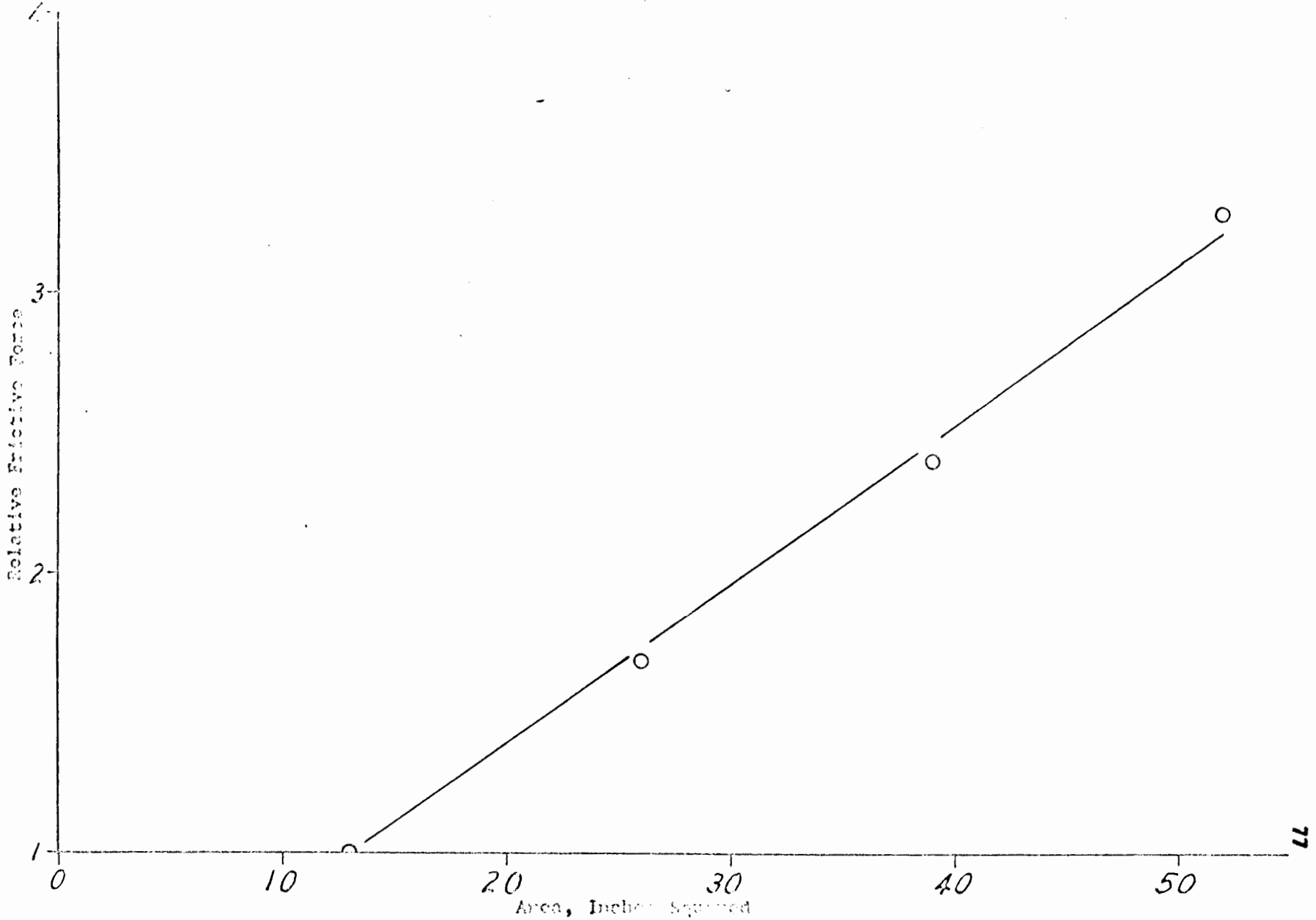

Figure 27: Relative Frictive Force versus Area; Variable Dimension Horizontal

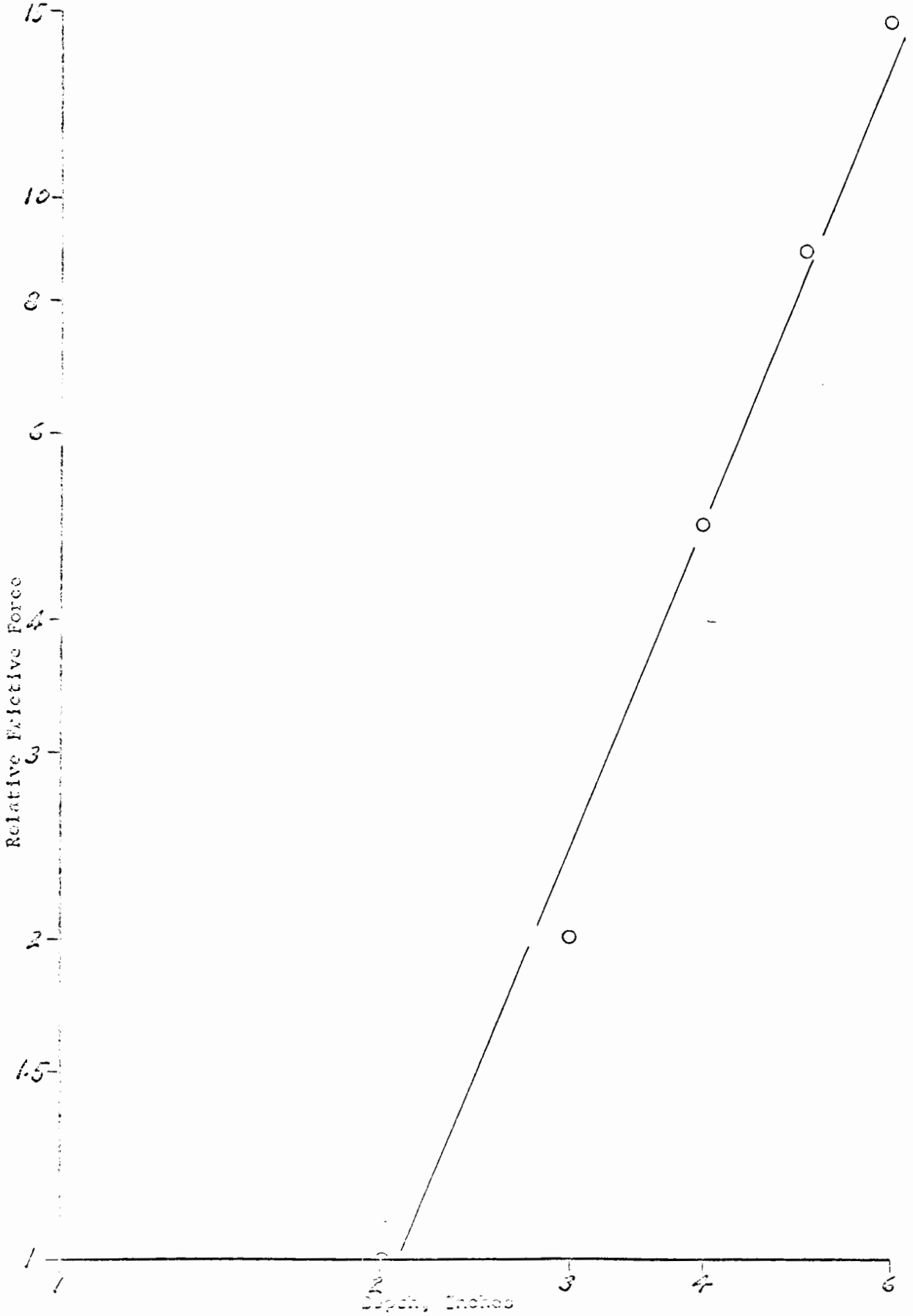

Figure 28: Relative Effective Force versus Area; Variable Dimension Vertical

SECTION III: IOWA - TANK STUDIES

INTRODUCTION

General

The methods of science and technology have long been put to use in order to examine the relationships between a flowing fluid and an immersed model. It is well known, in fact, that the studies of forces on immersed bodies have reached a fine and advanced state; drag forces on ships' hulls, streamlining of motor vehicles, and the broad question of aerodynamics are some of the fields that continue to receive vigorous attention. There is, however, a medium of immersion, soil, in which the measurement of drag forces has been negligible or related only to empirical factors.

The work presented in this section is an attempt to rationalize the knowledge of forces on model shapes as they are propelled through a soil medium. The project was undertaken because it contained opportunities for the variation of parameters within a controllable closed system.

The soil medium used throughout these experiments was the previously described Hatford-Loam Sand. It was felt that the use of this fine, dry, cohesionless soil would be ideal for obtaining repeatable results, and for providing a base for further experimentation. The work already accomplished is suitable for extension to cohesive soils, or to fluidized beds of sand.

With modern construction equipment becoming more complex and esoteric, hence more expensive, it is easily seen that any information leading to better design will be of value. The problem of an immersed body is encountered with such commonplace tools as deep plows and ripping points for bulldozers. The problem will be further realized as the heavy equipment industry moves toward the unification of processes and produces devices such as one-pass trench-diggers or cable-layers.

Previous Work

In researching previous work in this subject, it was found that such work as was done was directed either to the earthmoving industry or to the agricultural implement industry. The approach of virtually all past work was direct emulation of natural conditions.

Earthmoving inspired several of the papers (Cobb, Nelson and Selig, and Sullivan) that were examined. Unfortunately, the researchers were more concerned with relating draw-bar pull of scrapers or powering force of bulldozers to soil qualities than they were with examining boundary or depth effects. Nevertheless, the tow-rig design of the Caterpillar Company in their research laboratory (Cobb) and the more scholarly equipment of Nelson and Selig contributed ideas to the creation of equipment for this project. In addition, the latter's use of the theories of Coulomb and Rankine for passive earth pressure on a retaining wall in regard to moving bulldozer blades has given valuable clues to the mechanism of failure involved in the present case. In earlier two-dimensional tests referred to in the quoted article, Nelson and Selig show a case of initial failure that quite clearly resembles the Rankine criteria. In this article, they mention that after the blade had reached equilibrium of surcharge while moving through the sand, force oscillations occurred. They attributed this to successive shear failures.

The relevant work done in the agricultural field by Wells (1950) and also Payne (1956) is of more theoretical interst because Payne, at least, has considered both depth and speed effects. He states that the draft required by tillage implements is dependent on the weight of overbearing soil which varies with the square of depth. Of further relevance is the statement that force is related to the shearing strain rate and that a change of speed does not

affect the strength of the soil, or, consequently, the draft force. Nelson and Selig, whor refer to Payne in this instance, in justifying their use of a single experimental speed restate the hypothesis thus, "....speed has little effect on the behavior of cohesionless soils except when inertia forces become significant." Payne did his experiments on actual implements while in the field.

Wells' work is concerned with relating the draft force of two particular tillage implements to the physical characteristics of the soil through which they are pulled. A complete mole plow, instrumented to observe the component forces of draft, was one tool investigated. The other subject was a series of dihedral wedges that were examined because of their similarity to the mold board of a plow. They were winched through mainly cohesive soil at speeds of 0.50 - 1.00 feet per second. Wells states (page 41), with regard to the mole plow, that in the small range of velocities used there was no correlation of draft with velocity. Inasmuch as the soil media used were mostly cohesive, he attributed the draft mainly to frictive force on the sides of the instrument. Allowance is made (page 42), but not followed up, in cohesionless soil for the regulation of draft by the overburden pressure of the soil. An increase in depth gives only a linear increase in draft and this is accredited to the simple extension of surfaces of the support blade in contact with the cohesive soil (page 45). The work with wedges was done to relate drag force to the cohesive and rupture strength of the soil. "Point " resistance, or the drag created by fine piano wire, was also measured; this, of course, was a direct measure of the initial cohesion of the soil.

Aims

Given the previous statements about lack of work in the subject of forces on propelled bodies immersed in a soil medium, it might be well to state what the specific aims of this investigation are. The initial hope was to create a situation in which boundary effects would be negligible. That is, the towing tank would be designed wide enough and deep enough so that the model could move without interference from walls, floor, and free surface.

Depth variation, and its effect on the drag force, was to be examined; various models with different shapes, surfaces, and areas were to be looked at with the possibility of determining some form of drag coefficient for each type. Further, the towing mechanism would be designed so as to make possible changes of speed and thus examine the statement that the force is independent of speed changes.

Most important, it was hoped to gain a picture of the failure mechanism in the bedded sand which allowed the model to pass through it. All this was to be done with adequate control in order to acquire reliable information.

EQUIPMENT AND PROCEDURE

Mechanical Equipment

Tank: To contain the sand used in the experiments, and thus to keep the experiments manageable, a tank was designed and built. From the start, the scale of the research was kept large so as to fulfill the hope of avoiding boundary interference.

The tank was built to order by the Armfield Hydraulic Engineering Co. Ltd. and has overall dimensions, including supporting frame: of width, 3 feet 6¼ inches; height, 4 feet 5/8 inch; and length, 28 feet 6½ inches. Surmounting the respective sides of the tank is a rail, the details of which will be given shortly. The tank itself is constructed of 3/16-inch thick dural, and has internal cross-sectional dimensions, also shown in Figure 29 of width, 35 5/8 inches; of depth to start of circular segment, 24 inches; of total depth, 35 3/4 inches; and of arc of circle comprising the bottom, approximately 129 degrees. Its internal length is 28 feet. The frame of the tank was constructed of 6-inch by 3-inch channel steel; the details of this frame and the tank it supports can be seen in Figures 30, 32, 33, and 50. All seams and joints are welded. Joining of the tank to the frame is by two rows of bolts, the first 3 1/8 inches from the top of the tank, the second row, 21½ inches. The individual bolts are spaced one foot apart. The channel sections at the highest portion of each end have been subsequently strengthened by welding ½-inch steel plates across the channel and making it into a box section. This was done to give additional support and rigidity for the bases of the drive and tail pulleys of the towing chain. To give the tank flexibility of use it can be divided into three equal portions; drain points have also been built into each end.

The rails for the trolley are actually 2-inch by ½-inch equal-arm angle

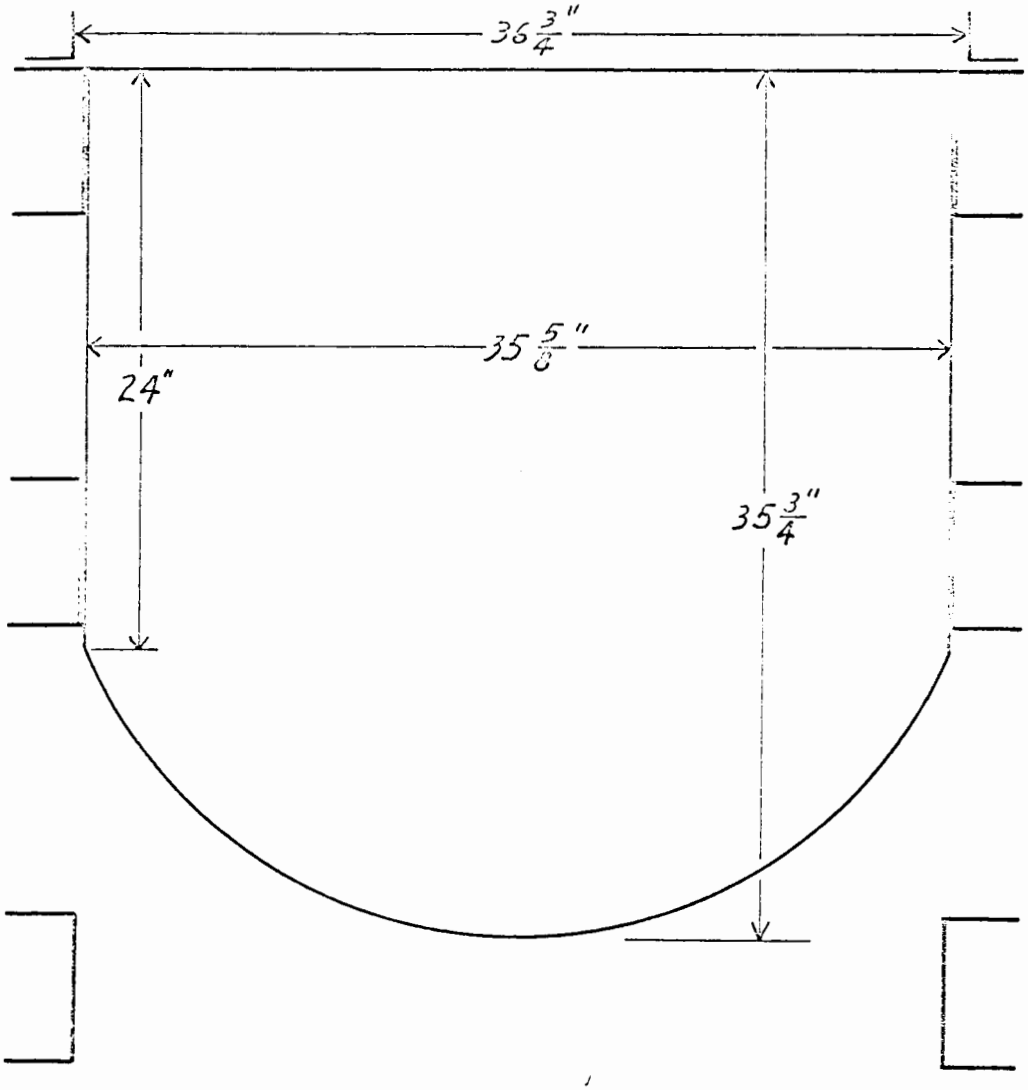

Figure 29: Tow-Tank Cross-Section



(a) Motor and End Chain Drives

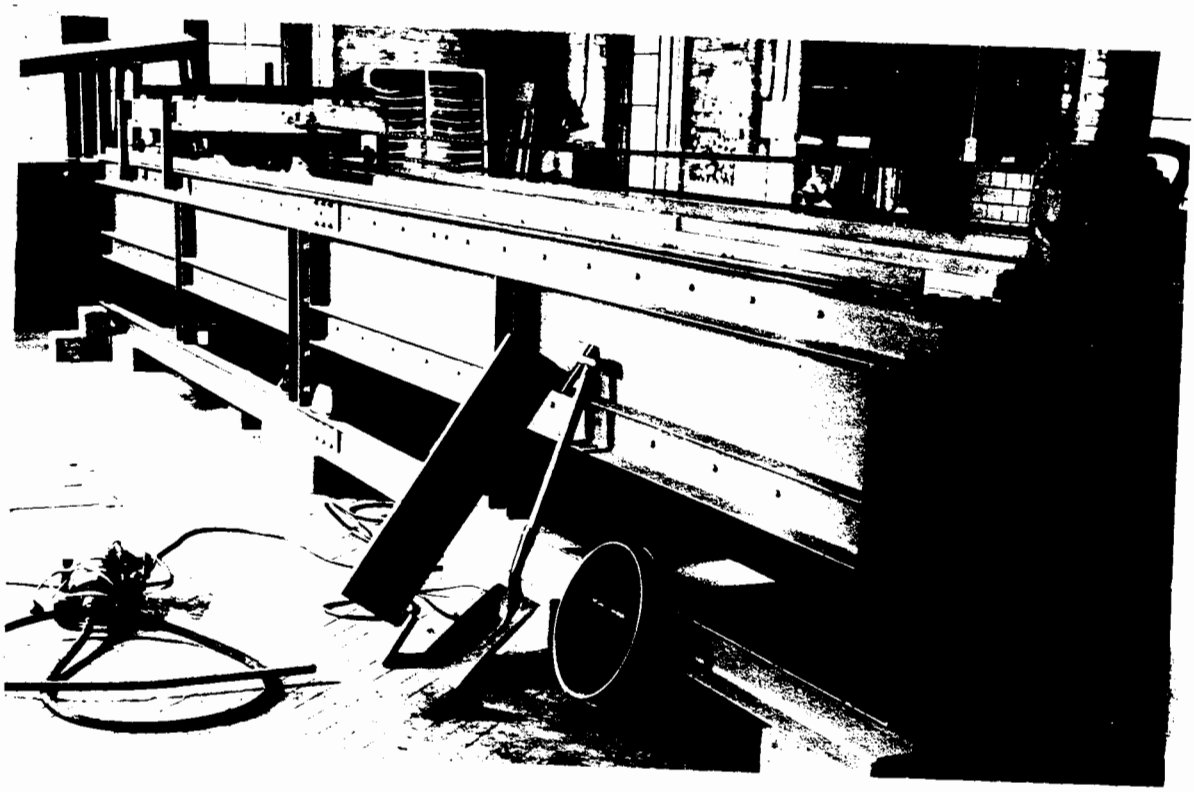

(b) Tank with Concrete Vibrator, Template, Shovel, and Screen

Figure 30: The Tank and Related Equipment

sections. They are supported by locking nuts on inverted bolts spaced one foot apart. The bolts are threaded into the uppermost side-channel of the frame and pass through slots, rather than holes, cut into the base of the angle section. The rails are thus adjustable for both height and width. The height of the rails above the highest point of the frame is 2 inches; above the channel that supports it, 2 3/8 to 2½ inches; and above the floor, 50 3/4 inches. The maximum variation in dimensions is 1/8 inch. Because of the adjustability of the rails, constant level and constant width of 36 3/4 inches has been maintained.

Drive and Gearing: The initial impetus for the towing drive comes from an AEI, Type BC, 1½-horsepower, reversible, single phase, induction motor with a speed of 1425 revolutions per minute. Power is transferred from the motor to a Crofts, 3½-horsepower, 60:1, 3-inch centers, Universal Mounting Type, "Radiation" worm reduction gear by a belt and two chain drives; all, but the motor, being mounted on the frame of the tank. The three successive drives, pictured in Figure 30, are used to provide flexibility in speed changes. The 1-inch belt and its two stock pulleys of 3½-inch and 7-inch diameter are also supplied by Crofts. The belt pulleys are affixed to their shafts by taper bush blocks. The chains are Renold's 110 046, ½-inch pitch, and the wheels and pinions used are standard. A variety of 19, 25, 38, and 114-teeth wheels are used to achieve speed changes. The shafts rotate in ball-bearings and the chains are properly tensioned by the use of shims under the bearing houses.

The output of the gearbox, which is mounted on the end structural member of the tank, is made linear by a 19-teeth, 6-inch diameter wheel which, with an identical wheel used as a tailstock, forms the support for the main

drive chain. This is a Renold's 110 038, 1-inch pitch. The chain is connected by shackles and threaded eyebolts to the trolley, thus creating an endless drive. Main chain adjustment is provided by the eyebolts and tension is maintained by a springed device on the trolley. The chain is viewed in Figures 30, 32, 50, and 52.

The end chain drives were chosen for their maximum flexibility with minimum costs. The components were purchased externally, but the system was designed and built by the laboratory work shops, thus insuring, if not sophistication, at least ease of maintenance and adjustment. The main chain was chosen after it was shown that ordinary wire rope did not have sufficient grip on its drive pulley. The roller type chains have given satisfactory and unfailing performance throughout the duration of the experiments.

Trolley: Like much of the other equipment in this investigation, the trolley that supports the test model grew in complexity as understanding of design needs was forthcoming. The two design criteria that were constantly adhered to in the trolley's construction were that there should be maximum support for the model with minimum interference of its travel through the sand, and that there should be a minimum of motion in all directions but the desired towing one.

The base of the trolley is an 1-inch board, 60 inches long and 40 inches wide, with 6-inch high sides also cut from 1-inch board. Affixed to the bottom of the trolley are four hard-wood blocks spaced to provide support for two axles. The wheelbase is 48 inches. Each axle supports its two wheels, kept at a separation of 36 3/4 inches by suitable collars, and a central guide pulley over which rides the chain. In the middle of the carriage is a third guide pulley, the axle of which is supported on springs,

and the chain rides under this pulley. The purpose of the three pulleys is to impart a downward force on the trolley -- keeping it on the rails -- by means of the chain tension, and to allow some springing, with a hoped for avoidance of shock damage, in the chain tensioning device. As was mentioned, the initial tension is created by means of threaded eyebolts that attach the chain to the ends of the trolley. The eyebolts are attached to the trolley by means of steel anchor blocks which are bolted to the floor and thus spread the load. The trolley, at this stage, is shown in a line drawing, Figure 31.

The trolley was further modified until it appeared as in Figure 32. The prominent change is the addition of outrigger wheels that serve to eliminate axial rotation due to moments created by force on the suspended models. The steel rail, used for its weight, serves the same purpose. Not seen, are two steel channels, 2 inches by 4 inches, that are bolted to the floor of the trolley to strengthen it both in tension and in flexure.

To explain how the model is linked to, and supported by the trolley, it is necessary to set down some terms. The probe is a beam of constant strength that holds the forward facing strain-gauge mount and model in place. The probe support is a quadripod that attaches the probe to the trolley and holds the base of the beam just above the level of the sand's free surface. These are shown in Figures 32, 33, 34, and 35. The probe support is an orthogonal, equal-arm, four-legged stand that is built of 2-inch by 2-inch Tee section steel welded to a cylinder, 4-inches diameter by 3 3/4-inches length. The tee sections, cut with a symmetrical 45-degree bias at each end, are 18 inches long from acute angle to acute angle. The legs are welded at one end to base-plates, 4 inches by 4 inches by ¼ inch, and at

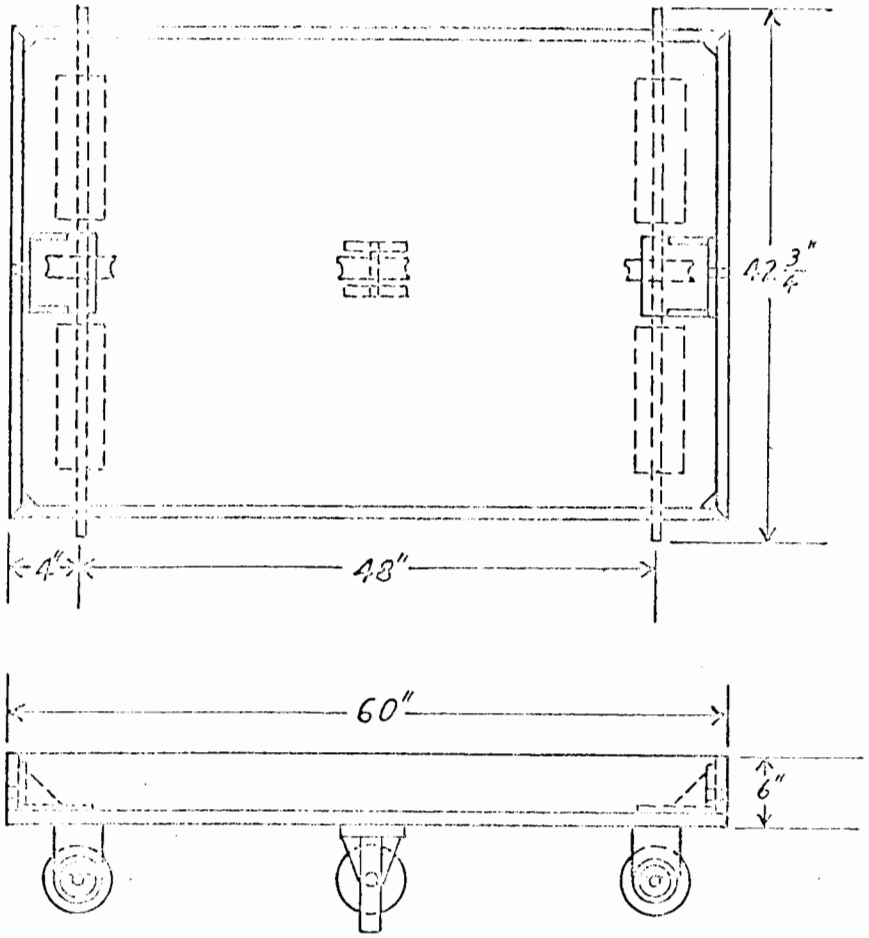

Figure 31: The Trolley

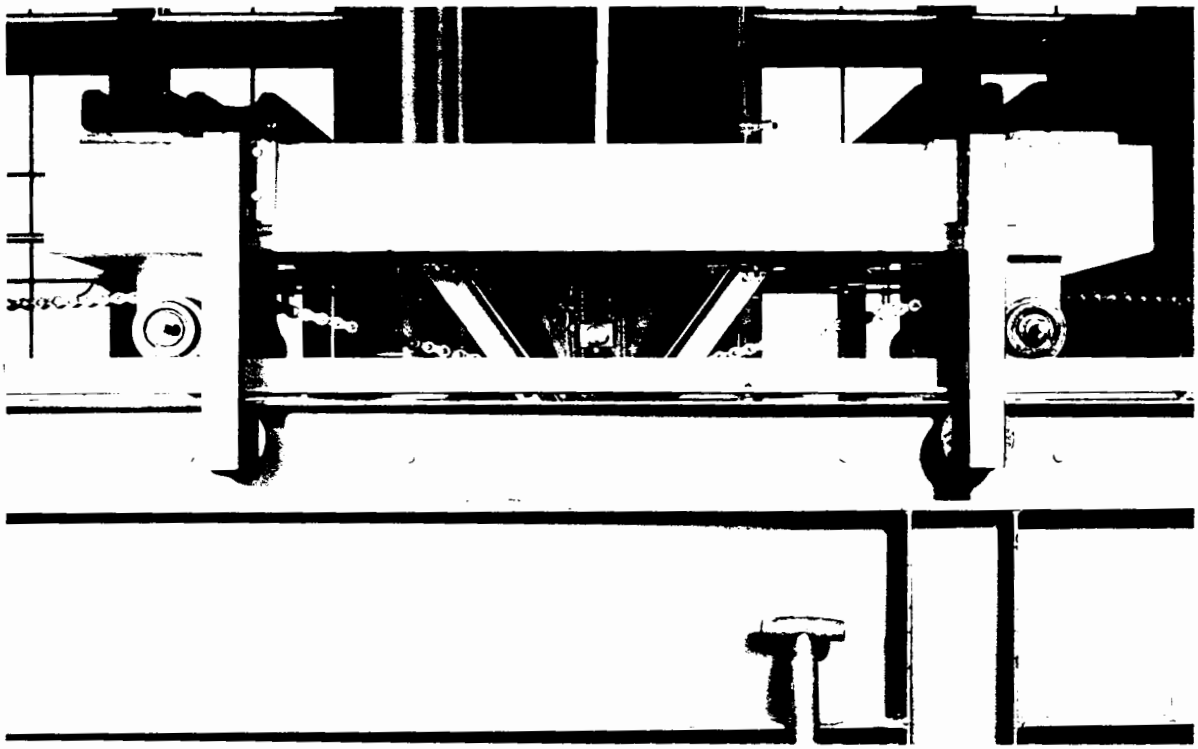

Figure 32: The trolley in Place



Figure 33: The Probe and its Support

the other end to the cylinder which has been bored and screw cut to accept a 2½-inch BSF thread. The support's standing height is 13½ inches.

The probe is composed of four parts: one of the various models, the strain-gauge mount, the lower beam and mount protector, and the upper beam. As can be seen, except for the model, each piece screws into the successive and more massive one supporting it. This was done to keep a minimum of probe mass near the model and still provide support and rigidity for the model at direct forces up to one ton. The upper beam was cut from mild steel and was originally 24 3/4 inches long with 10 inches of 2½-inch BSF thread; the remaining 14 3/4 inches tapers from a 2-inch diameter to one of 1½ inches. The long length of thread was provided so that a saw-cut was all that would be necessary to effect a change of depth. The 18, 21, and 24-inch depths were achieved with this beam. The 12 and 15-inch depths were provided by an earlier system that used the present lower beam as sole support for the model. The lower beam, best described by Figure 35, is constructed of high-strength, thick-wall tube and provides both support for the strain-gauge mount and protection for the strain gauges and their wires. It sticks out of the upper beam 2 3/4 inches making up the total test depth.

Most of the pieces of equipment described in this last section were designed to be the best solution for a problem imposed by the investigation. The magnitude of these problems, however, was not known until actual experimentation had begun. Therefore there was some earlier equipment the failure of which led to the succesful construction of the present. Although the data collected by the earlier pieces has been retained, it is felt that only the succesful, working system need be described.

Strain-Gauge Mount and Models: The strain-gauge mount, Figure 35,

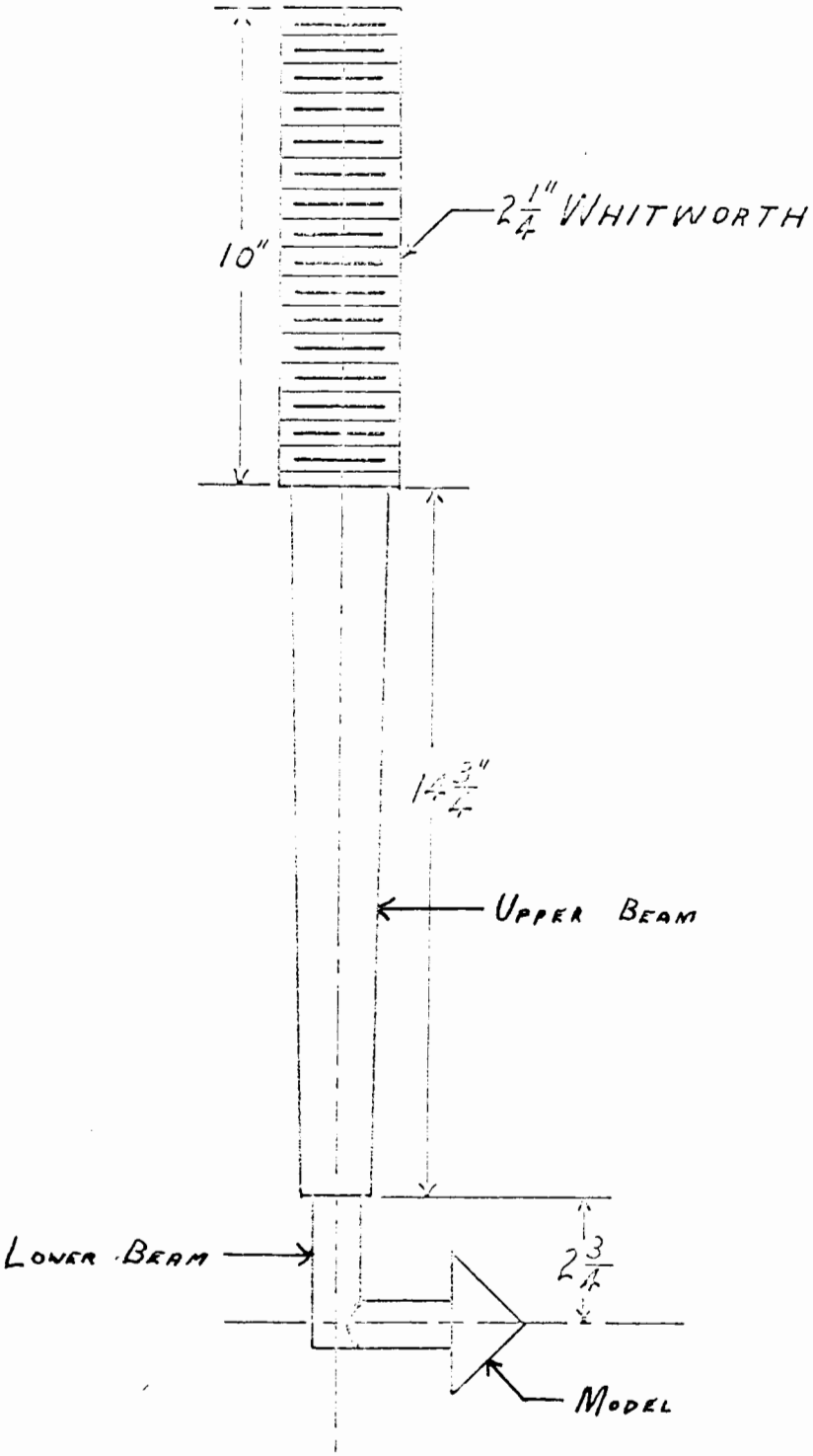

Figure 34: The Probe

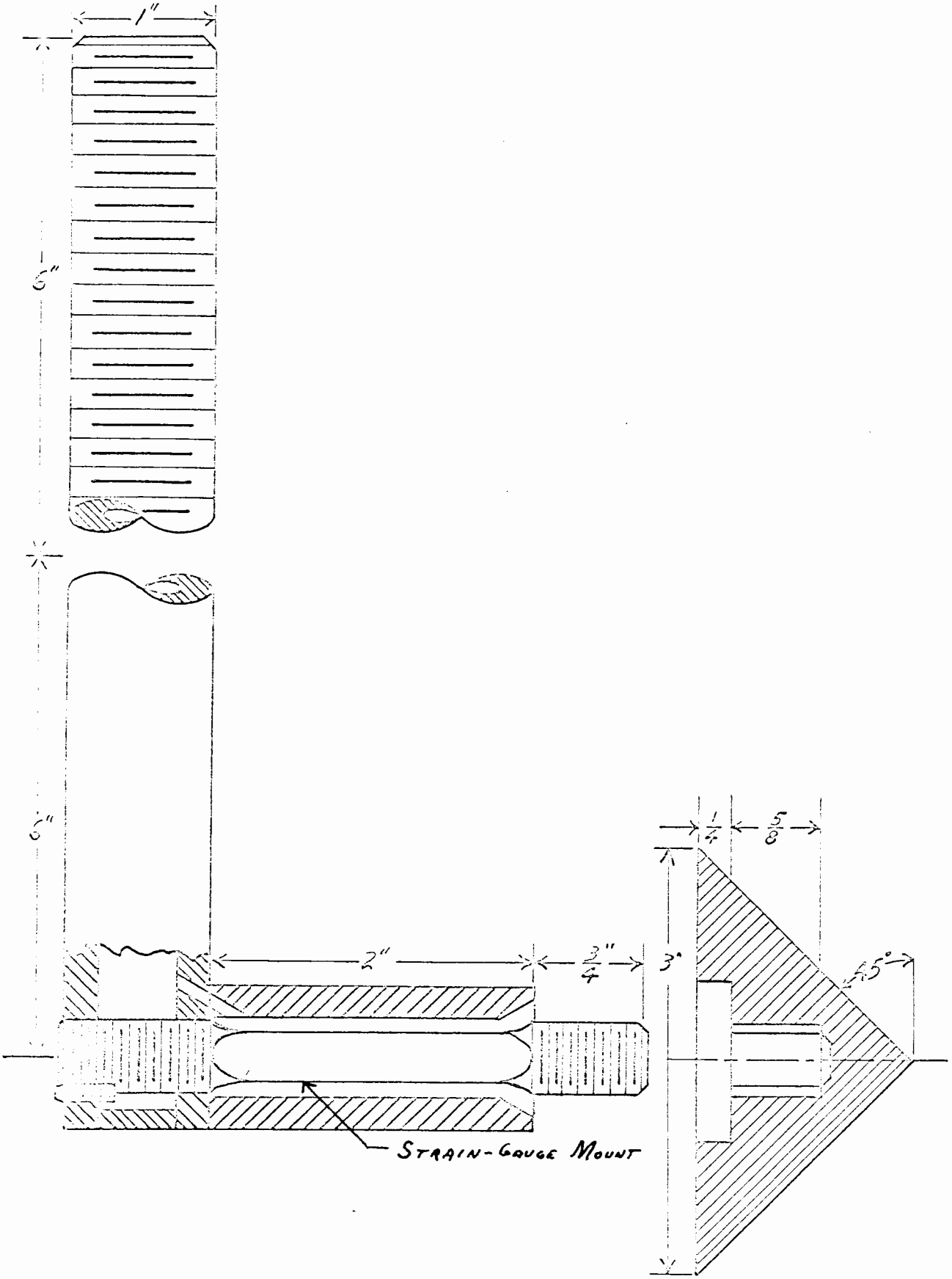

Figure 65: Section-View of the Lower Beam and Model, Showing the Strain-

Gauge Mount

holds the model firm and provides an accurate metal section from which strain can be measured. It is fashioned from ½-inch, mild-steel rod and has an over-all length of 3 7/8 inches. The modulus of elasticity, E, is taken from the Handbook of Chemistry and Physics to be 30.0×10^6 pounds per inch squared. The end of the mount that fits laterally into the beam has a thread length of 1 1/8 inches; the other end which supports the model has a thread length of 3/4 inch. The remaining two inches have been squared so as to have 0.350 inches per side, or a cross-sectional area of 0.1225 square inches. The actual area, averaged over the length of the test portion, is 0.1220 square inches. A set screw, as illustrated, holds the mount so that each flat surface is either exactly horizontal or vertical. A dummy gauge mount has also been prepared from the same material.

The models, pictured in Figures 33, 35, and 36, have all been turned from mild-steel rod to close tolerances. The surfaces of the models were polished so that there would be control of the surface friction parameter. (sec p. 107) All models are attached to the strain-gauge mount in the same way. In the middle of a central clearance hole, ½-inch deep and 1 1/8-inch diameter, a 5/8-inch deep hole is drilled and tapped to accept the strain-gauge mount. Since the mount extends 3/4 inch beyond its 1-inch diameter protective cover and since the total depth of hole in the model is 7/8 inches, the model, when fully screwed onto its mount, provides a complete cover for the strain gauges. The dimensions of the clearance hole insures that the model actually touches nothing but the mount to which it is attached.

The models, twelve have been used, are all circular in cross-section and can be classified as being cones on top of cylinders. The following Table and Figure 36 should amplify their characteristics.

For simplicity, some of the smaller models were made by reducing the

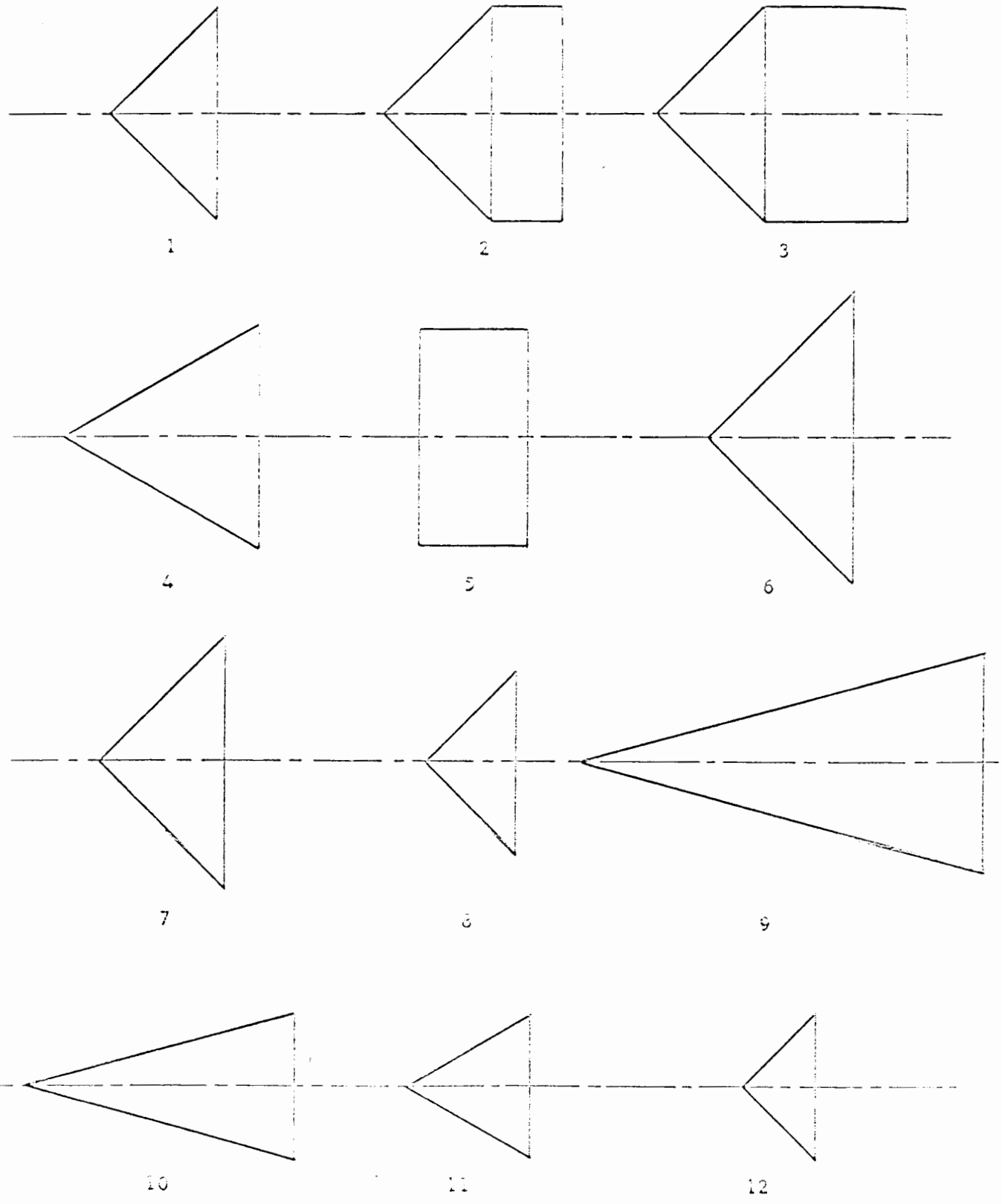

Figure 36: The Model Profiles, See Dimensions See Table 11

diameter of larger ones.

TABLE 11

MODEL CHARACTERISTICS

Number	Cone Semi-Vertical Angle, degrees	Base Radius, inches	Cylinder Length, ins.
1	45	1.500	0.0
2	45	1.500	1.0
3	45	1.500	2.0
4	30	1.559	0.0
5	90	1.500	1.5
6	45	2.000	0.0
7	45	1.750	0.0
8	45	1.250	0.0
9	15	1.500	0.0
10	15	1.000	0.0
11	30	1.000	0.0
12	45	1.000	0.0

Electrical Equipment

Strain Gauges: The heart of the sensing and recording system is the strain gauges. Those used in this experiment have proved to be quite satisfactory. In constant use have been T. M. L. polyester gauges, type PLS 10. These are resistance wire, copper-nickel alloy strain gauges utilizing a base of polyester plastic. The gauges have a resistance of 120 ohms and a gauge factor of 2.06; the gauge length is 10 millimeters. They have been adhered to the metal by T. M. L.'s CN contact adhesive.

The gauges were originally wired singly to the apex unit, not long after work began, however, they were wired in series pairs, each pair taking either the horizontal or the vertical direction. Thus a pair of gauges is mounted on opposite sides of the strain-gauge mount. The horizontal pair of gauges is circuit 1; the vertical is circuit 2. The reason for the change to paired gauges is discussed with the results.

Strain Bridge: The strain bridge, utilizing the afore-mentioned gauges, is primarily composed of commercial equipment purchased from H. Tinsley and Co. Ltd. The system is composed of a 25-point manual Apex unit, Type 4907-J, which provides balancing and switching; a Type 4907 Strain Gauge Bridge; a Type 6035 D. C. Amplifier; a 0 - 10 milliamp chart recorder, Type MSR, "Inkwell" built by Edgcumbe Peebles; and a few protective switches. The complete system is shown in the wiring diagram, Figure 37.

Pressure Gauge: In order to measure the pressure within the sand as the model passed by, a soil pressure gauge, Type SPIM, was purchased from the Saunders-Roe Division, Westland Aircraft Ltd. The gauge utilizes foil strain gauges, mounted on the inside of both ends of a short cylindrical cell, that are wired in a full bridge with all four arms active. The input to the bridge is from a six-volt battery, the bridge resistance is 229 ohms, the bridge capacity is rated as 0 - 30 pounds per square inch, and the output as 42.4 microvolts per volt applied per pound per square inch.

The gauge, Figure 38, was mounted on a board 2 feet by 5 inches by 3/4 inch, the ends of the board having been squared to the sides.

The output of the gauge was read directly from a Philips valve voltmeter Type GM6020 that shows polarity and has a range of 0.001 millivolts to 1000 volts, or the output was plotted on a Mosely "Autograf" X-Y recorder, Model 7030A, with an 'X' and a 'Y' range of 0.1 millivolts per inch to 20 volts per inch and a built-in sweep of 0.5 to 100 seconds per inch.

Procedure

Sand: The sand, Hatford-loam, as described earlier, weighed approximately 10 tons when delivered. Before it was placed in the tank it was dryed to approximately 0.1 percent moisture by placing a set quantity over a frame

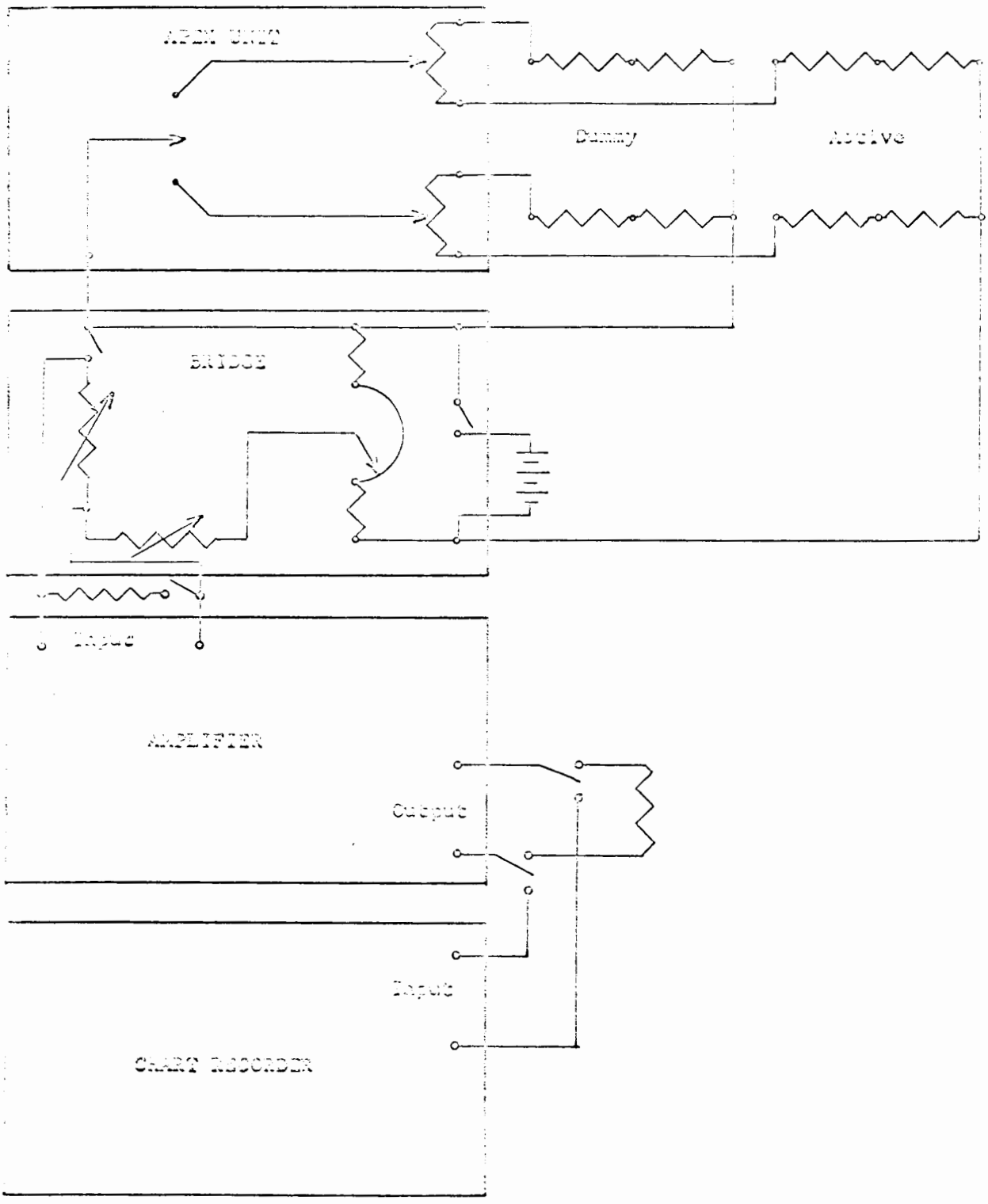

Figure 37: Strain Bridge Circuit Diagram

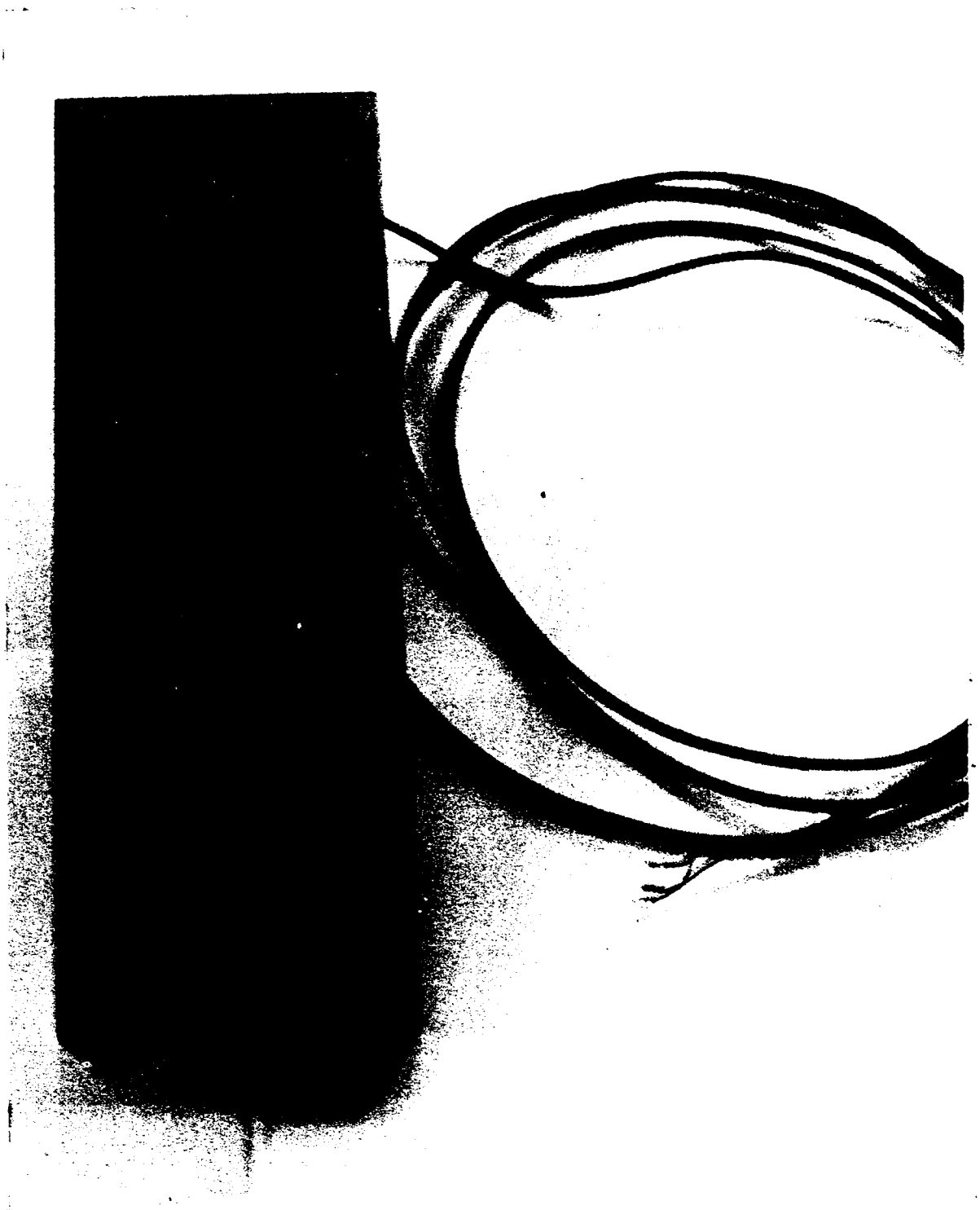

Figure 38: The Soil Pressure Gauge

through which stretches an Rumex Mains Warming Cable, Number 1C8, 300 watts and 80 feet long. After drying, the portion of sand was placed in the tank and the process repeated until all was transferred.

When filled and leveled, the sand occupied two-thirds of the tank. Rather than seal it off with a portable bulkhead, that end was left unconstrained, Figure 33. Thus the model could be towed into and out of the sand gradually and with a minimum of fuss. Also, the unoccupied portion of the tank provided a good place for working on the undercarriage of the trolley.

In order to ensure that the sand was uniform, before every run it was vibrated and leveled. The procedure for this was simple; a few spadefuls of sand were taken from the free end and distributed where the exiting probe had left a trough. The sand was then vibrated by poking an electrically-powered concrete settler, Compactors Engineering Ltd. Type E40, with 1-inch head, into it at 18-inch intervals; and then the sand was leveled with a template that slides over the rails and keeps the sand 8 inches below them. With the probe support height at 13½ inches and with the height of trolley over the rails at 6 inches, the additional distance of 8 inches places the sand at a point below the probe support just sufficient to allow room for a locking nut to keep the probe still in the probe support. Despite all efforts, from evidence of force runs, the sand was never completely homogenous.

When the model was run into the sand a small surcharge developed in front of the probe and its support. This was allowed to occur, and the readings were only counted after the height of the surcharge had reached equilibrium. The depth, however, was always counted as the depth of the model compared to undisturbed sand.

Strain Output: The first step in obtaining a record of the force level

on the model during the run was to switch on the amplifier, which is powered through a 50-watt Advance Volstat to eliminate voltage fluctuations, and allow it to warm up. The input of the amplifier was kept shorted during this period and the output was fed through a dummy resistance to protect the chart recorder from any high currents that may have been induced. The gauges were then supplied with 6 volts, the output of the bridge switched to the amplifier and the protective devices switched off.

The second step before each run was to calibrate the output of the recorder to the output of the bridge. For most runs, a calibration, using the 1 percent range of the amplifier, of 10 milliamps, chart full scale, equal to 0.1 percent resistance change -- 10.0ma = 0.10%ΔR/R -- was used. Thus the bridge slide-wire was placed at +0.05%, the pen on the chart recorder was zeroed with the balancing resistor in the apex unit, then the slide-wire was placed at -0.05%, the pen was brought directly to 10.0 ma with the galvanometer sensitivity control, this procedure was repeated for the other circuit, and then the pen was left centered by leaving the bridge slide-wire at zero.

The trolley was then set into motion and allowed about 3 or 4 feet of travel for surcharge equilibrium to occur, then a reading on each of the circuits was taken over a further 3 or 4 feet apiece. When the trolley was returned to its original position, a zero-drift check was made. Each complete run was numbered and a short description of the details placed into notes. For each circuit, on each run, the chart was read for maximum and average strain. Utilizing the gauge factor formula, $\epsilon = 30.0 \times 10^{6}$, and the fact that 1ma = 0.010%ΔR/R, 1ma on the chart is equal to 177.5 pounds of force. Every determination is repeated four times in order to obtain a

mean value and as a check for constancy.

Pressure Output: In order to obtain a plot of pressures within the sand as the model passed through it, the pressure gauge was buried at varying points along a cross-sectional plane and test runs were performed. Before the pressure gauge was buried into a new position, a record was made of the gauge output with approximately 6 volts input. The gauge was buried, a spirit level being used to insure verticality, the sand was leveled and vibrated, taking care not to poke the vibrator too close to the gauge, and the position of the gauge ascertained by measuring the height of the mounting board above the sand -- the gauge was mounted a set distance below the top of the board -- and the distance of the board from the side. The output of the gauge and the battery was recorded before and after the run and the load output was recorded as the maximum reading achieved during the run.

An X-Y plotter was occasionally used in conjunction with the voltmeter to obtain a visual readout of the pressure information and thus a check for any errors. All pressure tests were run at the same speed, that is 3.27 feet per second.

RESULTS

General

The original object of this investigation, as stated in the introduction, was to relate depth, model, and speed variation to force on the immersed model while maintaining an independence from boundary effects. These objects have been achieved, and in doing so, many other interesting facts and relationships have been elucidated. The following sections set down the salient features of these observations.

Depth

Initially, it is assumed that the force on the model is related to the weight of the overbearing material. Inasmuch as weight is directly related to volume, and dimensionally volume is L^3, it is further assumed that the force is related to the depth cubed, $F \propto d^3$ or $F = kd^3$. In order to obtain an empirical check on this assumption, a series of runs at depths from 12 to 24 inches, taken at 3-inch intervals, was made. The model, number one, used was the same for all experiments; as was the speed, 3.27 feet per minute = 0.0545 feet per second. All speed determinations have been made with a stopwatch that has a minimum interval of 0.2 seconds. The chart speed was 10 inches per minute or one inch of chart equaled 0.327 feet, 3.92 inches, of trolley travel. Because this was the first of the parameters to be worked on the first eleven runs were discounted for initial operating "bugs". The following table sets down the results of depth variation.

The information in Table 12 is graphed in Figure 39. A logarithmic scale is used so as to readily determine the exponential power from the slope. The error bars represent standard deviations determined from the results; there is a full discussion of errors in a later section. The max-

imum slope is between the 12-inch and 15-inch points and is 2.79, the overall slope is 2.27, and the minimum slope is between the 15-inch and 18-inch points and is 1.66.

TABLE 12

FORCE RELATED TO DEPTH VARIATION

Depth, inches	Number of runs	Average force, pounds	Tolerance, s
12	5	240	7
15	4	444	10
18	14	576	54
21	10	791	67
24	7	1150	97

Model Variation

General: The next parameter, or rather, set of parameters involves model variation. The set is subdivided into two principal groups: projected area constant and projected area varied. The first group is further subdivided into three more groups: variation of length of backing cylinder, variation of cone angle, and variation of model surface. Some of the models overlap in their purpose; for instance, a few models vary both area and cone angle.

Projected Area Constant, Cylinders: Models 1, 2, and 3 with an 1½-inch radius, 45-degree cone, and backing cylinders of length 0 inches, 1 inch, and 2 inches, respectively, were used for this parameter determination. The object was to discover the value, if any, of forces perpendicular to the model. Since all tests in this series were run at 18 inches of depth, with a speed of 3.27 feet per minute as before, it can be estimated from $P = \gamma h$, that the pressure on the top and bottom of the model is an average 1.0

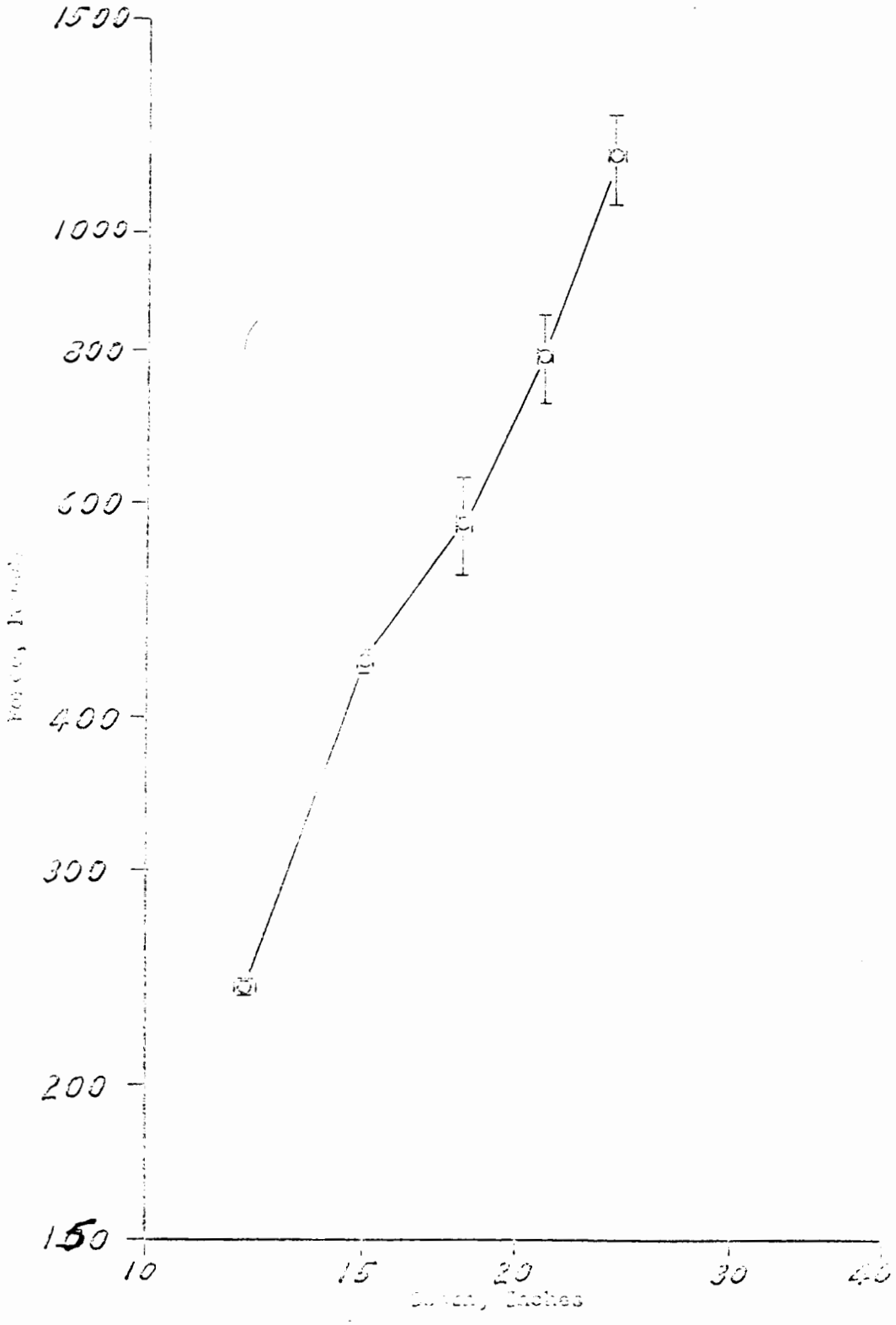

Figure 39: Force Versus Depth

pounds per inch squared. The pressure on the sides, using the ~~active~~ passive earth pressure coefficient, is ~~only 0.3~~ 3.0 pounds per inch squared. The average pressure on the model would then be ~~0.65~~ 2.0 pounds per inch squared, and with μ, measured in Section II, at 0.47 the drag would then be ~~0.305~~ 0.94 pounds per inch squared. Thus for the 1-inch cylinder, an increased drag of ~~2.9~~ 9.1 pounds could be expected; for the 2-inch cylinder, an increase of ~~5.8~~ 18.2 pounds could be expected. In fact, as shown by Table 13 and Figure 40, the graph of the tabular information, there is relatively little increase in force to correspond to the increase in length of the backing cylinder.

TABLE 13

EXAMINATION INTO FORCES NORMAL TO THE MODEL

Model No.	Cylinder Length, inches	Number of runs	Average Force	Drag Increase	Tolerance
1	0.0	4	541	--	3
2	1.0	8	535	-6	37
3	2.0	8	540	-1	25

As before, the tolerance is the standard deviation determined from the data gathered from the runs of a single variation. During model variation, model number one was rerun and it is the value thus obtained which is reported above.

Projected Area Constant, Cones: The next parameter, variation of the cone angle, was investigated with models 5, 1, 4, and 9, also 12, 11, and 10. The first series has a radius of 1½ inches and semi-vertical angles of 90, 45, 30, and 15 degrees. Because the 15-degree cone caused too great a moment on the strain-gauge mount during force oscillations, the second series of cones with constant radius of 1 inch and angles of 45, 30, and 15 degrees was tested. As before, all tests were at 13 inches of depth and at a speed

of 3.27 feet per minute. The results are contained in Table 14.

TABLE 14

VARIATION OF CONE ANGLE

Model	Radius	Cone Angle	No. Runs	Average Force	Tolerance
5	1.5	90	8	534	38
1	1.5	45	4	541	3
4	1.559	30	8	554	25
9	1.5	15	2	556	?
12	1.0	45	6	316	0
11	1.0	30	4	278	27
10	1.0	15	8	328	23

This information is plotted in Figure 41.

The expected result is that there would be little variation of force with change in cone semi-vertical angle, θ, according to the following reasoning. Unit drag is directly proportional to unit normal force, and normal force is related to frontal force (as measured on model 5, hence the force on a projected area) by $\sin\theta$. Total drag is obtained from unit drag by multiplying it by the area of the cone, however the area is related to the projected area by $1/\sin\theta$, therefore $\sin\theta$ times $1/\sin\theta = 1$ and there is no variation in force. Within limits, the results confirm this analysis.

Projected Area Constant, Surface: Following the reasoning stated in the last section, it can be assumed that a variation of the model surface would make no difference to the force on the model. To check this, the surface of model number one -- 45-degree semi-vertical angle, 1.5-inch radius, no backing cylinder -- was changed by adhering grains of Hatford-Loam sand to it with Araldite. This change of surface effects a 25 percent increase in μ, the coefficient of friction. As measured in a shear-box tester, the coefficient of friction of Hatford-Loam sand on mild steel is

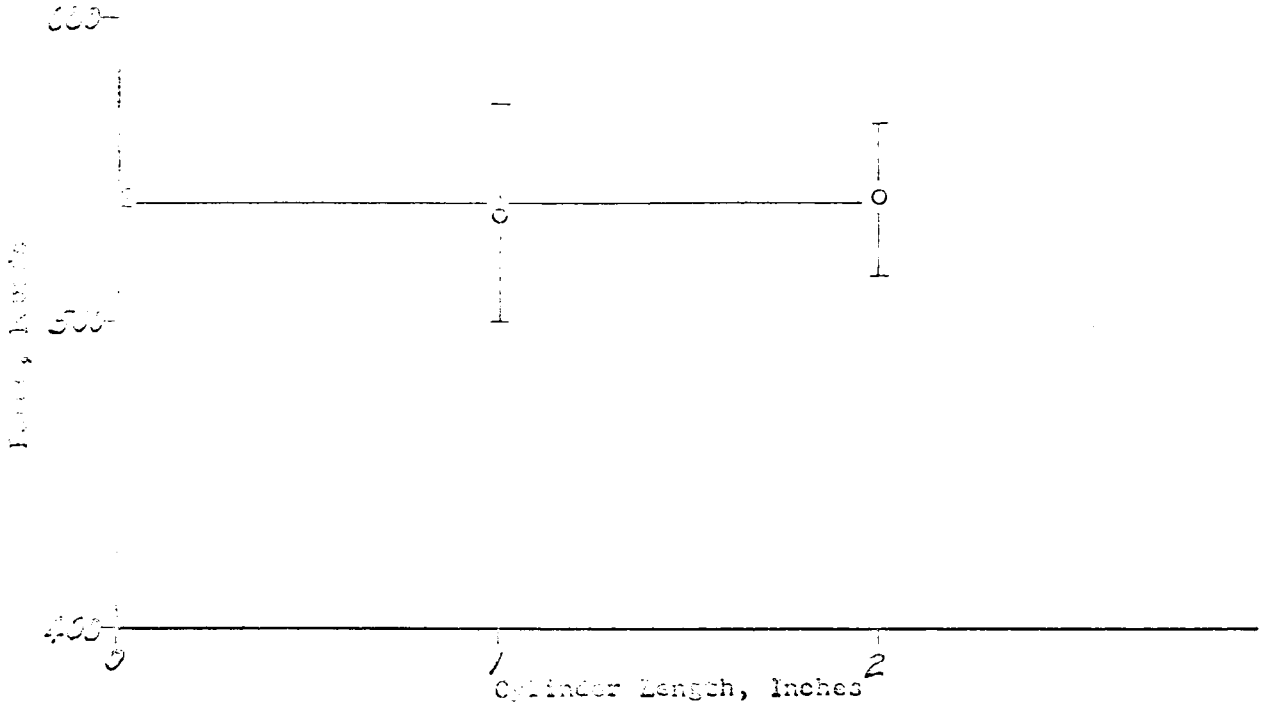

Figure 40: Force versus Cylinder Length

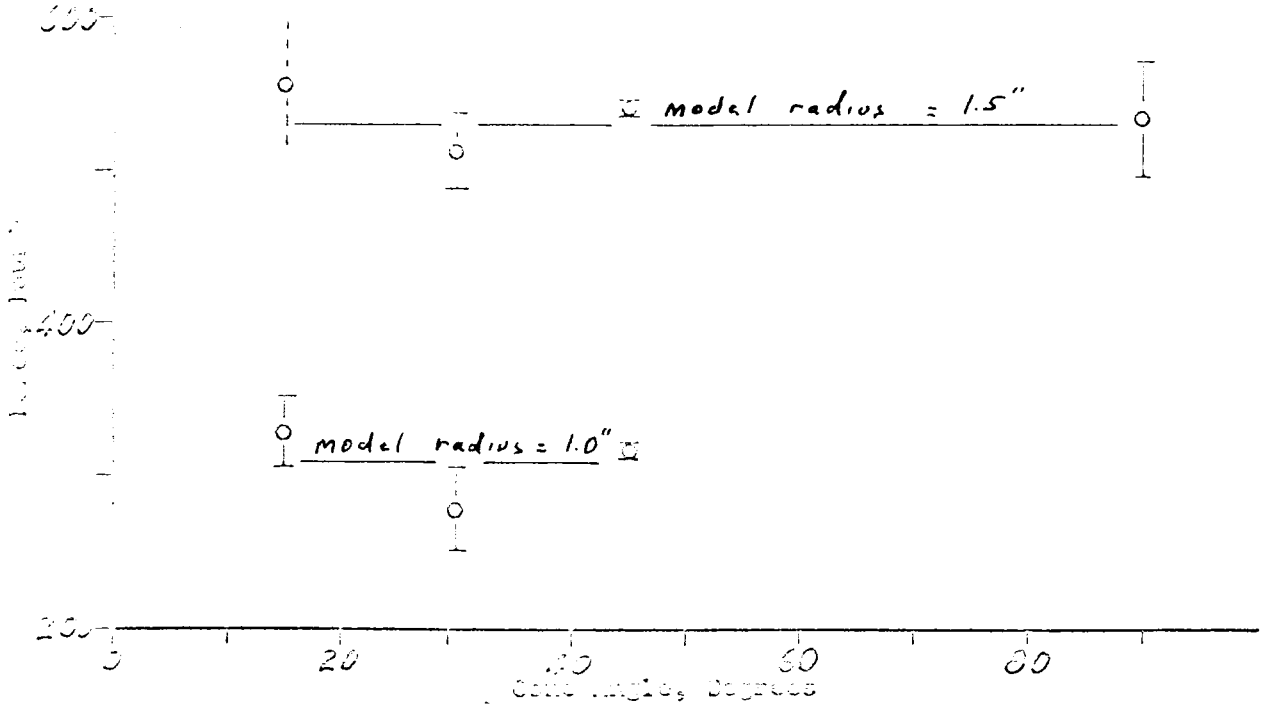

Figure 41: Force with Variation of Cone Angle

0.47, and, triaxially measured, μ of the sand on itself is 0.59. A series of test runs were made with this model at the 18-inch depth and with a speed of 3.30 feet per minute. Over eight runs the average force was 535 pounds, with a standard deviation of 25 pounds. Compared with the value for model one with a smooth surface, 541 pounds, the new value is seen to be slightly more than one percent less. Because the variation is both small and negative, the assumption is justified and no further testing was done on this parameter.

Projected Area Varied: The last model variable to be examined was the variation of base, hence projected, area of the cones. In this, models 6, 7, 1, 8, and 12, 11, and 10 were used to obtain radii of 2, 1.75, 1.5, 1.25, and 1 inches. The depth was 18 inches and the speed was constant at 3.27 feet per minute.

It is expected that the force will vary linearly with the area, or the radius squared, and thus the data from these runs is tabularized, Table 15, and graphed, Figure 42, against the radius squared.

TABLE 15

FORCE VERSUS RADIUS SQUARED

Model	No. Runs	Radius	Radius Squared	Average Force, pounds	Tolerance, s
10	8	1.0	1.0	328	23
11	4	1.0	1.0	278	27
12	6	1.0	1.0	316	0
8	6	1.25	1.5625	389	14
1	4	1.5	2.25	541	3
7	8	1.75	3.0625	717	24
6	8	2.0	4.0	933	76

With the assumption that the origin forms one of the test points, the slope of the graph is 239 pounds per radial inch squared. If this is further divided by π, the slope, or unit force, F/A, is equal to 76 pounds/square inch.

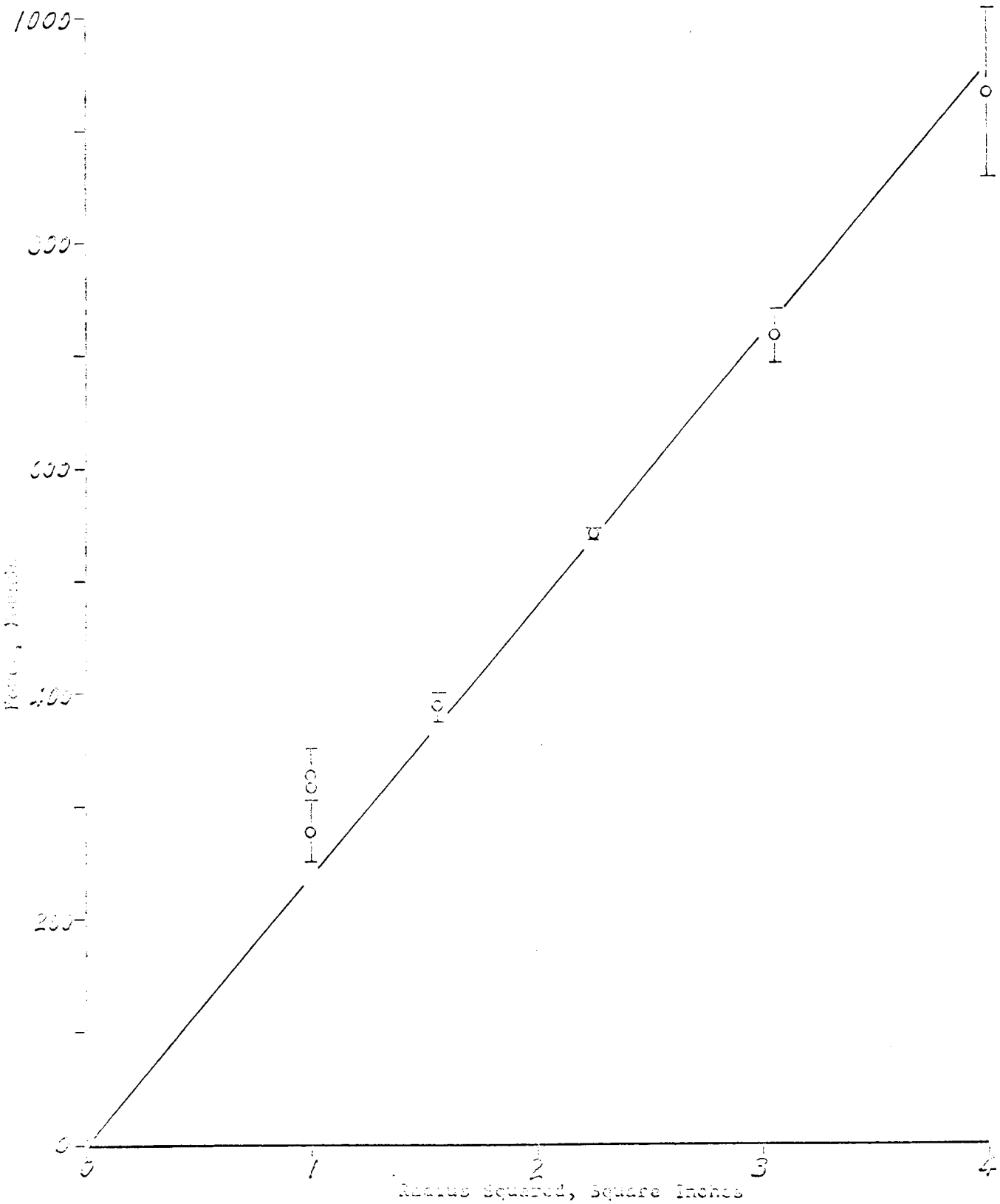

Figure 42: Force Versus Projected Area

Speed Changes

As was explained in the section on mechanical equipment, speed changes were achieved by changing the radii of the chain-drive pulleys that connect the motor to the gearbox. Knowing that the motor speed is 1425 revolutions per minute and that the gearbox reduction is 60:1, Table 16 lays down the gear wheel combinations that achieve the speeds used; it also sets down the calculated speed and the speed actually observed. The change from radial to linear motion is made with a 6-inch diameter pulley on the output of the gearbox.

TABLE 16

SPEED CHANGES

Motor to 5/8"-Shaft	5/8"-Shaft to 1"-Shaft	1"-Shaft to Gearbox	V, Calculated, ft/min	V, Actual, ft/min
2 : 1	38 : 19	114 : 19	1.53	1.68
2 : 1	25 : 19	114 : 19	2.40	2.50
2 : 1	25 : 25	114 : 19	3.15	3.27
2 : 1	19 : 25	114 : 25	5.45	5.67
2 : 1	25 : 25	38 : 19	9.44	9.79
2 : 1	25 : 25	25 : 19	14.34	15.09

The calculated speeds are all approximately 4 percent less than the observed speeds indicating a constant deviation in one of the stated values. This is of no real concern because all speeds were double-checked with a stopwatch. An increased chart speed is used with the 15.09 feet per minute speed.

As part of this parameter investigation, the model was run into the sand and held there with the strain recording equipment left on. At intervals the chart drive was switched on, thus giving a record of the static force against the model. Over a period of 53 minutes the only change in the

recorded value of strain was due to a slight change in output voltage of the batteries. This was indicated by a slight zero shift. Figure 43 is a copy of the chart for this run. The speed, until the model was halted, was 15.09 feet per minute; indicating that the forces on the model at all speeds up to 15.09 are due to static effects alone. Further, for the forces involved, that there was no mechanism for relaxation in the sand. Therefore no change of force should be expected with increases of speed -- at least to 15.09 ft/min -- and this is borne out in Table 17 and Figure 44. The depth was

TABLE 17

FORCE RELATED TO SPEED CHANGES

Speed, ft/min	No. Runs	Average Force	Tolerance, s
1.68	8	506	46
2.50	8	512	36
3.27	4	541	3
5.67	8	604	33
9.79	4	527	23
15.09	3	549	21

kept constant at 18 inches and the model used was number one.

To determine if, within the scope of the experiment, dynamic effects could be identified, a comparison with fluids is made and Bernoulli's pressure equation, $P_s = \frac{1}{2}\rho v^2 + P_o$, is evaluated for some representative velocities. P_o is ignored because it represents a static effect; the area is considered and P is tabularized as F, the force on the model.

TABLE 18

POSSIBLE DYNAMIC FORCES

V, ft/sec (ft/min)	v^2	F, pounds
0.1 (6)	0.01	0.001
1.0 (60)	1.00	0.117
10.0 (600)	100.00	11.72

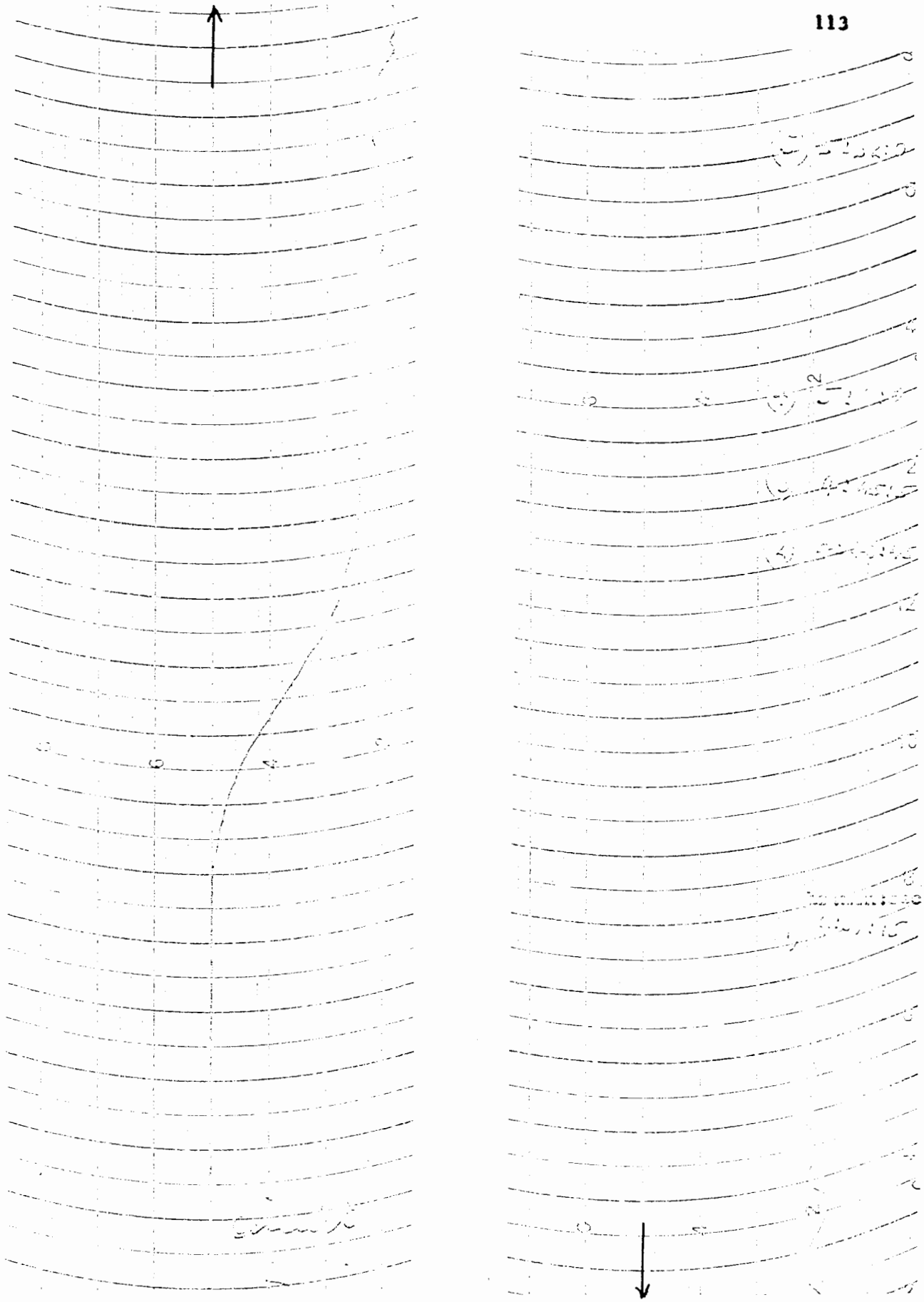

Figure 43: Portion of Recorder Chart Showing Strain Output for Run When Model was Held in the Sand

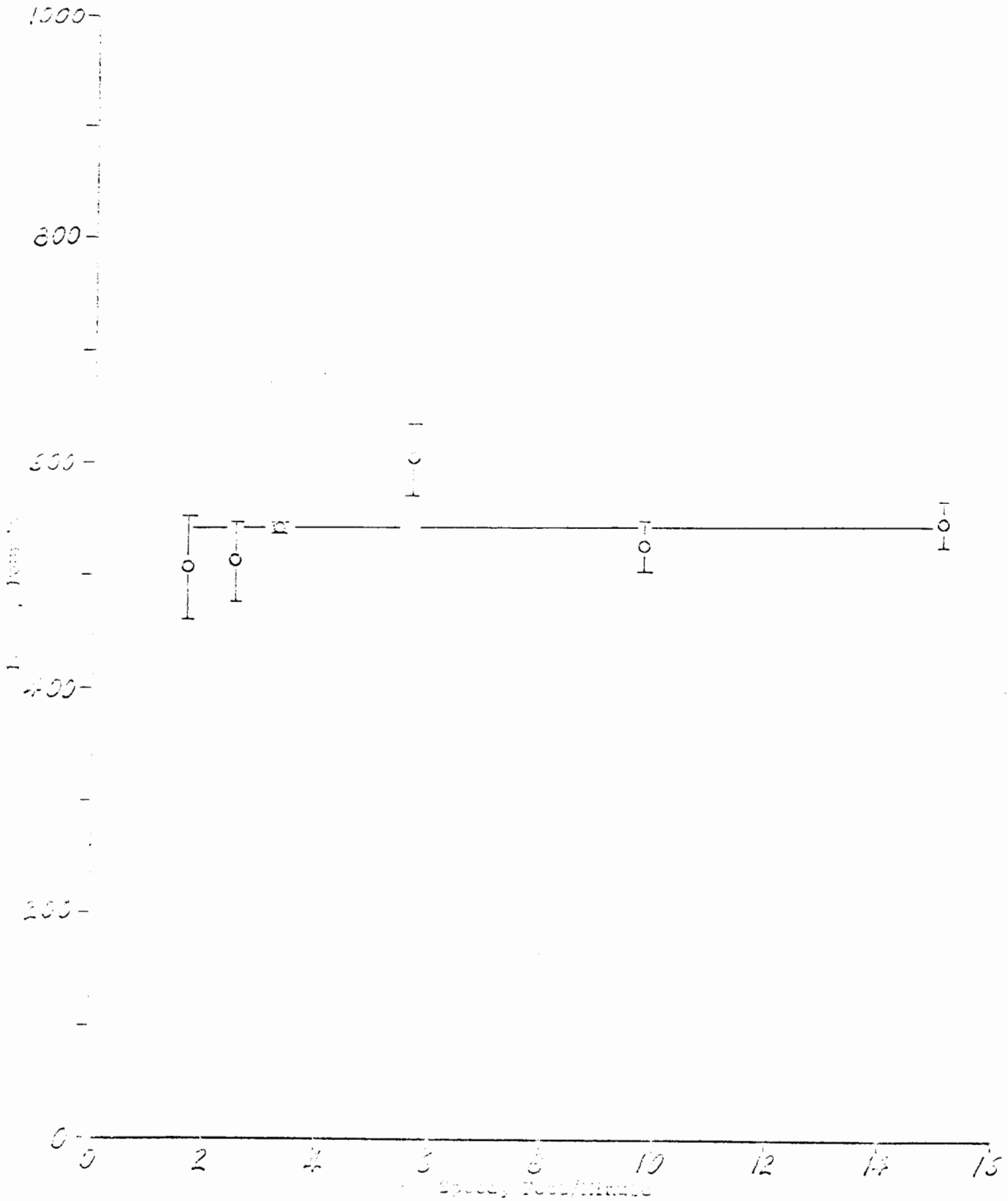

Figure 4.1 Torque Versus Speed

This would lead to the supposition that the equipment was incapable of the speeds necessary to achieve recognizable dynamic forces.

Pressure and Boundary Effects

General: In order to make meaningful conclusions about the relation of force to the model parameters it is necessary to understand something of the mechanism of failure within the granular medium as the model passes through. To this end, two different types of test were made: pressure determinations within the sand and the effect of false walls on the force levels. Both these tests are as important qualitatively as they are quantitatively. Hence a picture of a failure surface should be derived from these experiments.

With only one pressure gauge, the measurement of pressures was done over a series of runs, therefore it is not expected, because of the difficulty in keeping the sand homogenous, to have an uniform picture of the failure surface. Nevertheless, a good approximation should be forthcoming.

Normal Pressure, Measurement: The first significant measurements of pressure were made with the SP gauge set so as to measure pressures normal to the direction of model travel. As with all experimentation, the methods used evolved from trial and error procedures. Nonetheless, the ultimate findings which are herein recorded were surprisingly consistent.

Four objects were used to generate pressures -- an one-inch diameter, eleven-inch long vertical rod; model one at 12 inches, at 18 inches, and at 24 inches -- and for each the gauge was placed at sufficient points to obtain a contour plot of equal pressures within the sand. Each point was obtained from a single run and therefore there are some inconsistencies due to the lack of total homogeneity. Fortuitously, these are small. With symmetry of both model and tank, symmetry of pressure was assumed and the readings were taken

at one side only. It might be mentioned here that peak load always coincided with the model, not its support, passing the gauge. The method of taking the readings has already been described, so the information obtained is now set down in Tables 19, 20, 21, and 22. It must be remembered that the load pressures constitute a pressure change from the static state and it is possible to have a negative change; this does not mean the pressure drops below zero. The reported load pressures are the difference between the peak and static pressures.

An extensive plot of the model at 12 inches was not made because this was not a greatly used depth. The pressure was recorded near the wall of the tank simply as a control check to see that failure was occuring within the medium and not at the walls.

Table 21 for 18 inches and Table 22 for 24 inches represent the most extensive work and also include a measure of the static pressure before the run.

Although there is wide scatter in the values of the static pressure, it can be seen that they most closely fit the theoretical values of the active earth pressures. This must be so because the greatest pressure on the sand, before the experiment begins, is gravity acting in the vertical direction, and thus the horizontal component of pressure will be determined by the active earth pressure coefficient. A plot of the values of the measured horizontal pressures against depth, Figure 45, is included to show this correspondence. The plot also contains the theoretical line of active earth pressures.

To get more accurate values of the static pressure, since at low pressures the gauge output is influenced by the means of mounting and by residual pressures imparted during the burying process, the equations of pressure are used because they are based on more accurately determined constants. The

TABLE 19

POSITION AND VALUE OF PRESSURES, 11-INCH ROD

Run	Depth, inches	Distance from Wall, inches	Load, pressure lbs/in^2
1	9.0	2.0	-0.073
2	7.5	2.5	0.231
3	6.0	2.8	0.111
4	9.8	5.9	-0.095
5	7.3	5.5	0.126
6	5.9	5.8	0.282
7	8.5	8.0	0.133
8	6.0	8.0	0.250
9	4.3	8.0	0.163
10	9.5	12.5	0.472
11	7.1	12.3	0.630
12	6.0	12.0	0.481
13	5.0	1.6	0.059
14	3.8	1.6	0.105
15	12.5	12.5	0.422
16	14.4	12.5	--
17	14.4	12.5	-0.051

TABLE 20

POSITION AND VALUE OF PRESSURES, MODEL ONE AT 12 INCHES

Run	Depth, inches	Distance from Wall, inches	Load, pressure lbs/in^2
18	13.8	1.8	0.029
19	12.3	1.8	0.180
20	10.5	1.9	0.084
21	7.6	1.9	0.076
22	6.4	2.0	0.173
23	4.6	2.0	0.105

TABLE 21

POSITION AND VALUE OF PRESSURES, MODEL ONE AT 18 INCHES

Run	Depth, inches	Distance from Wall, inches	Static Pressure, lbs/in^2	Load pressure, lbs/in^2
46	19.5	2.3	0.333	0.329
47	16.5	2.1	0.224	0.349
48	21.3	6.9	*1.855	1.790
49	17.9	6.9	*-0.204	1.455
50	15.3	6.8	0.212	1.455
51	19.9	12.6	0.142	3.680
52	17.0	12.5	0.114	5.030
53	13.4	1.5	0.016	0.484
54	+			
55	14.4	6.3	0.610	1.900
56	11.0	6.1	0.185	2.130
57	14.4	12.5	0.381	3.135
58	12.5	12.4	0.091	3.540
59	9.3	1.9	0.078	0.480
60	5.5	1.6	0.086	0.231
61	8.5	6.5	0.141	0.565
62	5.4	6.3	0.086	0.376
63	10.8	11.6	0.055	0.687
64	5.5	11.5	0.079	0.574

*The value of the static pressure is not always to be trusted.
+A wire slipped from its connection at a vital moment; the run was repeated.

TABLE 22

POSITION AND VALUE OF PRESSURES, MODEL ONE AT 24 INCHES

Run	Depth, inches	Distance from Wall, inches	Static Pressure, lbs/in^2	Load pressure, lbs/in^2
24	22.5	4.5	0.228	0.313
25	19.3	4.4	0.163	0.790
26	16.3	4.4	0.023	1.478
27	23.4	8.3	0.271	1.332
28	18.0	8.0	0.251	1.819
29	15.5	8.0	0.221	1.929
30	25.0	12.5	0.155	8.100
31	21.0	12.0	0.189	6.210
32	18.0	11.8	0.104	4.445
33	14.8	1.8	0.309	2.062
34	11.8	1.8	0.251	1.880
35	13.3	6.6	0.232	1.102
36	9.9	6.6	0.120	0.611
37	*6.8	6.3	0.023	0.305
38	8.5	1.5	0.116	0.386
39	13.9	11.9	0.290	1.264
40	10.3	11.6	0.067	0.998
41	*6.3	11.4	0.067	0.371
42	*4.8	2.3	0.051	0.386
43	*2.8	2.0	0.066	0.301
44	*3.1	7.0	0.093	0.163
45	*3.6	12.3	0.074	0.167

*The load pressures at this depth are probably due to the influence of the probe rather than the model.

TABLE 23

DEPTH CORRESPONDING TO PRESSURE

P, lbs/in^2	d_a, inches	d_h, inches	d_p, inches
0.1	5.44	1.78	0.58
0.2	10.88	3.56	1.16
0.3	16.32	5.34	1.74
0.4	21.76	7.12	2.32
0.5	27.20	8.90	2.91
0.6	32.64	10.68	3.49
0.7	38.08	12.46	4.07
0.8	43.52	14.24	4.65
0.9	48.96	16.02	5.23
1.0	54.40	17.80	5.81
2.0	108.8	35.60	11.62
3.0	163.2	53.40	17.43
4.0	217.6	71.20	23.24
5.0	272.0	89.00	29.05
6.0	326.4	106.8	34.86
7.0	380.8	124.6	40.67
8.0	435.2	142.4	46.48
9.0	489.6	160.2	52.29
10.0	544.0	178.0	58.10

angle of friction, ϕ, is 30.5° for Hatford-Loam Sand; the density, γ, is 1.55 gm/cm^3, in engineering units, 97.0 lbs/ft^3. Table 23 embodies the depths corresponding to the three values of pressure: active, hydrostatic, and passive. It is derived from the formulae $d_a = P/\gamma K_a$, $d_h = P/\gamma$, and $d_p = P/\gamma K_p$, where K_a and K_p are defined in equations (3) and (4) of Section I.

Table 23 is laid out with pressure the independent variable and depth the dependent variable, so that this information can be applied to the plots of load pressure taken from Tables 19, 21, and 22 which are Figures 46, 47, and 48. It can be safely assumed that the material will fail when the load pressure exceeds some value of the static pressure. Thus on each plot of equal pressure contours, a line is drawn which is the locus of intersections of a pressure contour with the equivalent value of static pressure. This line should represent the path along which the material fails.

In theory, when the greater pressure is horizontal, the passive earth pressure determines failure. The lines of failure drawn on the contour plots tend to confirm this. Not only is the passive case the only line that fits on all of these plots, but it agrees the best with further evidence.

Before producing this confirmatory evidence, it is best to state here what checks, controls, and hence possible errors were used in these pressure measurements. An X-Y plotter was used to confirm the readings of the valve voltmeter and to produce curves of pressure versus model position. The first check was for response. The plotter responds more slowly than the meter so it was assumed that if the readings produced on the two instruments for the same peak load were identical, than the meter was sufficiently fast to give a true reading. This, in fact, was the result. The second check was visual but still persuasive; peak load occurred when the probe was still

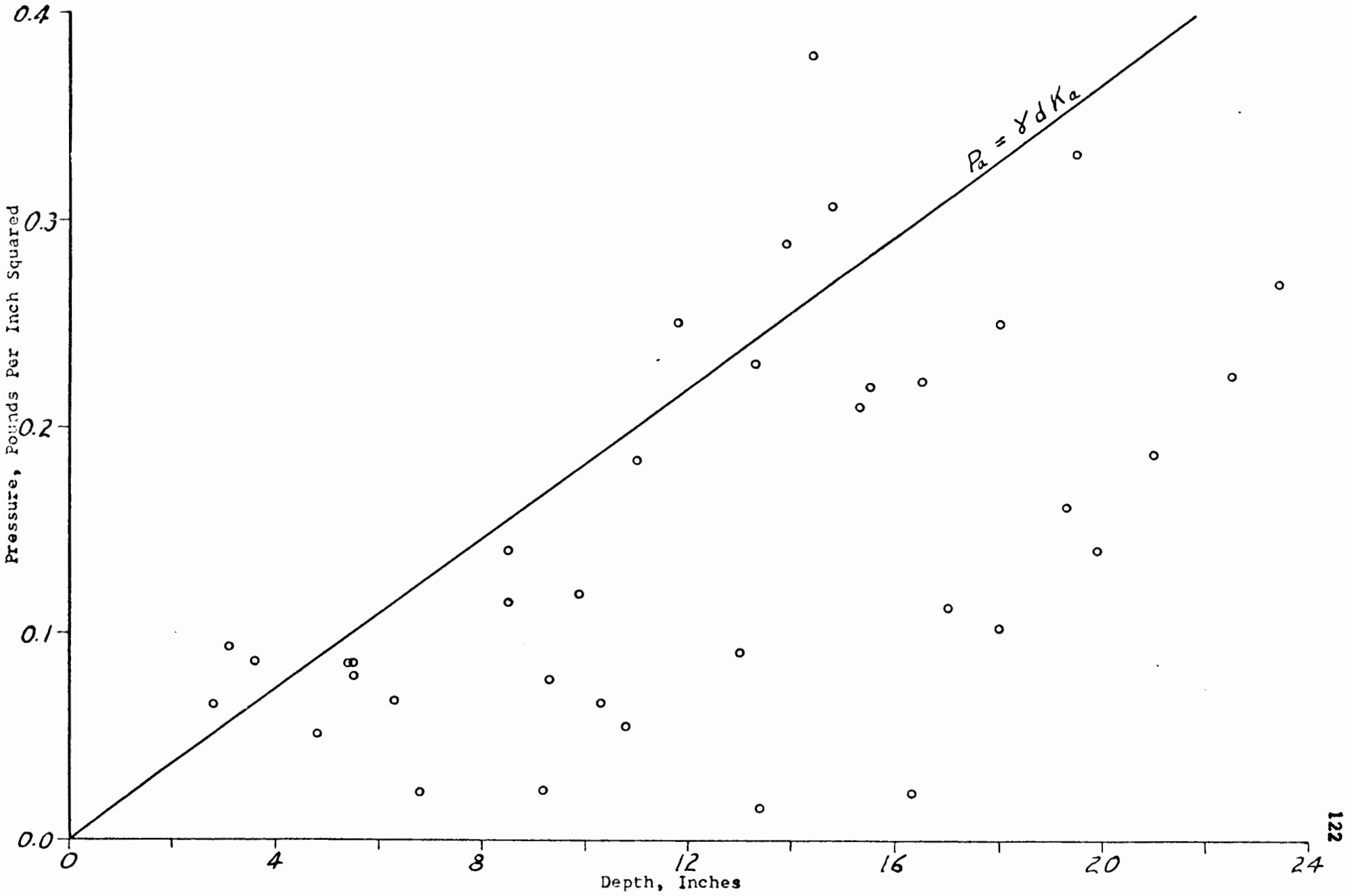

Figure 45: Static Pressures versus Depth

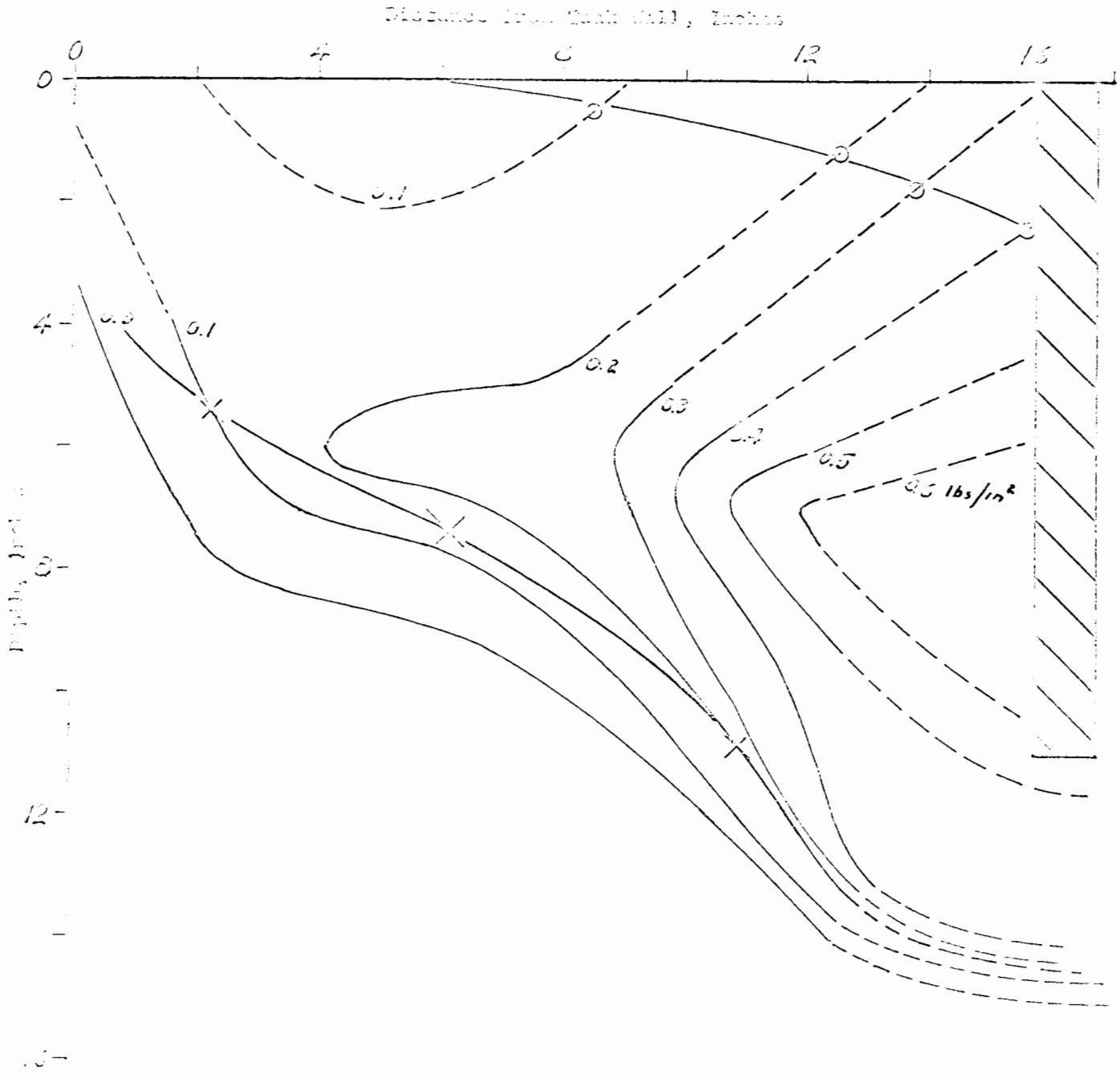

Figure 46: Contour Plot of Equal Pressures: 11-Inch Rod; o = Passive Intersection; x = Active Intersection

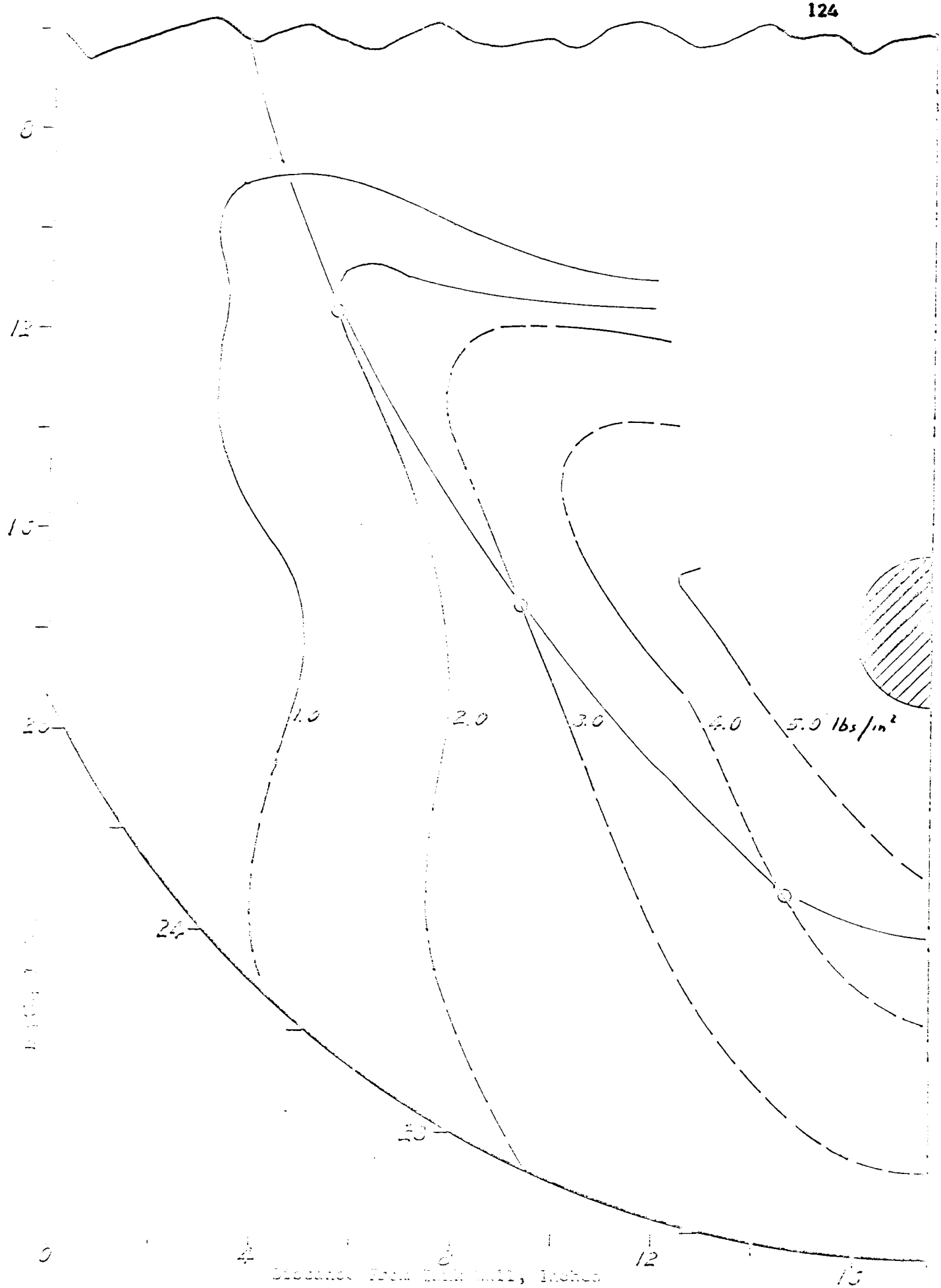

Figure 47: Contour Plot of Equal Pressures: Model One at 16 Inches

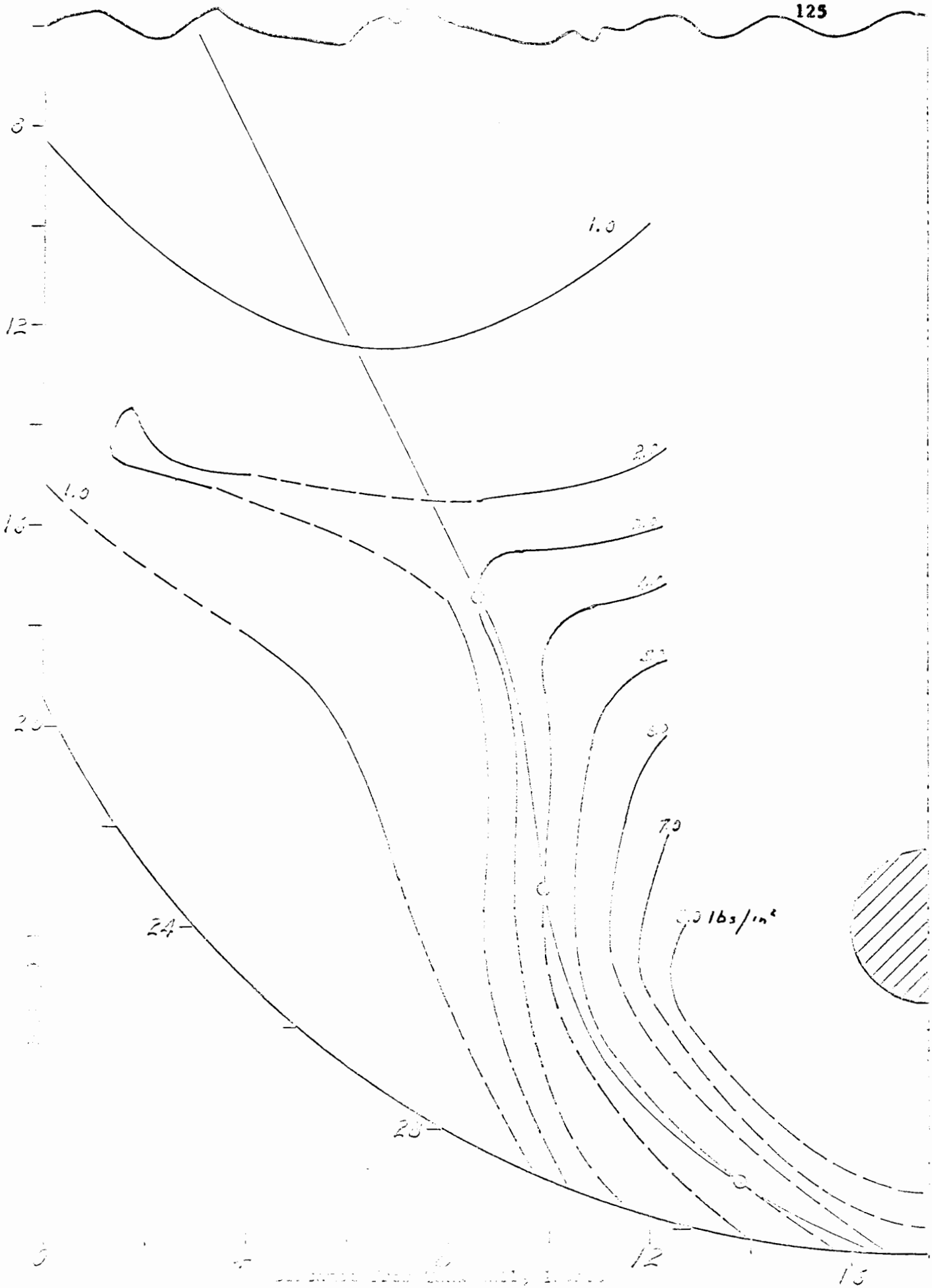
8
12
16
20
24
1.0
2.0
1.0
2.0
3.0
4.0
5.0
6.0
7.0
8.0 lbs/in²
8
12
16

two or three inches away from the gauge. Implicitly, the forward suspended model generated the greatest pressure showing that failure was caused by the model and not the probe. A good check is thus also provided on the probe design.

The third check was in regard to a phenomenon peculiar to this tank. As the trolley passed over the tank, its weight would cause the walls to separate slightly and the static pressure would lower. When the run was complete and the trolley returned, the walls would then contract and raise the pressure to a point higher than the initial pressure. However, the return was of no consequence and all readings were taken from the initial point. Several runs were made to determine the magnitude of this aberration and the results put in Table 24. The values that would be experienced for the gauge position if the model were present are also included.

TABLE 24

PRESSURE LOSS FROM TANK WALL MOTION

Run	Depth, Inches	Distance from Wall, Inches	A: Pressure Drop, lbs/in^2, with no Model	B: Expected Pressure, lbs/in^2	% Loss (A/B x 100)
65	11.8	6.8	-0.177	2.2	8.0
68	19.9	6.4	-0.224	1.8	12.4
72	15.5	6.5	-0.087	1.5	5.8

Although these percentages are fairly high it was decided to report the load pressures as a difference of the peak and of the initial static pressures rather than attempt to fit in this variation. Since it cannot be determined what would happen if the tank were rigid, any attempt at calibrating the pressure data would probably lead to more untraceable errors. Sample plots of the X-Y recorder are given in Figure 49; one plot is of the pressure

with the model at 18 inches, the other is of the trolley passing with no model and the gauge in the same position.

The fourth and final check, done for itself and as a further check on the second, was to measure the pressure with only the upper-beam of the probe in place. This, it can be recalled, has a length of 15½ inches from bottom of locking nut to end. A table, such as before, sets out the measured pressures and the pressures to be expected if the model at 18 inches were passing.

TABLE 25

PRESSURE FROM UPPER-BEAM OF PROBE

Run	Depth, inches	Distance from Wall, inches	Beam Pressure, lbs/in^2	Expected Pressure, lbs/in^2
66	11.8	6.8	0.576	2.2
67	5.8	6.5	0.471	0.4
69	19.9	6.4	0.838	1.8
71	15.5	6.5	0.701	1.5

The obvious conclusion to be drawn from Table 25 is that pressures measured above 6 or 7 inches of depth will be related more to the probe than the model. This is followed in the pressure contour plots and no contours are drawn at points less than six inches of depth.

In producing the contour plots, the rules of contouring are followed so that smooth contours, rather than ones that take in outlying points, are drawn.

Normal Pressure, False Walls: If the failure, as it is conjectured, occurs entirely within the tank it should be possible to use a narrower tank and obtain the same forces on the model. Not having a smaller tank, it was decided to bury stiff, 1/8-inch thick dural plates in the sand as false

the model was number one and the depth 18".
walls. Three positions were used with two sets of plates. The assumption was that at some point in the placing of the plates they would intersect the failure surface; that is form a new failure surface between the sand and the plate which bounds a smaller amount of failed material, causing a diminished force on the model. The first set of plates, 21 inches by 24 inches were buried parallel to the direction of travel with the long dimension horizontal, the top edge flush with the surface, and the leading edge 60 inches from the start of the level sand. This set of plates was first buried 6 1/8 inches (measured to the surface of the plate nearest the model) from the tank wall, with 23½ inches of space between. Secondly, they were placed 12 1/8 inches from the side with 11½ inches of space betwee. The third position was identical to the second except that a second set of plates that extended (29.7 inches) to the floor of the tank was used. Figure 50 shows this set of plates half buried. Inasmuch as the test was meant only to be a qualitative check, it will be simply stated that the first two positions caused no difference to the force on the model, but that the third caused the force to lower by about 21 percent. Figure 51 shows the chart that recorded this run. Thus there is some vindication for the selection of tank size and for the theory that failure occurs wholly within the sand. Quantitatively, it can be said from this particular experiment only that there lies a point somewhere between 6 and 12 inches from the wall where the introduction of a vertical failure plane, rather than the natural sloped one, causes a reduction of force on the model. No doubt this is because the bounded material is smaller in volume.

Normal Pressure, Surface Patterns: One more interesting, but wholly qualitative observation is the patterns that form on the surface of the

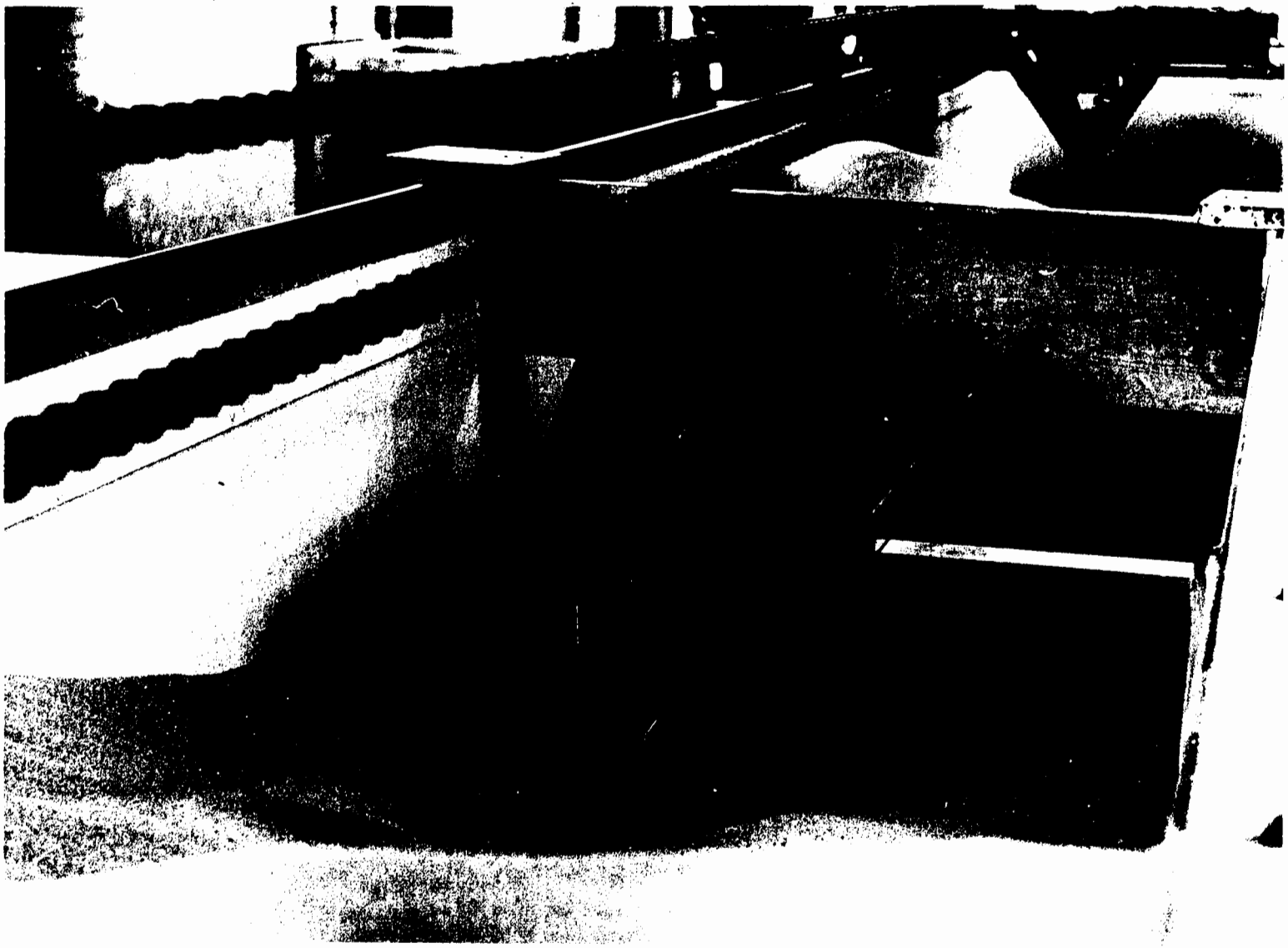

Figure 50: Half-Buried False Walls

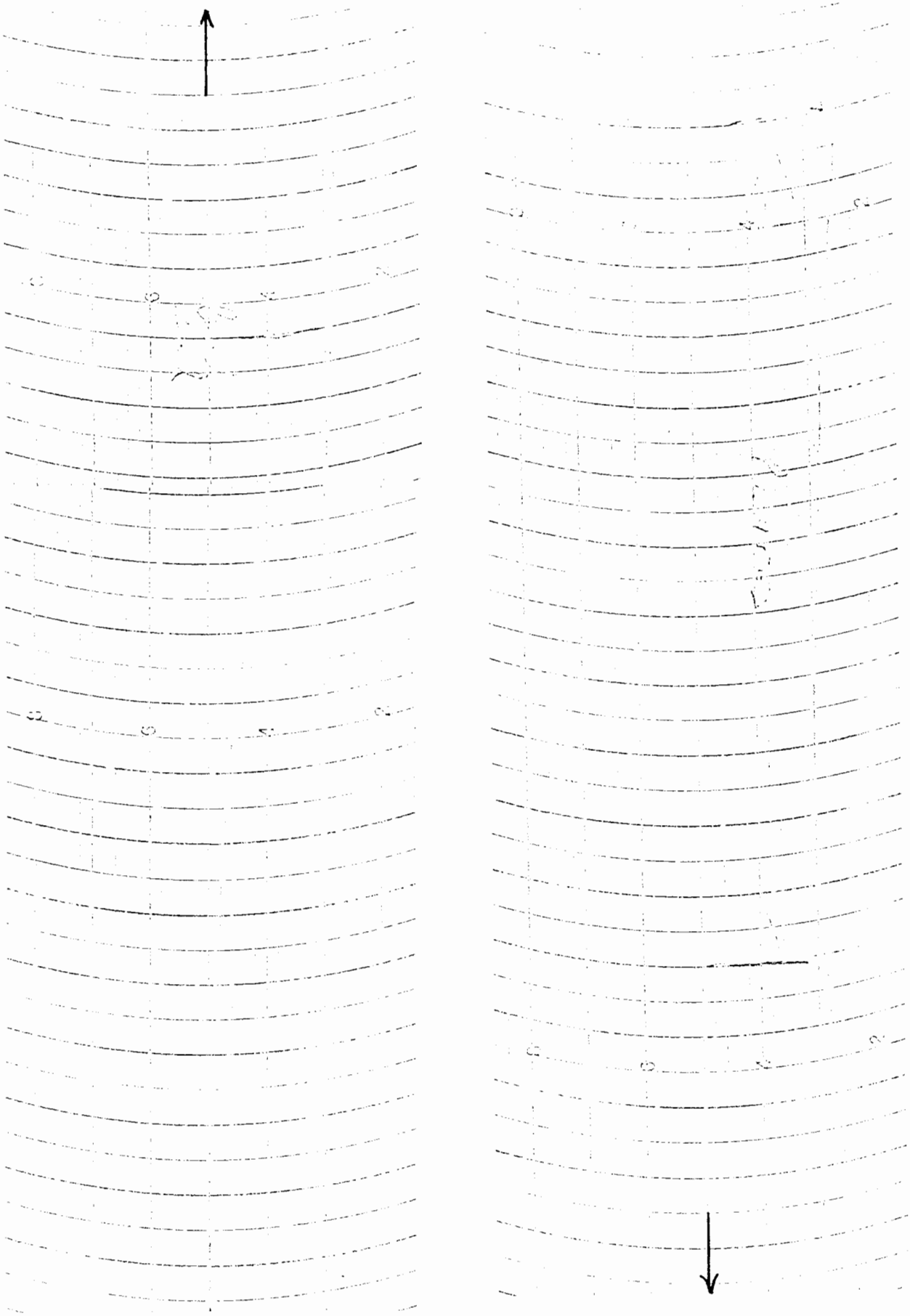

Figure 51: Portion of Recorder Chart Showing Strain Output when Model was Run Between False Walls

sand after a run. They were noticed after the template for leveling the sand was used. With a perfectly smooth surface, Figure 52, to begin with it became easy to see any disruption of the surface. Presumably, the edge of the pattern represented the extension of the failure surface to the upper free surface.

The patterns did not begin, or if they began, did not reach their full dimensions until the model had travelled 36 inches into the sand (all axial distances are measured from the start of the level sand, not from where the model first enters the sand). The patterns were never strictly uniform, reflecting the nonhomogeneous character of the sand, but they were of approximately constant width. With the model at 12 inches of depth, the disturbance on the surface would extend 10 to 11 inches from the line of travel. With the model at 15 inches the patterns extended 11 to 12 inches from the centerline. At 18 inches and deeper, the patterns would extend to the wall of the tank. At 18 inches depth the patterns extend 24 inches in front of the probe. Photographs best display this disturbance, hence Figures 53 and 54 are included to show the patterns created at 18 inches; Figures 55 and 56 show the patterns at 21 and 24 inches respectively. Figure 57 shows the patterns created when the plates were in their third position. The upper beam of the probe creates similar patterns on its own.

Axial Pressure: Having established a line of failure in the direction normal to the travel of the model, it was desired to learn something of the failure in the line of travel. To this end, the gauge was buried at a point directly in the path of the model perpendicular to it and 60 inches from the start of the level sand. When measuring normal pressure, it was necessary not only to determine the slip plane but to establish that the tank was indeed large enough to



Figure 52: Smooth Sand Surface



Figure 53: Disturbance on Sand Surface After Model One at 18 Inches Passed



Figure 54: Disturbance on Sand Surface
After Model One at 18 inches Passed

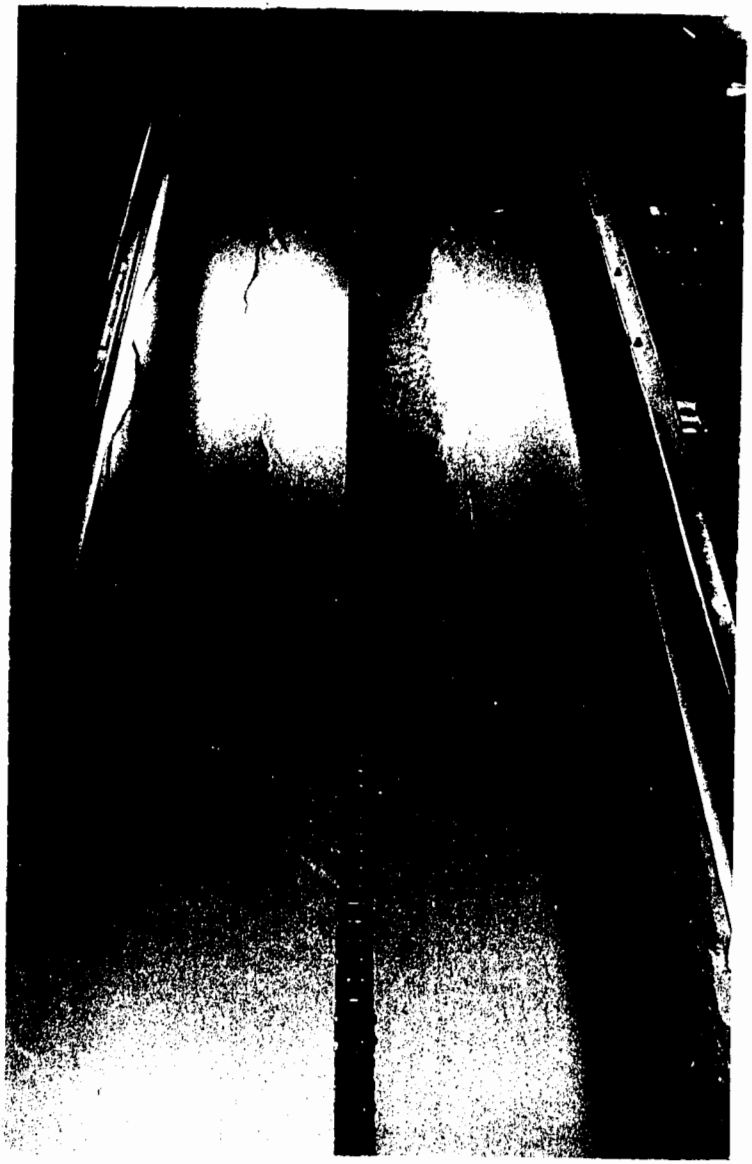

Figure 55: Disturbance on Sand Surface Afte
Model One at 21 inches Passed



Figure 56: Disturbance on Sand Surface After Model One at 24 Inches Passed



Figure 57: Disturbance on Sand Surface After Model One at 18 Inches Passed between the False Walls

accomodate the model and the accompanying failure it causes within the sand. The purpose of measuring the axial pressure was solely to determine the manner in which the sand failed. It was postulated from evidence obtained from the earlier pressure measurements and from the surface patterns that the portion of sand that moved, that is failed, did so in a wedge. The shape of this wedge, Figure 58, is an inverted pyramid with rectangular base. The largest cross-section is a triangle with its dimensions determined by the failure surface normal to the model and its direction of travel. The photographic evidence shows that the leading line of the wedge is straight and thus the assumption that the base is rectangular.

The pressure gauge output was led into the X-Y plotter; the model was number one; the depth 18 inches; and the speed 3.30 feet per minute. Careful positioning was maintained so that it was easily possible to measure, on the surface, the distance that the model stopped from the gauge. The following table gives the result of these measurements.

TABLE 26

MEASURED AXIAL PRESSURE VERSUS DEPTH

Gauge Depth, inches	Calculated Pressure, lbs/in^2			Peak Pressure, lbs/in^2
	P_a	P_h	P_p	
5.4	0.099	0.302	0.925	0.399
8.6	0.159	0.485	1.484	0.832
13.0	0.239	0.730	2.238	1.810
18.3	0.336	1.025	3.140	*5.01
21.5	0.396	1.208	3.700	*3.30

*still rising when model stopped

Figure 59 is a copy of the pressure output below the model and Figure 60 is a copy of the pressure output above the model. From Figure 60 it can clearly be seen that failure occurs, when the pressure drops, before the

model reaches the gauge. A simple plot, Figure 61, showing the point of failure, in relation to the model, of the sand at various depths indicates that the wedge assumption is correct. Further, the angle of this failure surface is near to that for the passive slipline, the slipline that is correct for the situation of principal pressure horizontal. These points of failure lie on a series of lines that form angles from 33 to 47 degrees with the horizontal. The theoretical passive line, $45^{\circ} - \phi/2$, is 29.7° to the horizontal. There is no way of telling what influence the gauge position had on the failure surface. By its presence it may have caused an unnatural observation of the faiure line; presumably the bulk of the gauge and its support were responsible for the apparent steepening of the line.

Examination of an X-Y plot of the normal pressures, Figures 49 and 52, as the model passes indicates that there is a rear slope, other than vertical, to the failed wedge. The pressure drops on a line that is steeper than the one on which it rises, however, it does descend on a slope. Since there is no way of repeating the axial measurements that were done to obtain the forward slope for the trailing slope, inferences are drawn from Figure 62 and from four other plots, not shown, that were made by placing the gauge at different positions. It is assumed, from the steeper rear slope, that the rear surface of the wedge is inclined to the horizontal by the active angle, $45^{\circ} + \phi/2 = 60.3^{\circ}$. This surface is incorporated in Figure 58.

The volume of the pyramid is now easily obtained. From Figure 47 and Figure 61, the dimensions of the base, 34 inches long by 29 inches wide, are obtained, and the depth is 18 inches. From V = 1/3 Base times Height, the volume is 3.43 cubic feet and the weight (the density is 97.0 lbs/ft^3) is 333 pounds.

With an idealized failure wedge established it is possible to find the forces on this wedge. They are resolved directly in the principal planes and therefore no shear is present. Further, the pressures, and consequently the forces, are dependent only upon the depth of model and thus speed of travel has no effect on these forces.

In determining the forces, it is seen that those acting on the sides of the wedge counteract each other and do not need to be found. Thus the forces on the forward and rear surfaces of the wedge are to be determined.

The center of pressure on an inverted triangle is found by

$$\bar{x} = \int xP\,dA / \int P\,dA$$

where P, at a point x, is $\gamma(h - x)$, and $dA = mx\,dx$.

$$\bar{x} = \tfrac{1}{3}h.$$

The hydrostatic, or vertical, value of the pressure acts at this center; considering the area of the triangle the force is then found

$$F = \tfrac{1}{2}\gamma hA.$$

Multiplying the force on the forward surface, 220 pounds, by the passive earth pressure coefficient, and that on the rear surface, 152 pounds, by the active coefficient, gives the components of horizontal force. Subtracting the rear force from the forward one, the total limiting force on the idealized wedge is 624 pounds. This is only eight percent different from the measured force, 576 pounds, on model one at 18 inches, which was the situation from which this wedge idealization was made. Although, in the above analysis, it has been assumed that the region of failure was a pyramid with its vertex at the model, the fact that failing pressures were found beneath the model (Figure 47) suggests that the failure surface should be curved as is normally the case for passive plastic failure. This line is shown on Figure 58 as a suggestion for the more complicated surface.

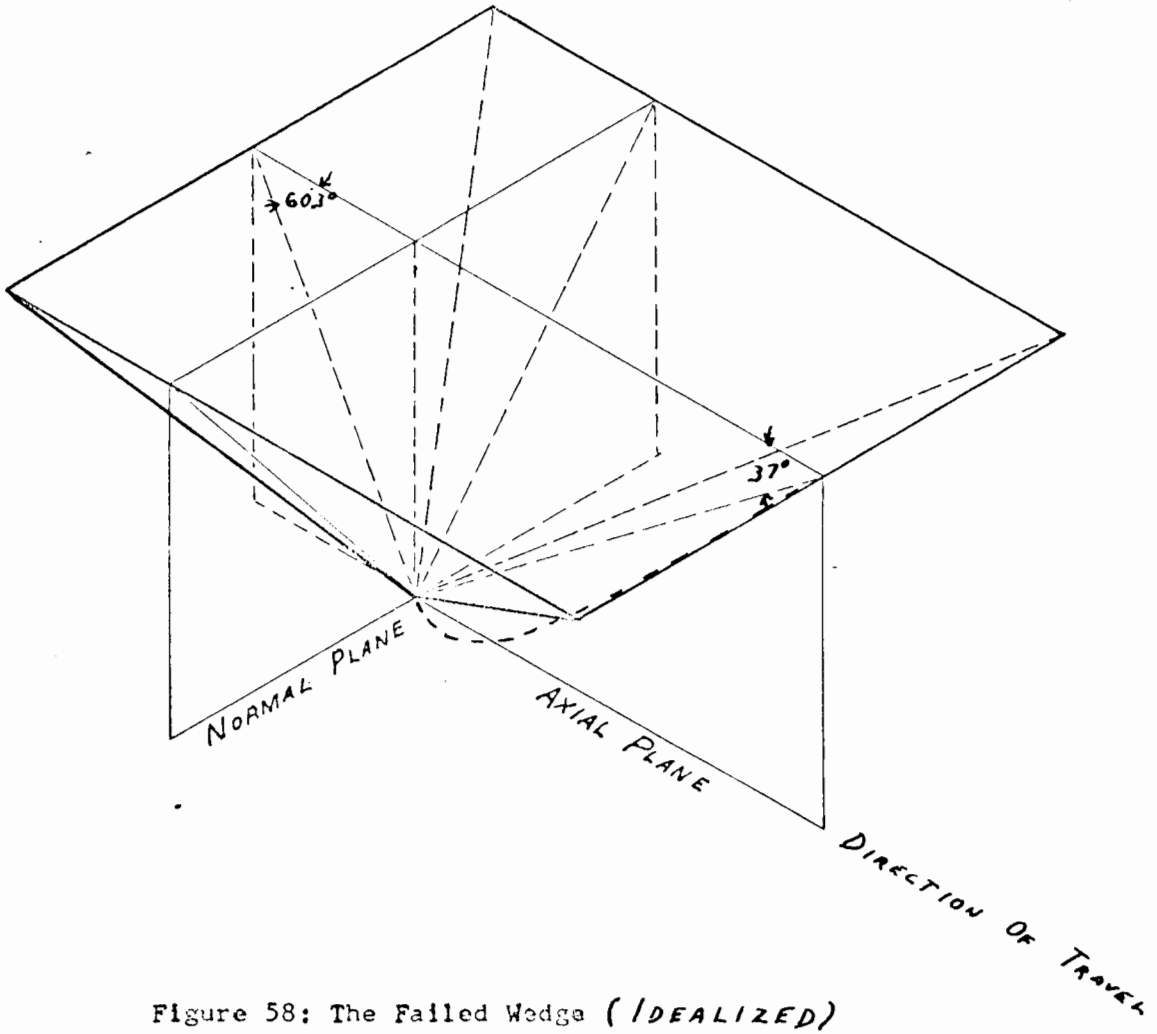

Figure 58: The Failed Wedge (IDEALIZED)

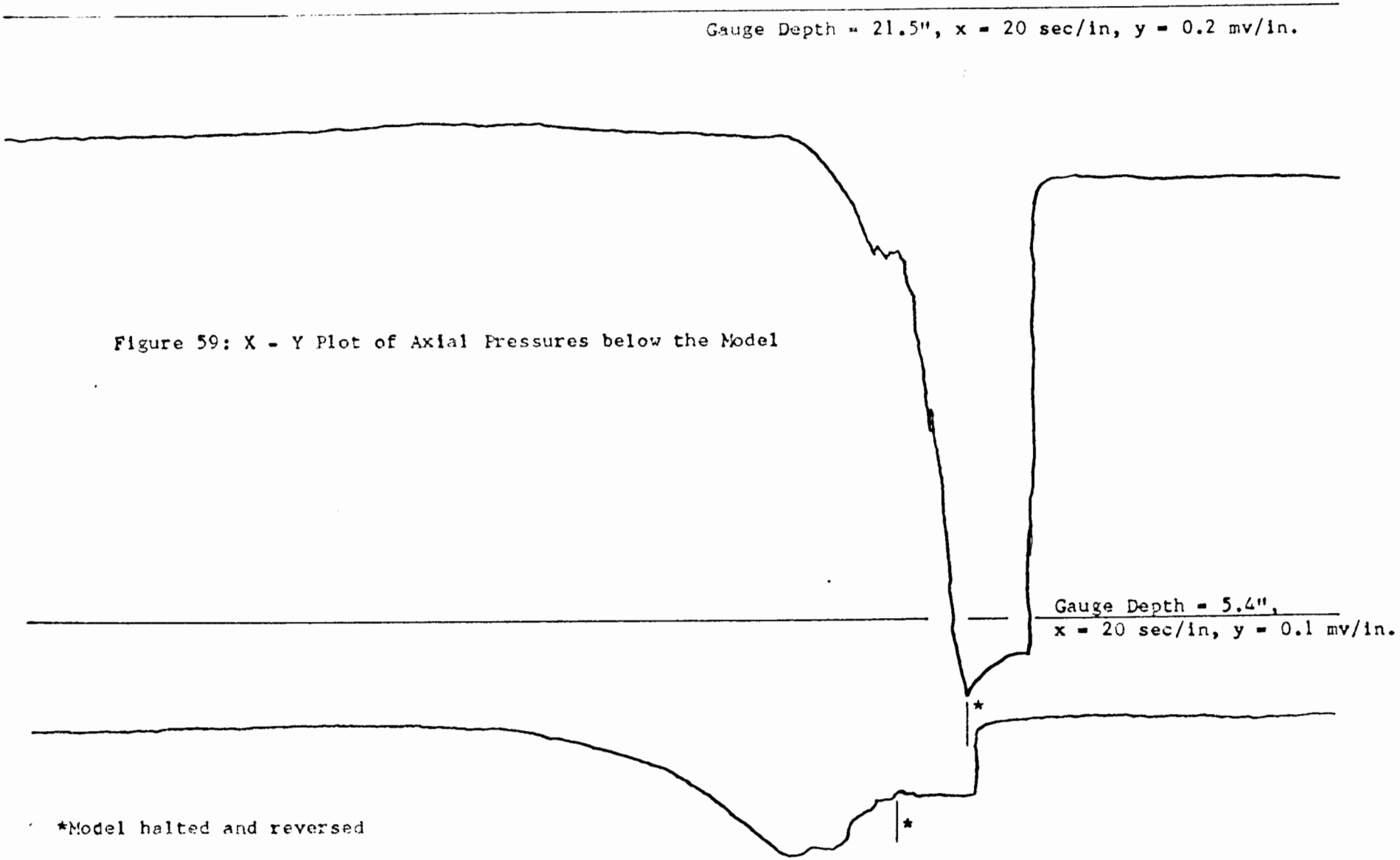

Figure 59: X - Y Plot of Axial Pressures below the Model

Figure 60: X - Y Plot of Axial Pressures above the Model

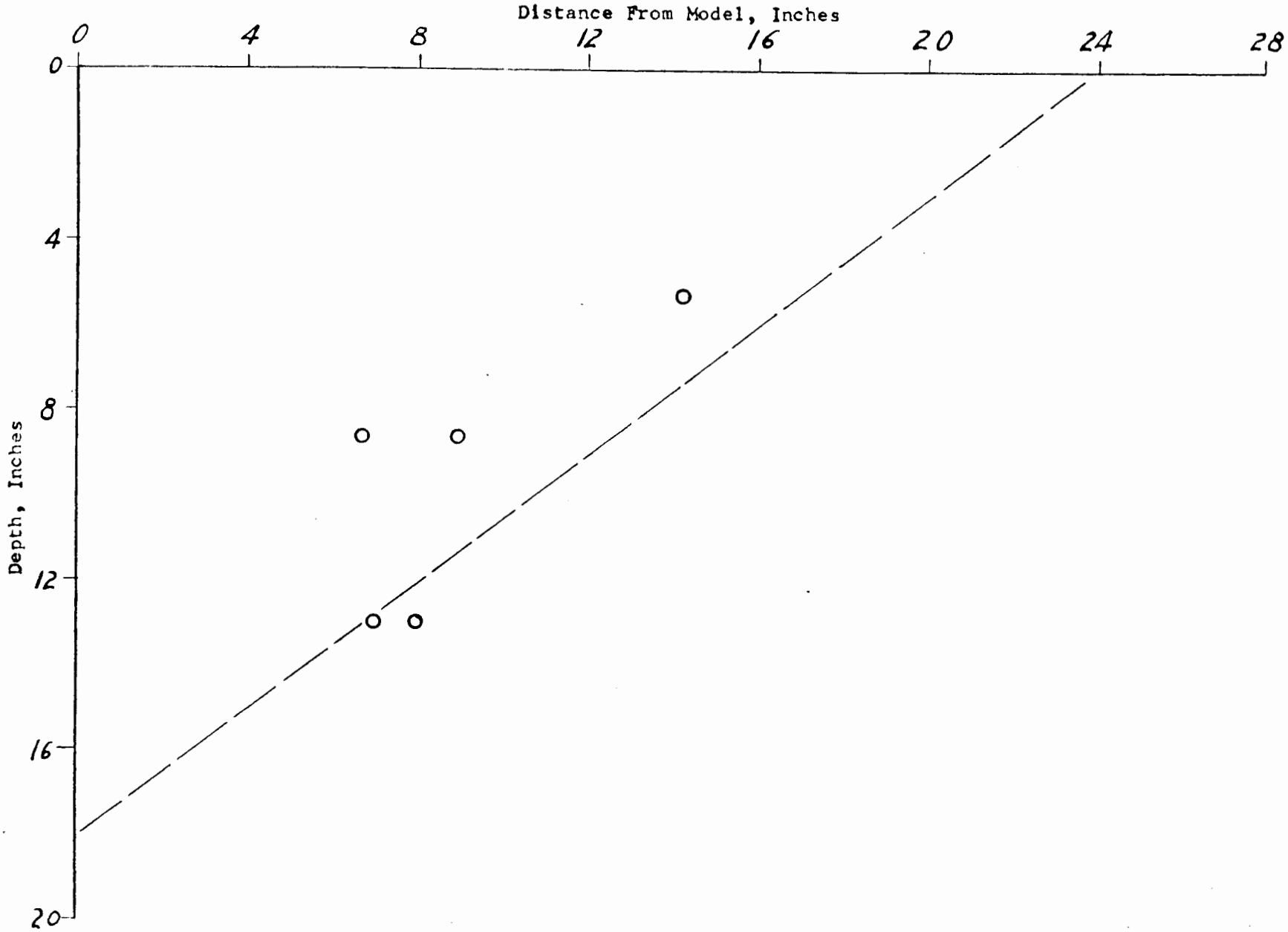

Figure 61: Position of the Line of Failure in the Axial Direction

Gauge Depth = 12", Gauge Distance from Wall = 13", x = 20 sec/in, y = 0.1 mv/in.

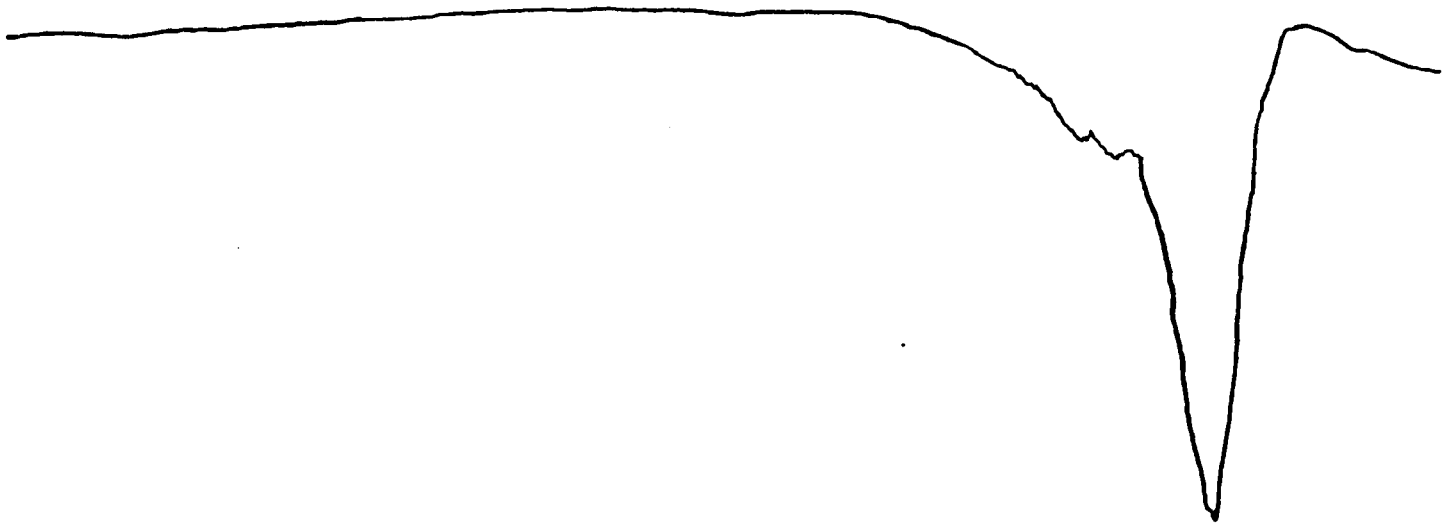

Figure 62: X - Y Plot of Normal Pressure as the Model Passes Completely

Compressive Effects: Several other pertinent observations were gathered during the course of experimentation. The first is that the force on the model can be affected by the degree of compaction of the sand. If a particular section has been disturbed, such as by burying the false walls and then removing them, the force on the model will decrease; conversely, if a particular section has been well compacted, such as by extensive use of the concrete vibrator, the force will go up. The second is if the model passes completely through the zone where it halted in a previous run, the force will go up as it passes through this zone. In both cases, the total change could be as much as one third of the expected force. A third observation, relevant to the first, is that the patterns on the sand surface became more extensive at any point where the force had gone up. Thus if the model passes through a zone of more compact sand the force on the model goes up and more sand is disturbed at the surface.

Dynamic Failure: The failure at any instant is described but no mention has been made of its continuing mode. As in Nelson and Selig's experiment, it takes an oscillating form as pressure builds up and then causes failure of successive blocks of sand. This phenomenon is easily seen from the trace of the pressure output of an early run, Figure 63. This section of a chart recording shows a trace from a strain gauge mounted so as to measure strain in a vertical plane. Unfortunately, the oscillations are so great that no meaningful measurements can be made from this trace. Therefore opposite gauges were wired in series to form pairs so as to eliminate, on the trace, the oscillations. Thus, the recording equipment produced a record of the compressional forces without interference from forces caused by flexure of the mount.

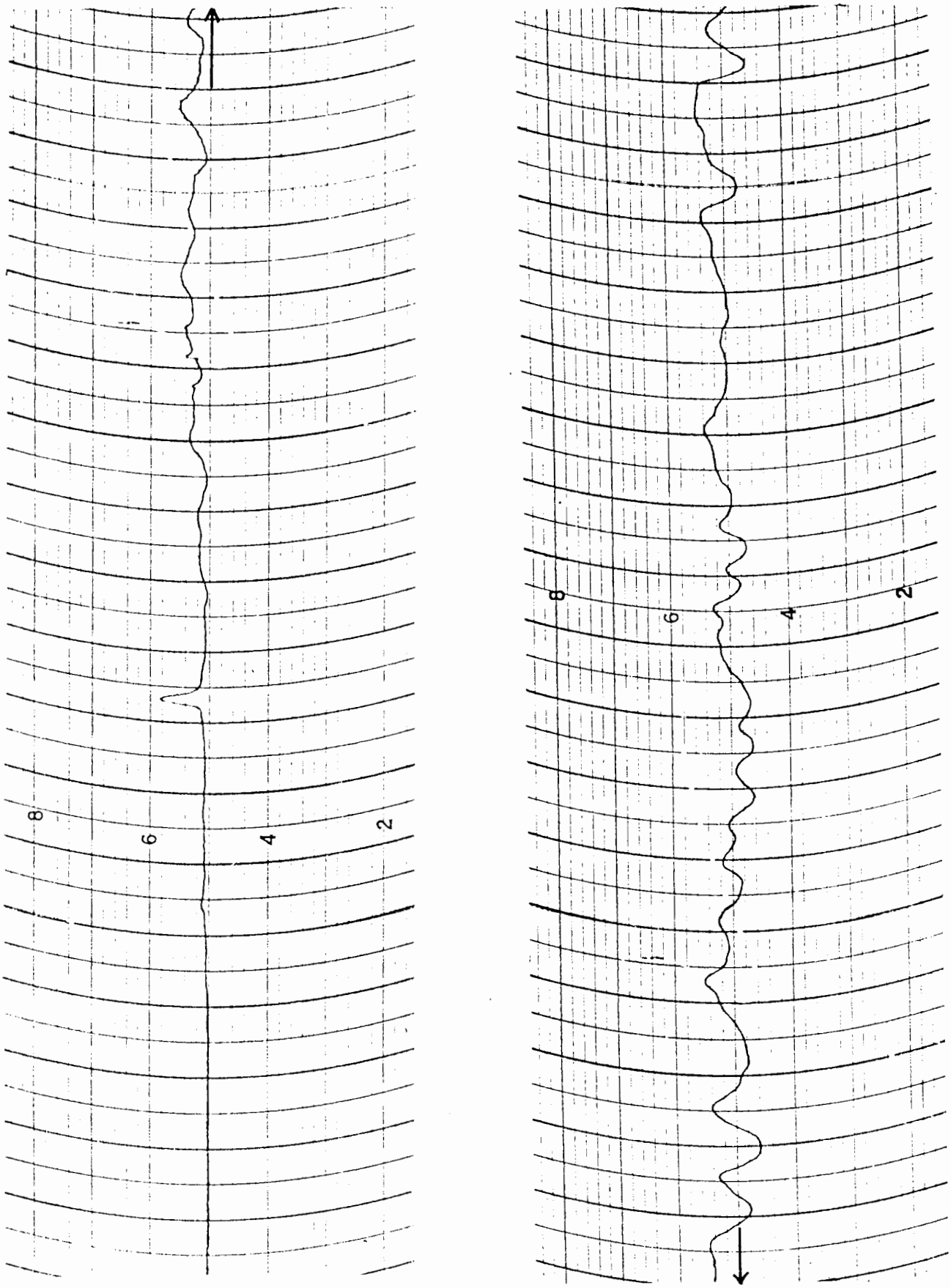

Figure 63: Portion of Recorder Chart Showing Strain Output of Successive Shear Failure

Trolley Draft

Although the measurement of total trolley draft was not necessary for the relating of the force on the model to the various parameters of the experiment, it was measured and will be reported here. The purpose of the measurement was to check the efficiency of the gearing system and to determine the power delivered to the model.

With the model at 13 inches of depth, hence a model drag of 541 pounds, the total draft varied from 860 pounds to 1075 pounds. Although the gauges were mounted on the eyebolt connecting the trolley to the chain, the value of the chain tension -- approximately 300 - 400 pounds -- is not reported in the value of total draft. The draft due to the rolling friction of the trolley -- it was quite heavily loaded to keep it on the rails -- was about 175 pounds. Hence the efficiency of the system can be gathered from the knowledge that the motor would occasionally stall at the 15.09 ft/min speed.

(15.09 ft/min x 1075 lbs)/(60 sec/min x 550 ft lb/sec/hp) = 0.492 hp. Thus, 33 percent efficiency was obtained from the gearing system driven by an 1½-horsepower motor; it is noted, however, that the efficiency of a worm-gear reduction unit drops with increases of input speed.

Although the system was relatively inefficient, it was ~~tolerated~~ used because it was easily maintained and both cheap and easy to alter.

ERRORS AND ANALYSIS OF RESULTS

Errors

General: As in Section I, it is necessary to state how errors affect the data included in this report. Therefore a section on those errors that can be accounted for because they are systematic, and a section on those errors that can be deduced but not numerically accounted for because they are random is included at this point.

Systematic Errors: The first source of error identified was the most important to the accuracy of the results and, fortunately, the one most easily corrected. This was the output of the strain gauges. Rather than perform tedious observations of the gauge factor, the stated gauge factor was accepted and used. Calibration was provided by comparing the computed output to a known dead load that provided the strain. Variation of the true value of S from that stated was also eliminated by this method.

TABLE 27

CORRECTION FACTORS

Runs	Circuit	Percent Correction
1 - 69	1 and 2 averaged	98.0
70 - 102	1	100.5
	2	105.0
103 - 117	1	99.5
	2	98.6

The lower beam of the probe was demounted and clamped in a vise so that the strain-gauge mount was vertical, and to this model number 5 (no cone) was attached so as to form a base for the dead weight. The output of the strain bridge was led to a valve voltmeter and the bridge was zeroed and calibrated as before. The weights were added and the strain output

recorded. This was done a number of times on each circuit, the readings averaged, the weight calculated and then compared with the actual value. A correction factor was thus obtained. This procedure was done any time the strain-gauge mount was replaced or tampered with. The correction factors in Table 27 were thus obtained. All force results reported here have had the appropriate factor applied and are therefore corrected.

The next error of this type to be identified is in relation to the depth. The pitch of the thread used to hold the upper beam to the probe support is 0.1666 inches; at 18 inches with the force varying with the depth raised to the 2.5 power, the difference of one pitch would mean an error of 2.5 percent. Since the model must face forward, it can be seen how it is possible for the model to be one-half of a pitch above or below 18 inches. Considering this and the possibility of fluctuations in the sand level, a tolerance of $\pm\frac{1}{8}$ inch is included in the reporting of depth.

The force varies linearly with the projected area of the model; hence any variation in the diameter would cause the force to vary by the diameter squared. Therefore all models were turned to within one or two thousandths of an inch of their stated diameter. Upon checking, however, it was found that model number 4 (30°-cone, $1\frac{1}{2}$-inch radius, no cylinder) was outsize and actually measured 3.118 inches across the diameter. Since this aberration was observed, it can be stated that the unknown errors inherent in model diameter size can be no greater than $(1.502/1.500)^2 \times 100$, or less than 0.3 percent.

The model surfaces were all similar, that is polished until no visible scratches remained but still non-reflective. Subsequent experimentation has shown that these precautions were redundant. Nevertheless, it is cer-

tain that no errors could have been introduced from variation of model surface. It might be noted that passage of the model through the sand did not scratch or mar the surface.

Compensating or Random Errors: As was mentioned previously, the sand could not be made entirely homogenous and thus there was variation in both the bulk density and the voids ratio. A bench test shows that the bulk density, γ, can vary from 1.46 gm/cm^3 to 1.57 gm/cm^3. The figure of 1.55 gm/cm^3 has been used in the calculations because it represents the density achieved by intermittent vibration; the upper limit, above, was achieved with a vibration table. In any event, the bench test shows that the value of the bulk density can be varied by 7.0 percent. The density, ρ, of Hatford-Loam Sand is 2.47 gm/cm^3, therefore the voids ratio, e, varies from 0.690 to 0.578, a spread of 17.7 percent. Since the variation of γ and e is random, no correction factor can be applied and it is assumed that over a number of runs a common, and correct, value of force is obtained.

Some error is also introduced from a slight variation of rail height, but this is compensated by the fact of using a template for the sand level that measures from the rail rather than the floor of the tank.

TABLE 28

INSTRUMENT PRECISION

Instrument	A: Smallest S. D.	B: Reading Range	Error, %, (20A/B)
Strain Bridge	0.01 % R/R	0.10 % R/R	2.0
Chart Recorder	0.2 ma	1.5 - 3.0 ma	2.66 - 0.5
Valve Volmeter	0.001 mv, but	0 - 0.1 mv	0.2
commonly	0.01 mv	0 - 1.0 mv	0.2
X-Y Plotter	0.02 mv	0.2 - 1.0 mv	0.4

The remaining errors are those inherent in reading graduated scales.

Rather than being actual errors, they are limits of precision. The foreplaced table lists the instruments used, the smallest scale division, and the error considering it is possible to be precise to 0.2 of a scale division. The strain bridge was set between even intervals rather than read and was probably more precise than indicated.

The speed varied, due to change of gearing arrangements, by a maximum of 2 percent from that which was desired. Checks were made and it is safe to say that unknown variations of speed were less than 0.5 percent. The results of the speed variation tests show that this is of no consequence.

To eliminate the random errors, four runs, each on both circuits, were made to establish one point. Tabulated, each run counts as two because of the use of the two separate strain circuits. The number of runs was occasionally cut to three (or six) if the results up to then were very uniform. On the whole, this procedure was sufficient to eliminate outlying points; it must be remembered that every plotted point represents an average and that a so-called "true" value can vary from that plotted, within the deviation limits. Error bars indicating the accepted precision of any parameter variation and the standard deviation of force readings for any one determination are included in the graphs.

Analysis

General: At this point, it will be best to examine the results and assess their meanings. This will be done first to the individual force parameters, and then to the mode of failure in the medium. Finally some conclusions will be drawn in an effort to integrate the parameter variations with the failure.

The Force Variable, Depth: Although it was assumed that the force would

increase as the depth cubed, it was hoped that at some depth the influence of the boundaries (the walls of the tank and the free surface) would become negligible. Evidence of this change would be forthcoming if the exponential value of the depth to which the force was related dropped to the square or even to unity. The reasoning was that at some depth the model would not disturb the sand clear to the surface, but would displace an equal sized block of sand no matter the depth. Once this equilibrium was reached, the work would be done in compacting the grains, that is decreasing the voids ratio. Inasmuch as this type of failure varies with the value of the hydrostatic pressure, $P = \gamma d$, it was assumed that at some depth the force would correspond linearly to the depth.

From the graph (Figure 39) and table (12) of depth data, it would seem that some form of change was beginning to occur between 15 and 18 inches of depth. Below that point interference from the sides and bottom forced the related values of force up. It is noted that this depth is 6 times the value of the model diameter. Considering the tolerance limits, however, not too much can be made of this slight flattening of the curve slope. All that can be said is that the force is related to depth raised to the 2.3 power for the depths examined. Further, there is some possibility of another relation for the depth, but the evidence is not strong enough to identify it. To interject, it was because of this flattening and its intimation of the most freedom from boundaries at 18 inches that this depth was chosen for the investigation of the other variables.

The Force and Model Variation: Much of the material in this section is straight-forward and needs no explanation. However, there are several points that could be examined.

In regard to cone angles, another explanation for the lack of variation of force with cone angle is that the cone pushes a small wedge of material, a dead zone so to speak, that is bounded by sliplines of the passive case. This conjecture is illustrated in Figure 64. The angle that the passive slipline makes with the horizontal in Hatford-Loam Sand is 29.7°. Thus, if this explanation is correct, all cone angles greater than 29.7° -- models 1 - 8, 12 -- will respond as if they were flat plates. With this assumption, the force would drop when the cone angle is less than 29.7°, because the value of δ' for metal on sand is less than that of sand on itself. The evidence is somewhat inconclusive, however, the 15° did give higher values than the 45° models. Therefore not much credence will be given this supposition. Unfortunately, this matter could not be investigated more fully because as the cone angles became smaller, with constant base area, the models became longer. Models that are too long would give adverse readings because the long moment arm would accentuate the oscillations at the mount.

To revert to Wells, a value of "point" resistance can be found by extrapolating (Figure 42) the line of force against radius squared to the ordinate instead of assuming the origin as one of the data points. A "point" resistance of approximately 75 pounds results. The tolerance limits, however, are too wide to allow any conclusive statement to be drawn from this extrapolation. The model parameter of projected area needs no further explanation, the force varies linearly with change in area.

It is clear that, within experimental limits, the variation of model surface and length of backing cylinder had no effect on the force.

Speed and the Force: The evidence in regard to speed changes is obvious, up to 15.09 ft/min the force is entirely from static loads and a change in speed should not affect the force. Agreement with Payne's statement is thus

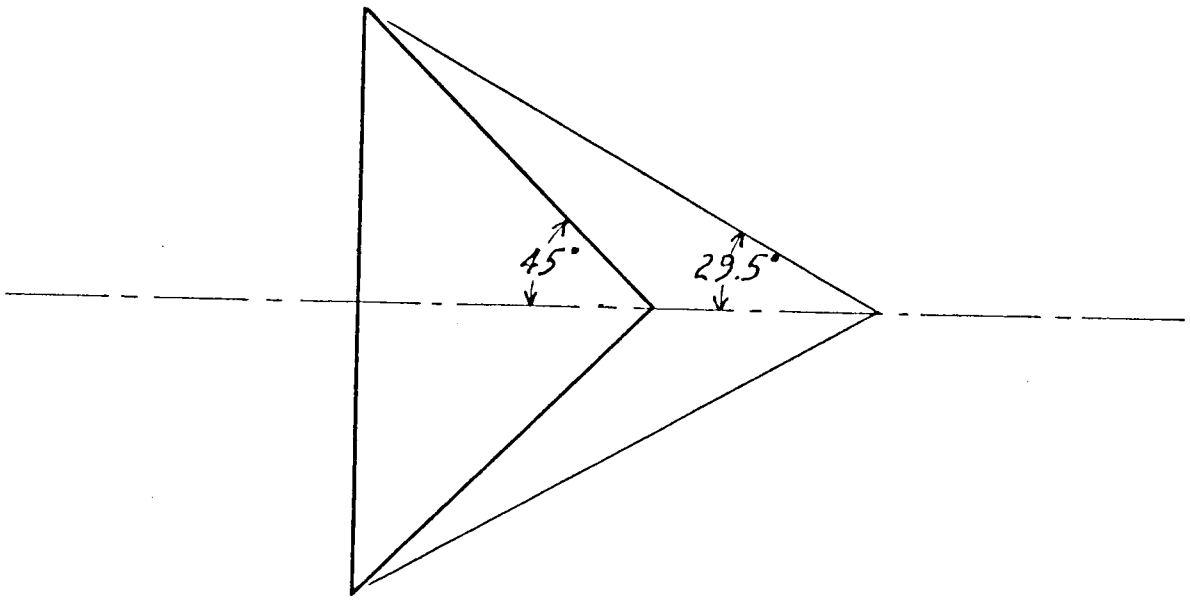

Figure 64: Possible Dead-Zone of Moving Material in Front of the Model

produced. Further, when the speed was varied, within tolerance limits, the force did not vary.

It is unfortunate that the magnitude of forces was not known when the original equipment was ordered because a range of speeds greater than the present 9 to 1 could have been obtained. The incorporation of truly dynamic forces will have to wait for another experiment.

Medium Failure: It would appear that the sand fails in a wedge, the shape of which is determined by sliplines, that is disrupted by the moving model. It is also apparent that the failure surface, as developed by the pressure gauge studies, is affected by the boundaries imposed by the tank. The ratios of model depth to tank width, 1 : 2, and model depth to tank depth, also 1 : 2, were not sufficient to allow uninhibited development of a line of failure. That is the line that would be contained in a plane normal to the direction of travel. It is suspected, as was the case for the line of failure developed in the axial plane, that this line should assume the directions of a passive slipline.

Nevertheless, failure did occur entirely within the medium and not at the walls. This is clearly demonstrated by the pressure data, and by the evidence of the false-walled runs.

Medium Failure and the Force: If the sand fails in a wedge then there are two distinct components to the force on the model. The first is the shear force necessary to cause initial displacement of the wedge; the second is the lifting force necessary to displace the wedge sufficiently to allow the model to pass. THESE ARE RESOLVED ON P. 137A.

Variation of the force, without variation of the parameters, is due to changes in the bulk density of the sand. A seven percent change in weight should cause an equal change in the force. Further, a change in voids ratio will change the angle of internal friction. Bishop and Eldin

show that a 10 percent change in porosity of dry sand will result in a 7-degree change in ϕ. Since a change in the bulk density signifies a comparable change in the voids ratio, hence porosity, the shear strength will increase with the bulk density. Thereupon a change of bulk density will change both the components of force, and it becomes evident why the tolerance limits are the size they are.

The experimental results were repeatable as long as care was taken to insure equivalent conditions in the sand for every run. With the concrete vibrator, repeatability came only as a result of averaging many runs. Completely uniform conditions would have resulted if the entire tank were vibrated as one. The force would then be at its highes for any given condition because the sand would be in its most dense state. Unfortunately, the equipment necessary to vibrate 15 tons of tank and sand was beyond the scope of this experiment.

Because of the data resulting from the model area variation, it must be accepted that the size of the wedge is also dependent upon the model size. A larger model produces a larger, but not deeper, wedge and the force increases as a result. Without conclusive proof this must remain an inference.

In the main, the objects of this investigation have been achieved. Different parameters and their effect on the force have been examined; the rigid boundaries and top free surface and their interference with the force have also been looked at. From the resultant data some relations and conclusions about the force and the model parameters have been drawn; also the limitations of the experiment have been determined.

BIBLIOGRAPHY

Akroyd, T. N. W., 1957, Laboratory Testing in Soil Engineering, London, Soil Mechanics Ltd., 233p.

Binder, Raymond C., 1962, Fluid Mechanics, Englewood Cliffs, N. J., Prentice-Hall, 453p.

Bishop, Alan W. and Eldin, A. K. Gamal, 1953, "The Effect of Stress History on the Relation between ϕ and Porosity in Sand", Proceedings 3rd International Conference on Soil Mechanics and Foundation Engineering, Vol. 1, pp. 100 - 105.

Brown, R. L., July 29, 1961, "Minimum Energy Theorem for Flow of Dry Granules Through Apertures", Nature, Vol. 191, No. 4787, pp. 458 - 461.

Brown, R. L. and Richards, J. C., 1959, "Exploratory Study of the Flow of Granules Through Apertures", Transactions of the Institution of Chemical Engineers, Vol. 37, No. 2, pp. 108 - 119.

Brown, R. L. and Richards, J. C., 1965, "Kinematics of the Flow of Dry Powders and Bulk Solids", Rheologica Acta, Vol. 4, No. 3, pp. 153 - 165.

Cobb, D. E., Cohron, G. T., and Gentry, J. D., "Scale Model Evaluation of Earthmoving Tools", SAE Paper S327 for meeting April 4 - 5, 1962, 8p.

Drucker, D. C., 1953, "Limit Analysis of Two and Three Dimensional Soil Mechanics Problems", Journal of the Mechanics and Physics of Solids, Vol. 1, pp. 217 - 226.

Drucker, D. C. and Prager, W., 1952, "Soil Mechanics and Plastic Analysis or Limit Design", Quarterly of Applied Mathematics, Vol. 10, pp. 157 - 165.

Fowler, R. T. and Glastonbury, J. R., 1959, "The Flow of Granular Solids Through Orifices", Chemical Engineering Science, Vol. 10, pp. 150 - 156.

Franklin, F. C. and Johanson, L. N., 1955, "Flow of Granular Material Through a Circular Orifice", Chemical Engineering Science, Vol. 4, pp. 119 - 129.

Gardner, G. C., 1966, "The Region of Flow When Discharging Granular Materials from Bin-Hopper Systems", Chemical Engineering Science, Vol. 21, pp. 261 - 273.

Gardner, G. C., 28 February 1967, Private Communication.

Hill, R., 1950, The Mathematical Theory of Plasticity, Oxford, Oxford University Press, 353p.

Hodgman, Charles D. (ed.), 1962, Handbook of Chemistry and Physics, Cleveland, Ohio, The Chemical Rubber Publishing Co., 3604p.

BIBLIOGRAPHY CONTINUED

Jenike, A. W., October 1961, Gravity Flow of Bulk Solids, University of Utah, Utah Engineering Experiment Station, Bulletin 108, Salt Lake City, Utah, 309p.

Jenike, A. W., 1964, "Steady Gravity Flow of Frictional-Cohesive Solids in Converging Channels", Journal of Applied Mechanics, Transactions ASME, Vol. 31, Series E, No. 1, pp. 5 - 11.

Johanson, J. R., 1964, "Stress and Velocity Fields in the Gravity Flow of Bulk Solids", Journal of Applied Mechanics, Transactions ASME, Vol. 31, Series E, No. 3, pp. 499 - 506.

Johnson, W. and Mellor, P. B., 1962, Plasticity for Mechanical Engineers, London, D. Van Nostrand Company, Ltd., 412p.

Jyotaki, Tomosada, et. al., Nov. 1962, "Dynamical Behavior of Granular Materials Flowing Down through a Vessel", Japan Society of Mechanical Engineers, Vol. 28, No. 195, pp. 1462 - 1471, (English Summary and Diagrams).

Kirkpatrick, W. M., 1957, "Condition of Failure for Soils", Proceedings 4th International Conference on Soil Mechanics and Foundation Engineering, Vol. 1, p. 172.

Martin, J. B. and Richards, J. C., 1965, "The Determination of the Dynamic Zone Within a Free-Flowing Granular Mass", Journal of Science and Technology, Vol. 11, No. 1 pp. 31 - 34.

Nelson, R. D. and Selig, E. T., "Bulldozing Resistance of Plane Blades in Cohesionless Soil", SAE Paper 897A for meeting Sept. 14 - 17, 1964, 13p.

Pariseau, W. G., 1966, The Gravity Induced Movement of Materials in Ore Passes Analyzed as a Problem in Coulomb Plasticity, Unpublished Doctoral Thesis, University of Minnesota.

Payne, P. C. J., 1956, "The Relationship between the Mechanical Properties of Soil and the Performance of Simple Cultivation Implements", Journal of Agricultural Engineering Research, Vol. 1, No. 1, pp. 23 - 50.

Rose, H. E. and Tanaka, Tatsuo, Oct. 23, 1959, "Rate of Discharge of Granular Materials for Bins and Hoppers", The Engineer, Vol. 208, pp. 465 - 469.

Savage, S. B., 1965, "The Mass Flow of Granular Materials Derived from Coupled Velocity-Stress Fields", British Journal of Applied Physics, Vol. 16, pp. 1885 - 1888.

Scott, Ronald F., 1963, Principles of Soil Mechanics, Reading, Massachusetts, Addison-Wesley Publishing Company, Inc., 550p.